VOLUME 39 JULY 1961 NUMBER 7

Canadian Journal of Physics

Editor: H. E. DUCKWORTH

Associate Editors:

L. G. ELLIOTT, *Atomic Energy of Canada, Ltd., Chalk River*
J. S. FOSTER, *McGill University*
G. HERZBERG, *National Research Council of Canada*
L. LEPRINCE-RINGUET, *Ecole Polytechnique, Paris*
B. W. SARGENT, *Queen's University*
G. M. VOLKOFF, *University of British Columbia*
W. H. WATSON, *University of Toronto*
G. A. WOONTON, *McGill University*

Published by THE NATIONAL RESEARCH COUNCIL

OTTAWA CANADA

CANADIAN JOURNAL OF PHYSICS

Under the authority of the Chairman of the Committee of the Privy Council on Scientific and Industrial Research, the National Research Council issues THE CANADIAN JOURNAL OF PHYSICS and five other journals devoted to the publication, in English or French, of the results of original scientific research. Matters of general policy concerning these journals are the responsibility of a joint Editorial Board consisting of: members representing the National Research Council of Canada; the Editors of the Journals; and members representing the Royal Society of Canada and four other scientific societies.

EDITORIAL BOARD

Representatives of the National Research Council

I. McT. Cowan (Chairman), *University of British Columbia*
Léo Marion, *National Research Council*
H. G. Thode, *McMaster University*
D. L. Thomson, *McGill University*

Editors of the Journals

D. L. Bailey, *University of Toronto*
T. W. M. Cameron, *Macdonald College*
F. E. Chase, *Ontario Agricultural College*
H. E. Duckworth, *McMaster University*
Léo Marion, *National Research Council*
J. F. Morgan, *Department of National Health and Welfare, Ottawa*
J. A. F. Stevenson, *University of Western Ontario*

Representatives of the Societies

D. L. Bailey, *University of Toronto*
Royal Society of Canada
T. W. M. Cameron, *Macdonald College*
Royal Society of Canada
H. E. Duckworth, *McMaster University*
Royal Society of Canada
Canadian Association of Physicists
P. R. Gendron, *University of Ottawa*
Chemical Institute of Canada
D. J. Le Roy, *University of Toronto*
Royal Society of Canada
J. F. Morgan, *Department of National Health and Welfare, Ottawa*
Canadian Biochemical Society
R. G. E. Murray, *University of Western Ontario*
Canadian Society of Microbiologists
J. A. F. Stevenson, *University of Western Ontario*
Canadian Physiological Society

Ex officio

Léo Marion (Editor-in-Chief), *National Research Council*
J. B. Marshall (Administration and Awards), *National Research Council*

Manuscripts for publication should be submitted to Dr. H. E. Duckworth, Editor, Canadian Journal of Physics, Hamilton College, McMaster University, Hamilton, Ontario.
For instructions on preparation of copy, see **NOTES TO CONTRIBUTORS** (back cover).

Proof, correspondence concerning proof, and orders for reprints should be sent to the Manager, Editorial Office (Research Journals), Division of Administration and Awards, National Research Council, Ottawa 2, Canada.

Subscriptions, renewals, requests for single or back numbers, and all remittances should be sent to Division of Administration and Awards, National Research Council, Ottawa 2, Canada. Remittances should be made payable to the Receiver General of Canada, credit National Research Council.

The journals published, frequency of publication, and subscription prices are:

Canadian Journal of Biochemistry and Physiology	Monthly	$9.00 a year
Canadian Journal of Botany	Bimonthly	$6.00 a year
Canadian Journal of Chemistry	Monthly	$12.00 a year
Canadian Journal of Microbiology	Bimonthly	$6.00 a year
Canadian Journal of Physics	Monthly	$9.00 a year
Canadian Journal of Zoology	Bimonthly	$5.00 a year

The price of regular single numbers of all journals is $2.00.

Canadian Journal of Physics

Issued by THE NATIONAL RESEARCH COUNCIL OF CANADA

VOLUME 39 JULY 1961 NUMBER 7

THE SPECTRUM OF NEUTRONS FROM THE IRRADIATION OF URANIUM BY 14-MEV NEUTRONS[1]

R. L. CLARKE

ABSTRACT

The spectrum and absolute yield of neutrons resulting from 14-Mev neutrons incident on natural uranium was observed at 90°±16 to the incident neutron beam by a time-of-flight method. Further observations of the spectrum from 9 to 13.5 Mev were made for scattering angles at 30° and 60°. In addition to the expected neutrons resulting from evaporation and fission, strong evidence is seen for direct interaction inelastic scattering. The (n,n') cross section is estimated to be 150±70 millibarns.

INTRODUCTION

The spectrum of neutrons resulting from 14-Mev neutrons incident on natural uranium has been given by Zamyatnin *et al.* (1957) and by Vasilev *et al.* (1957). The experiment of Zamyatnin was done with photographic plates and covered the region from 0.5 to 6.0 Mev. The work of Vasilev was done with a time-of-flight system and covered the region from 0.05 to about 1.1 Mev. These workers did not give any normalization of their yields either on an absolute scale or relative to each other.*

The object of the present experiment was to extend the spectrum measurements to a higher energy and to give the yields on an absolute scale. The shape and angular distribution of the high-energy part of the spectrum strongly suggest the presence of direct interactions. The shape and intensity of the lower-energy part of the spectrum are expected to depend sensitively on the competition between neutron evaporation and fission following compound nucleus formation, which has been discussed by, for example, Jackson (1956) and Leachman (1958). Hanna and Clarke (1961) have made numerical estimates of the contributions from fission and evaporation and have compared these with the experimental results to give some information about the nuclear processes involved.

[1]Manuscript received January 16, 1961.
Contribution from Atomic Energy of Canada Limited, Chalk River, Ontario.
Issued as A.E.C.L. No. 1240.

*NOTE ADDED IN PROOF: Recently Vasilev *et al.* (Vasilev *et al.* Soviet Physics J.E.T.P. **11**, 483 (1960)) have measured the spectrum of neutrons emitted in coincidence with fission. Their data suggest a higher cross section in the region of 5 Mev than was observed in the present work. The reason for the discrepancy is not clear.

APPARATUS

The spectrum of neutrons resulting from 14-Mev neutrons incident on natural uranium was measured by a time-of-flight technique, using neutrons from the TD reaction. These neutrons were produced by a 120-kev deuteron beam which struck a tritium–zirconium target. Observations were carried out at right angles to the deuteron beam; hence the energy of the incident neutrons was 14.1 Mev.

A schematic view of the apparatus, as seen looking toward the accelerator, is shown in Fig. 1. The recoil alpha particles from the reaction are counted

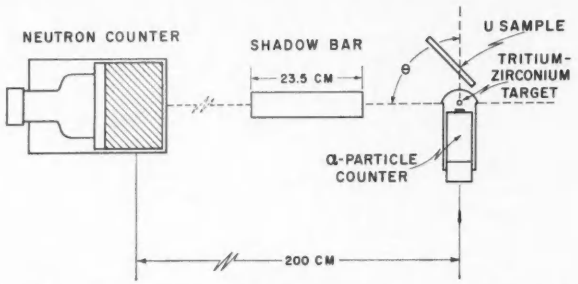

FIG. 1. The time-of-flight apparatus. The deuteron beam is normal to the plane of the figure and strikes the T–Zr target just above the α-particle counter. The shaded areas represent plastic scintillators.

by means of a thin plastic scintillator in direct contact with an R.C.A. 6342 photomultiplier. The scattered neutrons were detected in a plastic scintillator, 7 in. diameter by 5 in. thick, coupled to a 5 in. diameter Dumont photomultiplier. The measured times, from which the neutron flight times were deduced, were taken from the occurrence of a pulse in the alpha counter to the occurrence of a pulse in the neutron counter. This delayed coincidence requirement between the neutron and alpha counters in effect defined a beam of neutrons whose width was determined by the collimator in front at the alpha counter. The full width of this beam at half maximum was 32°. The center of the phosphor was 200 centimeters from the target on a line approximately at right angles to the deuteron beam axis.

The sample consisted of a sheet of natural uranium 10 cm × 10 cm × 0.7 cm supported on a light brass frame at an angle of 45° to the neutron beam, 12 centimeters from the target. The major portion of the neutron beam defined by the alpha-particle collimator thus passed through the sample. The thickness of the sample was so chosen that about 28% of the neutrons passing through it suffer an interaction. Of these interactions, half are due to elastic scattering which, because it is strongly peaked in the forward direction, has little effect on the experiment.

A copper shadow bar was placed between the target and the neutron counter to reduce the background due to direct neutrons from the target. Additional shielding was placed between the neutron counter and those portions of the

accelerator, such as diaphragms in the beam path, which gave rise to significant background. With this system only a few counts per minute were observed, distributed over all flight times. Thus it was necessary to count for long periods to get adequate statistics.

This system was used for the high-energy portion of the work.

The time-to-pulse-height converter resembled, with only minor modifications, that of Neilson and James (1958). The distribution of flight times was displayed on a 30-channel pulse-height analyzer on which each channel corresponded to about 3.5×10^{-9} seconds. The time-to-pulse-height converter was calibrated in three ways: by the insertion of known delays in artificial pulses put in at the preamplifiers, by changing the length of the flight path with the neutron beam aimed directly at the neutron counter, and by observing the flight time of neutrons scattered by hydrogen through known angles. The satisfactory agreement between these methods showed that the equipment was operating as required. The resolution of the system was found to be $\sim10\times10^{-9}$ seconds. This was limited principally by the 5 in. photomultiplier.

The energy sensitivity of the neutron detector was measured in two ways. In the first a cylindrical piece of polyethylene 2.5 cm in diameter and 5 cm long was supported 25 centimeters from the target with its axis parallel to the deuteron beam axis. The neutrons scattered from both the hydrogen and carbon in the sample can be seen as peaks in the time spectrum in Fig. 2.

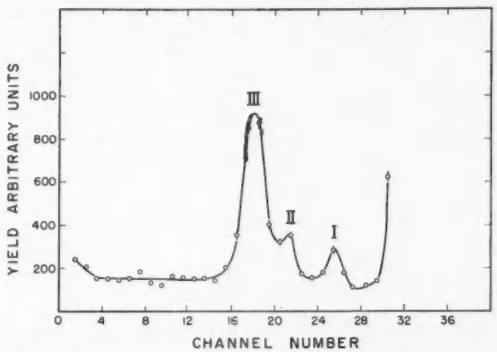

FIG. 2. The spectrum of neutrons from 14-Mev neutrons scattered by polyethylene. The scattering angle is 40°. The peaks due to elastic scattering from carbon, inelastic ($Q = -4.43$) scattering from carbon, and scattering from hydrogen are labelled I, II, and III, respectively. The areas under these peaks, less the background, were used to calibrate the detector. Part of the γ-ray peak can be seen at the right of the figure.

The observed yields, that is the areas under the peaks, were used to calibrate the energy sensitivity of the detector in terms of the known scattering cross sections for hydrogen (Hughes and Schwartz 1958) and carbon (Anderson *et al.* 1958). The results from hydrogen as the angle θ (Fig. 1) was varied from 25° to 55° gave a calibration from 3.9 to 9.7 Mev. The elastic scattering from carbon gave a point at 13.5 Mev.

In the second method the polyethylene scatterer was replaced by a cylinder of plastic phosphor 2.5 cm in diameter and 5 cm long, connected to an R.C.A. 6342 photomultiplier. This scattering counter was used instead of the alpha-particle counter to give the zero time signal in the time-of-flight system. With a bias on the scattering counter set low enough, all events due to neutrons scattered from the hydrogen in it to the neutron counter could be identified from their flight times. Because of the relatively low counting rate in the scattering counter and because the neutrons scattered from carbon did not give rise to any background, this method of calibration was considered more accurate than the first. It gave a calibration from 2.2 to 12.0 Mev.

In both methods the scattered neutron energy was calculated from the geometry rather than from the position of the neutron peak in the time spectrum. The results from the two methods agree within the limits of experimental error. The energy sensitivity curve finally used is shown in Fig. 3(*a*).

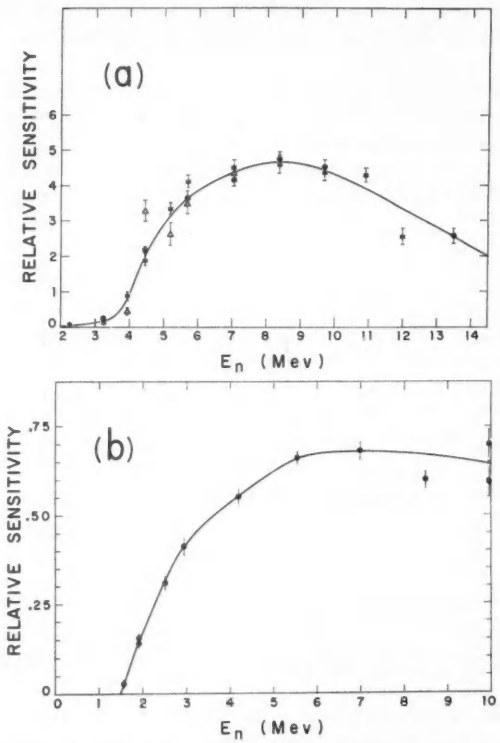

FIG. 3. The sensitivities of the neutron counters to neutrons of various energies, (*a*) for a plastic scintillator 17.8 cm diameter×12.7 cm thick, (*b*) for a stilbene crystal 2 cm×2 cm×4 cm. In Fig. 2(*a*) the crosses refer to data taken by scattering from a scintillator (see text), the triangles by scattering from polyethylene, the circles to an average of an earlier calibration using both the above techniques. The units of sensitivity used are the same for both counters.

This counter could not be used for the lowest-energy part of the spectrum because of the rapid increase of background as the bias was reduced below 3 Mev. For this part of the spectrum a neutron counter consisting of a stilbene crystal 2 cm×2 cm×4 cm in contact with an R.C.A. 6342 photomultiplier was used with a flight path of 1 meter. This counter was calibrated in the same manner as the large counter and was found to have a resolution of 6×10^{-9} seconds. The sensitivity curve is shown in Fig. 3(*b*).

Both these calibrations gave relative efficiencies as a function of energy; the absolute value of the uranium neutron yield was obtained in terms of the known carbon cross section by comparison with the yield from a carbon sample of known mass and the same geometry as the uranium.

The angular distribution of high-energy neutrons is important in determining the processes which govern neutron emission, as discussed below. For those neutrons of energy greater than 9 Mev the angular distribution was measured using a later version of the instrument. A 10 cm diameter by 10 cm long cylinder of plastic phosphor was mounted on an R.C.A. 7046 photomultiplier and surrounded by heavy shielding. This system gave a resolution of 2×10^{-9} seconds. In this case the flight path was 2.76 meters.

It was found that there was a substantial dependence of the background in the neutron counter on the beam intensity. Hence, the random coincidence background was approximately proportional to the square of the beam current. In spite of this, an accurate subtraction of the accidental coincidence rate could be made by assuming that this background was proportional to the product of the total alpha-particle and neutron counts. This was possible because during the rather long periods of observation required, the beam current was automatically controlled so as to hold the alpha-particle counting rate, and hence the neutron production constant. The background which was used for each channel of the time spectrum was found from a run made with the sample removed, but with other conditions unaltered. The background spectrum thus found was weighted by the product of the neutron and alpha-particle counting rates and subtracted from the spectrum observed with the sample in place.

RESULTS

A typical time-of-flight spectrum after background subtraction but before correction for counter sensitivity is shown in Fig. 4. This is a composite spectrum, the result of several runs taken with the large phosphor. The peaks due to gamma rays, elastically scattered neutrons, and inelastically scattered neutrons can all be seen. The uncertainty in the shape of the elastic peak introduced an error of a factor of about 2 at 12 Mev. This error becomes negligible at 10 Mev. In subtracting the elastic peak from the observed spectrum, the peak was assumed to be symmetrical about its maximum. This procedure may overestimate slightly the yield of inelastic neutrons.

No correction to the spectrum shape was made for multiple scattering in the sample. Over the range of neutron energies of interest, from 3 to 14 Mev, both the total and non-elastic cross sections show only a small variation

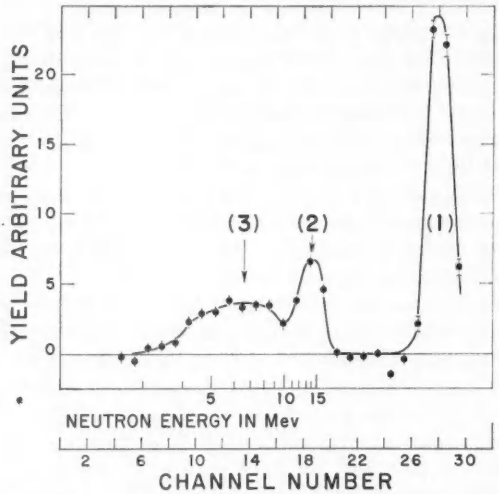

FIG. 4. Time-of-flight spectrum observed at 90° for 14-Mev neutrons scattered from natural uranium using the apparatus of Fig. 1. Peak (1) corresponds to γ-rays, peak (2) to elastically scattered neutrons, and the continuum (3) to the inelastically scattered neutrons.

(Hughes and Schwartz 1958; and Almqvist and Clarke 1955). Since the effect of non-elastic scattering is in general to degrade the neutron energy to less than 2 Mev, such a scattering event will remove a neutron entirely from observation by the present experiment. Since elastic scattering is predominantly forward, its effect is to spread out slightly the angular resolution of the experiment. This effect will be most pronounced at high energies, where, as is shown in the present experiment, the angular distribution is most anisotropic. At energies below 8 Mev, where the distribution is isotropic, there should be no distortion of the spectrum due to elastic scattering. A rough estimate shows that at the highest observed energy, 12 Mev, the distortion is less than 2% so that to the accuracy of the present experiment, it may be neglected.

Because the uranium sample was about four times thicker than the carbon sample in terms of neutron mean free path, a correction was made for self-absorption in making the comparison between carbon and uranium absolute yields. The result was to increase the uranium cross section by $10\pm3\%$.

The energy spectrum obtained from the time-of-flight spectrum after the corrections discussed above have been applied, is shown in Fig. 5. The figure is a combination of the data from the three detectors. The data of Zamyatnin (1957) and Vasilev *et al.* (1957) are shown for comparison. Their data have been normalized to the present work only by eye. Although none of the three curves shown overlap each other perfectly, there is general agreement as to the shape of the spectrum. The most conspicuous features are the low energy at which the maximum occurs and the flattening of the curve at energies above 6 Mev.

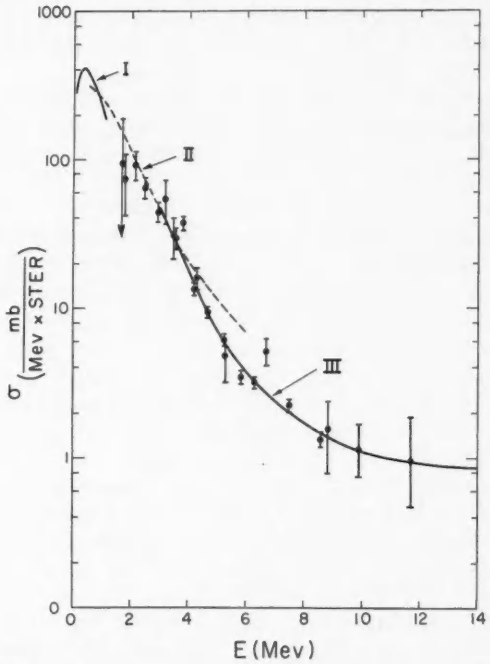

FIG. 5. The spectrum of neutrons observed at 90° from the scattering of 14-Mev neutrons from natural uranium. Curve I is the data of Vasilev *et al.* (1957), curve II that of Zamyatnin *et al.* (1957). The experimental points and curve III are the data of the present work. The curve is drawn only to aid the eye. The errors shown are due to counting statistics only, as discussed in the text.

Sources of systematic error may be summarized as follows:

(1) In the calibration of the time-to-pulse-height converter, there is an uncertainty of about 5% in the number of nanoseconds per channel and an uncertainty of about 0.5 channels in the position of the channel corresponding to the origin of the time scale. These uncertainties produce errors both in the energy scale and in the cross-section values. The latter arises in the calculation of the yield per Mev from the observed yield and the calculated channel width in Mev. The error thus introduced in the cross section is a maximum near 5 Mev, where it reaches a value of about 20%.

(2) For energies near 14 Mev there is an error due to the uncertainty in subtracting the elastic peak. This introduces an uncertainty in the last few points, rising from zero for the point near 9 Mev to a factor of 2 for the point at 12 Mev.

(3) The error in the normalization of the uranium yield relative to the carbon cross section of Anderson *et al.* (1958) arises from the self-absorption corrections discussed above, from statistics, from uncertainties in placing the carbon in the same position as the uranium, and from the limited stability

of the equipment over the considerable periods of time involved. This error may be taken to be 5%. The error in the work of Anderson *et al.*, which appears to be less than 5%, is negligible.

(4) The spectrum and the corrections to it become increasingly unreliable at low energies due to uncertainties in the sensitivity curve. Allowance for this has been made in assigning errors at the lower end of the spectrum.

Because the yield of neutrons for energies greater than 6 Mev is difficult to account for on the basis of either evaporation or fission (Hanna and Clarke 1961), it was felt that it might be due to direct interaction. Spectra were measured at scattering angles of 30°, 60°, and 90° using the 10 cm×10 cm detector. The results after subtraction of the elastic peak are shown in Fig. 6,

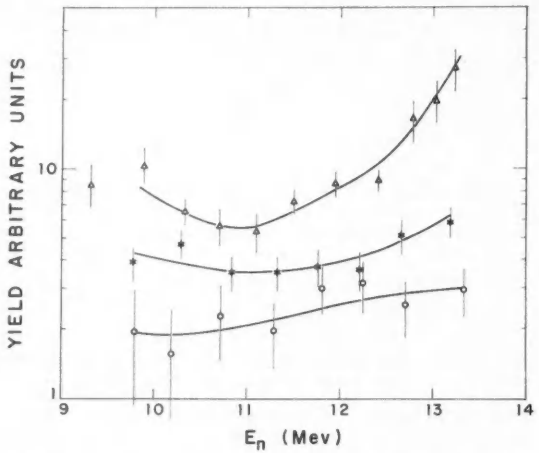

FIG. 6. The yield of neutrons resulting from 14-Mev neutrons incident on natural uranium. Symbols refer to angles of observation; circles, 90°; stars, 60°; triangles, 30°. In each case the contribution of elastically scattered neutrons has been subtracted. The curves are drawn only to aid the eye.

where it can be seen that the yield is higher at small angles, the effect being most pronounced as the energy approaches 14 Mev. These data are qualitatively similar to the data of Rosen and Stewart (1955) on bismuth and suggest that the forward peak in the neutron yield is a result of direct interaction processes.

Using these data, an estimate of the (n,n') cross section can be made. The thresholds for the (γ,n) and (γ,α) reactions on U^{238} are 6.0 and 5.8 Mev, respectively (Cameron 1956). Thus, it is reasonable to assume that those neutrons which, on inelastic scattering, leave the target nucleus, U^{238}, excited to less than 6 Mev are the outgoing neutrons from the (n,n') reaction. In estimating the number of these neutrons from the angular distribution data, the total yield from 8 Mev to 14 Mev is required for all angles. The present data were extrapolated by assuming (1) that differential cross section is constant from 90° to 180° angle of observation, and (2) that the cross section from 8 Mev to

9 Mev is the same as that at 9 Mev. The former assumption probably overestimates the cross section; the latter probably constitutes an underestimate. In integrating over energy to get the total $\sigma(n,n')$ the region from 13.5 Mev to 14 Mev was neglected. There is really no way in this experiment of distinguishing scattered neutrons which have lost only 0.5 Mev from elastic neutrons, nor is there any way of estimating their total yield. Subject to these uncertainties, a value of $\sigma(n,n')$ or 150 ± 70 millibarns is obtained.

DISCUSSION

The shape of the observed spectrum, with its maximum at 0.5 Mev, and the relatively large yield at energies up to 8 Mev strongly suggest that both evaporation and fission neutrons contribute significantly to the spectrum. An analysis of the shape in terms of multiple neutron evaporation from U^{238} followed in some cases by fission has been given by Hanna and Clarke (1961). From the ratio of the total area under the curve, 7.8 barns and the non-elastic cross section, 2.90 barns, a value of 2.7 is obtained for η, which is in satisfactory agreement with experiment (see Hanna and Clarke). Because of the difficulty in normalizing the data of Vasilev *et al.* (1957) and Zamyatnin *et al.* (1957) to the data of this experiment, the value given here should not be considered an accurate determination. However, it does indicate that the cross sections found are consistent with other experimental determinations of η.

In Fig. 6 it can be seen that between 11 and 14 Mev an increase in yield is seen, especially at small angles. This is not seen in Fig. 5 because of the large uncertainties in the data near 14 Mev. This increase in differential cross section resembles the increase in cross section seen at small angles for individual levels in light nuclei (Anderson *et al.* 1958; Clarke and Cross 1959, 1960). For those neutrons from U having energies greater than 12.5 Mev, corresponding to levels in U of low excitation, the ratio of the yield at 30° to that at 90° is of the order of 10:1, which is greater than the ratio of yields seen for the first excited states of S^{32} ($W = 2.24$ Mev) and Mg^{24}($Q = 1.37$ Mev). The angular distributions seen for neutrons in the region 9 Mev to 12 Mev, corresponding to $Q = -2$ to -5 Mev, appear to be comparable to those seen in S and Mg for individual states having similar Q values. Thus it is reasonable to suppose that the angular distribution seen in U scattering arises from causes similar to the direct interactions seen in light nuclei. This hypothesis is further supported by the large intrinsic quadrupole moment of U^{238}, which would be expected to give rise to strong surface direct interaction according to the models of Inopin (1956), Ui (1959), and Blair (1959).

As stated above, the total cross section for neutrons of energy between 8 and 13.5 Mev is about 150 millibarns, which is 15% of the total non-elastic cross section. The portion of the cross section corresponding to excitations less than 0.5 Mev was not measured, and the fraction of this cross section which may be due to direct interaction is not known, consequently the true direct interaction cross section is not known. However, the ratio of this high-energy yield is similar to the ratios of direct to total non-elastic seen for Mg, C, and Be, which lie between 10% and 30% (Anderson *et al.* 1958; and Ball *et al.* 1958).

ACKNOWLEDGMENTS

The writer is indebted to Mr. G. C. Hanna and Dr. W. G. Cross for many helpful discussions.

REFERENCES

ALMQVIST, E. and CLARKE, R. L. 1955. Unpublished.
ANDERSON, J. D., GARDNER, C. C., NAKADA, M. P., and WONG, C. 1958. Phys. Rev. **110**, 160.
ANDERSON, J. D., GARDNER, C. C., MCCLURE, J. W., NAKADA, M. P., and WONG, C. 1958. Phys. Rev. **111**, 572.
BALL, W. P., MACGREGOR, M., and BOOTH, R. 1958. Phys. Rev. **110**, 1392.
BLAIR, J. S. 1959. Phys. Rev. **115**, 928.
CAMERON, A. G. W. 1956. Paper B6 of A.E.C.L. 329.
CLARKE, R. L. and CROSS, W. G. 1960. Bull. Am. Phys. Soc. **5**, No. 4, 245.
CROSS, W. G. and CLARKE, R. L. 1959. Bull. Am. Phys. Soc. **4**, No. 4, 258.
HANNA, G. C. and CLARKE, R. L. 1961. Can. J. Phys. **39**. This issue.
HUGHES, D. J. and SCHWARTZ, R. B. 1958. B.N.L. 325, 2nd ed.
INOPIN, E. V. 1956. J. Exptl. Theoret. Phys. (U.S.S.R.) **31**, 901.
JACKSON, J. D. 1956. Paper B2 of A.E.C.L. 329.
LEACHMAN, R. B. 1958. U.N. Geneva Conference, **15**, 229.
NEILSON, G. C. and JAMES, D. B. 1958. R.S.I. **26**, 1018.
ROSEN, L. and STEWART, L. 1955. Phys. Rev. **99**, 1052.
UI, H. 1959. Progr. Theoret. Phys. **18**, 163.
VASILEV, Yu. A., ZAMYATNIN, Yu. S., TOROPOV, P. V., and FOMUSHKIN, E. F. 1957. Atomnaya Energ. **3**, 540.
ZAMYATNIN, Yu. S., GUTNIKOVA, E. K., IVANOVA, N. I., and SAFINA, I. N. 1957. Atomnaya Energ. **3**, 542.

NEUTRON EVAPORATION IN THE 14-MEV NEUTRON FISSION OF URANIUM[1]

G. C. Hanna and R. L. Clarke

ABSTRACT

The numbers of prefission and postfission neutrons expected from the 14-Mev neutron fission of uranium have been calculated from the experimental data on partial cross sections and neutron multiplicities. It has been assumed that the competition between neutron emission and fission does not change with increasing energy beyond threshold. The neutron energy spectrum measured recently by Clarke gives a smaller intensity in the energy range 4–6 Mev than is expected from the calculated number of postfission neutrons. The measured intensity suggests that only 2.1 ± 0.5 neutrons are evaporated from the moving fission fragments.

INTRODUCTION

As described in the preceding paper, Clarke (1961) has measured the energy spectrum of neutrons resulting from the interaction of 14-Mev neutrons and natural uranium. He has also measured the angular distribution of the highest-energy neutrons and concluded that these are probably the result of direct interaction processes. Below about 6 Mev the direct interaction neutrons can be neglected in comparison with those emitted following compound-nucleus formation. These arise from two sources. The lowest-energy region is dominated by neutrons evaporated from the compound nucleus either before fission takes place or when there is no fission. At somewhat higher energies, especially between 4 and 6 Mev, most of the observed intensity is due to neutrons evaporated from the moving fission fragments.

Enough is known of the course of the reactions to predict with reasonable accuracy the total number of prefission and postfission neutrons, and, for the latter neutrons, the energy spectrum as well. The present paper calculates these expected effects and compares them with what is observed experimentally.

EXPECTED INTENSITIES

The capture of a 14.1-Mev neutron in U^{238} forms U^{239} with an excitation energy of 18.86 Mev (Foreman and Seaborg 1958), which may undergo fission or evaporate a neutron (its de-excitation by gamma radiation is very improbable). In the latter case a U^{238} nucleus is formed with an excitation energy that is less than that of the parent U^{239} by the sum of the neutron kinetic energy, which is on the average 1 Mev,* and the neutron binding energy; the average excitation of the U^{238} is therefore 13.1 Mev. This U^{238}

[1]Manuscript received January 17, 1961.
Contribution from the Nuclear Physics Branch, Atomic Energy of Canada Limited, Chalk River, Ontario.
Issued as A.E.C.L. No. 1241.

*That is, twice the temperature of the evaporation spectrum, which is close to 0.5 Mev (see below).

nucleus can in turn undergo fission or evaporate another neutron, and so on according to the scheme of Fig. 1. The competition between the different

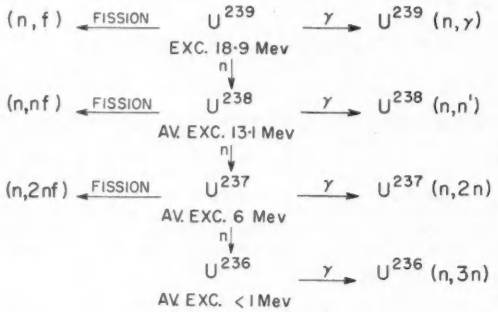

FIG. 1. Nuclear reactions produced by 14-Mev neutrons on U^{238}.

processes is expressed in terms of the various partial cross sections, on which there is fairly complete experimental information (see Appendix). The finally adopted values are given in Table I, which also lists N_f, the number of neutrons

TABLE I

Partial cross sections and neutron multiplicities in the interaction of 14.1-Mev neutrons with U^{238}

x	Nucleus	Excitation (Mev)	$\sigma(n,xnf)$ (barns)	N_f	$\sigma(n,xnf)$ $\times N_f$	$\sigma(n,xnf)$ $\times(N_f+x)$	$\sigma(n,xn)$ (barns)	$\sigma(n,xn)$ $\times x$
0	U-239	18.86	0.55	4.22_4	2.32_3	2.32_3	0	0
1	U-238	13.1	0.45	3.40_7	1.53_3	1.98_3	0.15	0.15
2	U-237	6.0	0.17	2.40	0.40_8	0.74_8	0.84	1.68
3	U-236	~ 0	0	0	0	0	0.74	2.22
Totals			1.17		4.26_4	5.05_4	1.73	4.05

NOTE: μ = number of postfission neutrons per fission = $4.264/1.17 = 3.64_4$.
ν = number of pre- and post-fission neutrons per fission = $5.054/1.17 = 4.32_0$.
η = number of secondary neutrons per interaction = $(5.054 + 4.05)/2.90 = 3.14$.

emitted following the different types of fission; the basis of these estimates is given in the Appendix.

Table I shows that the average number of postfission neutrons per fission, μ, is 3.64 compared with the average total number per fission (ν) of 4.32, which includes the prefission evaporation neutrons. The average number of neutrons produced per interaction, η, is calculated to be 3.14, which may be compared with recently reported direct measurements of 2.8 ± 0.25 by Lebedev *et al.* (1958) and 2.99 ± 0.15 by Flerov and Talyzin (1958) and with an unpublished value of 3.29 ± 0.15 by Allen (1960). The value obtained from the curve of Fig. 2 is 2.7, but this result is sensitive to the fitting of the low-energy Russian data to the rest of the curve, and Clarke's (1961) experiment cannot be regarded as a satisfactory measurement of η.

It is therefore not legitimate to discuss his experimental data in terms of μ/η, although this would have the advantage of eliminating uncertainties in absolute intensity measurements. Rather, the calculated value of μ is to be compared with the value expected from the observed intensity in the 4- to 6-Mev region. It should therefore be noted that μ is calculated from the published values of the directly measured quantity ν by the relation

$$\mu = \nu - \frac{\sigma_{n,nf} + 2\sigma_{n,2nf}}{\sigma_f},$$

which is independent of the non-fission cross sections. Estimates of the uncertainties in the individual terms are given in the Appendix; they lead to a value of about ± 0.18 for the uncertainty in μ. No precise meaning can be attached to this estimate of the uncertainty, but, at $\pm 5\%$, it is clearly smaller than that of the experimental intensity measurements.

THE EXPECTED FISSION-NEUTRON SPECTRUM

The total area of the postfission-neutron spectrum, $\mu\sigma_f$, is expected to be 4.26 neutron barns (Table I). With the assumption that all these neutrons are evaporated from the moving fission fragments, the spectral shape is expected to be rather similar to that of the slow neutron fission of U^{235}.* Wahl (1954) has shown that the fragment velocities in 14-Mev fission are essentially the same as in thermal fission. However, the 14-Mev fission-neutron spectrum is expected to be slightly more energetic because the fragment temperatures are higher. The spectrum measured in a particular direction will be further modified as a result of the angular correlation of the fission neutrons and fission fragments since the fragments are not isotropic with respect to the 14-Mev neutron direction.

The correction for fragment temperature was calculated following Terrell (1959), who showed that the fission-neutron energy spectrum can be adequately represented by a Maxwellian distribution $(2/\sqrt{\pi})\,(E/\theta)^{\frac{1}{2}}\exp(-E/\theta)\,(dE/\theta)$, where θ is a fictitious temperature defined by $3\theta/2 = \bar{E}$, the mean neutron energy in the laboratory system. From a study of the available data Terrell has concluded that $\bar{E} = 0.78+0.621\,(N_t+1)^{\frac{1}{2}}$ Mev, where N_t is the number of postfission neutrons (and is equal to ν in systems where only (n,f) reactions are possible). Terrell's scale of ν values is based on 2.46 for U^{235} thermal fission; for the present analysis, with ν equal to 2.43 (Hughes *et al.* 1960), his relation becomes $\bar{E} = 0.78+0.624\,(N_t+1)^{\frac{1}{2}}$. The postfission-neutron spectrum expected from the 14-Mev neutron fission of U^{238} is therefore the sum of three components with (see Table I) intensities of 2.323, 1.533, and 0.408 neutron barns and fictitious temperatures corresponding to, respectively, N_t values of 4.224, 3.407, and 2.40, i.e. θ values of 1.470, 1.393, and 1.287 Mev.

Table II gives the ratio, as a function of energy, of the intensity of this complex spectrum to that of the simple spectrum with θ equal to 1.287 Mev. These will be referred to as the "hard" and "soft" spectrum respectively.

*This is true provided that the angular distribution in the fragment system, generally assumed isotropic, is the same in both cases.

TABLE II

The ratio of the intensity of the expected postfission-neutron spectrum in 14-Mev fission to that of the thermal fission spectrum

E(Mev)	0.5	1	1.5	2	3	4	5	6	8	10
Ratio hard/soft	0.901	0.925	0.960	0.996	1.073	1.157	1.247	1.347	1.59	1.84

It is difficult to estimate the uncertainty in this hardening correction, which is appreciable at high neutron energy. Fortunately its reliability is not of crucial importance for the purposes of the present discussion.

In the 14-Mev neutron fission of U^{238} the fragments are emitted preferentially in the direction of the incoming beam; according to Henkel and Brolley (1956) the ratio of intensities at 0° and 90° is 1.40±0.14. In the present experiment the secondary neutrons are observed at 90° to the 14-Mev neutron beam axis and thus preferentially at 90° to the direction of motion of the fission fragments. The neutrons evaporated from the moving fragments are peaked in the fragment direction, and the present experiment therefore observes fewer fission neutrons than would be expected if the fission process were isotropic. The magnitude of this effect was calculated by using a simplified model of the fission process due to Milton (1958), which assumes a single typical mass splitting and, from each fragment, an equal neutron evaporation characterized by two nuclear temperatures, so that in the fragment system the energy spectrum from each fragment is

$$N(\eta) = \frac{\alpha\eta}{T_1^2} \exp \frac{(-\eta)}{T_1} + \frac{(1-\alpha)\eta}{T_2^2} \exp \frac{(-\eta)}{T_2} .$$

α, T_1, and T_2 are adjusted to fit the energy spectrum observed in the laboratory system. Although this model is evidently oversimplified it is acceptable for the present purpose since the calculated effect is quite small (see Table III).

TABLE III

The effect of angular correlation on the fission neutron flux at right angles to the 14-Mev neutron beam

Laboratory energy (Mev)		0	0.5	1	2	4	6	8	10
$\frac{\text{(Average intensity}-\text{intensity at 90°)}}{\text{Average intensity}}$	×100	0	2.3	3.5	4.2	4.8	6.2	7.0	7.3

NOTE: These numbers were calculated for a 14-Mev neutron beam of zero angular divergence; for the spread (~30°) of the present work they should be multiplied by about 0.9.

COMPARISON WITH THE EXPERIMENTAL DATA

The experimental data of the preceding paper (Clarke 1961) are reproduced in Fig. 2. The smoothed data, curve III of Fig. 2, are reproduced as curve A of Fig. 3, which also shows two calculated fission spectra, B and C, both corrected for angular distribution effects. Curve B is the "hard" spectrum corresponding to $\mu = 3.64$ postfission neutrons per fission. The total neutron emission is expected to be the sum of this spectrum, a lower-energy evaporation

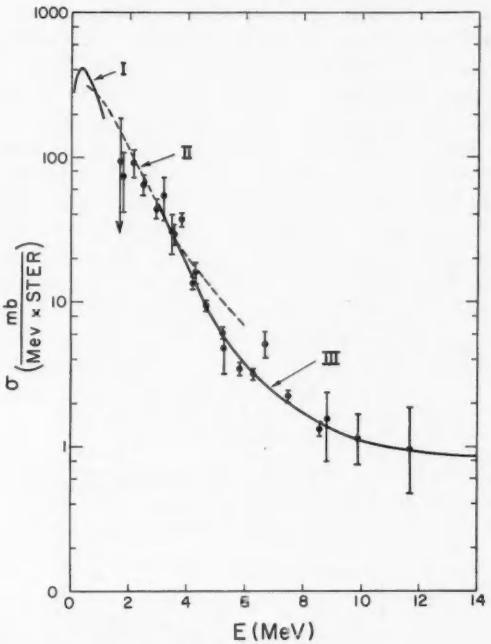

FIG. 2. The spectrum of neutrons observed at 90° from the scattering of 14-Mev neutrons from natural uranium. Curve I represents the data of Vasilev *et al.* (1957), curve II those of Zamyatnin *et al.* (1957). The experimental points are the data of Clarke (1961) and the errors shown are due to counting statistics only. Curve III is drawn through these data only to aid the eye.

spectrum, and a weak higher-energy component resulting from direct interaction processes. However, it appears that in the neighborhood of 5 Mev the calculated intensity of the fission spectrum alone is greater than the total observed intensity.

This suggests that not all the postfission neutrons are evaporated from the moving fragments. Curve C has been calculated on the assumptions that the moving fragments are at no higher temperature than in thermal-neutron-induced fission, and that the "excess" postfission-neutron emission occurs between the saddle point (where the nucleus is committed to fission) and the scission point (where it actually ruptures). Curve C has a total intensity of 2.81 neutron barns (2.40 neutrons per fission) and a correspondingly "soft" shape.

If curve C is subtracted from A the difference spectrum in the region below about 5 Mev has roughly the shape expected for evaporation from a nucleus having a single temperature T, i.e. $N(E) \propto Ee^{-E/T}$. Curve D is $N(E)/E$, and it will be seen that it is approximately exponential in shape with a temperature of 0.55 ± 0.07 Mev. The trend of curve D in the region above 4 Mev suggests

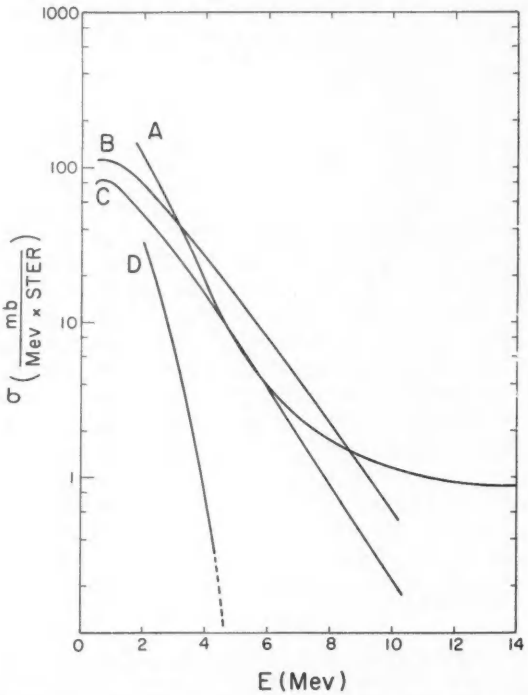

FIG. 3. A comparison of the smoothed experimental data (A) with fission-neutron spectra calculated on the assumption that all postfission neutrons are evaporated from the moving fragments (B) and that only 2.4 neutrons per fission are so evaporated (C). Curve D is the difference (A−C) divided by the energy (see text).

that too large a postfission contribution has been subtracted. However, an increase of about 15% in curve A in this region, which is within the experimental uncertainty, would remove the downward trend in D.

This value of T agrees with that of 0.48 ± 0.05 Mev given by Zamyatnin *et al.* (1958) for U^{238} and 14-Mev neutrons, but it is substantially lower than the temperatures of 0.75 to 1 Mev found by Graves and Rosen (1953) in the region of lead and bismuth. The difference is greater than expected from the combined effects of mass number on the level-density parameter and of the greater importance of the $(n,3n)$ reaction in uranium. Although it is not reasonable to expect that the complex evaporation phenomena occurring here can be accurately represented by a single nuclear temperature, a more elaborate analysis has not been tried because of the sensitivity of the upper part of the evaporation spectrum to the absolute amplitude of curve A and the assumptions made about the fission-neutron intensity.

To return to the fission neutrons, Batzel (1954) was apparently the first to mention the possibility of a substantial neutron emission between the

saddle point and scission. It may also be recalled that the angular distribution measurement of Harding and Farley (1956) implies that, out of the 13 neutrons emitted in the 147-Mev proton fission of uranium, the number emitted by the moving fragments (μ') is only 2.5 ± 1. In the present experiment μ' is determined essentially by the absolute intensity measurement in the 4- to 6-Mev region, which is accurate to about $\pm20\%$. Accordingly, $\mu' = 2.4-\delta\pm0.5$, where δ represents the correction for the tail of the evaporation spectrum; extrapolation with $T = 0.55$ Mev gives $\delta = 0.3_3$, i.e. $\mu' = 2.1\pm0.5$.

It should, however, be pointed out that there is another possible interpretation of the data. An alternative explanation of the observed low intensity near 5 Mev is that the neutrons are evaporated predominantly at right angles to the direction of motion of the fission fragments. Terrell (1959) has shown that an anisotropy of $(1-0.4\cos^2\theta)$ reduces the intensity at 5 Mev by about 5%. Thus an exceptionally large anisotropy would be required to explain the observed effect.

ACKNOWLEDGMENTS

The authors are grateful to K. W. Allen for his unpublished 14-Mev neutron data, to J. C. D. Milton for the results of his unpublished Datatron calculations of fission-neutron spectra, and to L. G. Elliott for helpful discussions.

REFERENCES

ALLEN, K. W. 1960. Private communication.
ALMQVIST, E. and CLARKE, R. L. 1955. Unpublished.
BATZEL, R. E. 1954. UCRL 4303.
BEYSTER, J. R., WALT, M., and SCHRANDT, R. G. 1956. Unpublished Los Alamos Report, *quoted by* Leachman (1958).
CLARKE, R. L. 1961. Can. J. Phys. **39**. This issue.
FLEROV, N. N., BEREZIN, A. A., and CHELNOKOV, I. E. 1958. Atomnaya Energ. **5**, 657.
FLEROV, N. N. and TALYZIN, V. M. 1958. Atomnaya Energ. **5**, 653.
FLEROV, N. N. and TAMANOV, E. A. 1958. Atomnaya Energ. **5**, 654.
FOREMAN, B. M., JR. and SEABORG, G. T. 1958. J. Inorg. & Nuclear Chem. **7**, 305.
GAUDIN, M. and LEROY, J. L. 1958. U.N. Geneva Conference, **16**, 106.
GRAVES, E. R., CONNER, J. P., FORD, G. P., and WARREN, B. 1958. Unpublished, *quoted by* Knight, Smith, and Warren (1958).
GRAVES, E. R. and ROSEN, L. 1953. Phys. Rev. **89**, 343.
HARDING, G. N. and FARLEY, F. J. M. 1956. Proc. Phys. Soc. A, **69**, 853.
HENKEL, R. L. and BROLLEY, J. E., JR. 1956. Phys. Rev. **103**, 1292.
HUGHES, D. J., MAGURNO, B. A., and BRUSSEL, M. K. 1960. Supplement No. 1 to Hughes and Schwartz (1958).
HUGHES, D. J. and SCHWARTZ, R. B. 1958. BNL 325, 2nd ed.
JOHNSTONE, I. 1956. AERE NP/R 1912.
KNIGHT, J. D., SMITH, R. D., and WARREN, B. 1958. Phys. Rev. **112**, 259.
LEACHMAN, R. B. 1958. U.N. Geneva Conference, **15**, 229.
LEBEDEV, P. P., ZISIN, IU. A., KLINTSOV, IU. S., and STSIBORSKI, B. D. 1958. Atomnaya Energ. **5**, 522.
MACGREGOR, M. H., BALL, W. P., and BOOTH, R. 1957. Phys. Rev. **108**, 726.
MILTON, J. C. D. 1958. Unpublished.
SMITH, R. K., HENKEL, R. L., and NOBLES, R. A. 1957. Unpublished Los Alamos Report, *quoted by* Leachman (1958) and Hughes and Schwartz (1958).
TERRELL, J. 1959. Phys. Rev. **113**, 527.
VASILEV, YU. A., ZAMYATNIN, YU. S., TOROPOV, P. V., and FOMUSHKIN, E. F. 1957. Atomnaya Energ. **3**, 540.
WAHL, J. S. 1954. Phys. Rev. **95**, 126.
ZAMYATNIN, YU. S., GUTNIKOVA, E. K., IVANOVA, N. I., and SAFINA, I. N. 1957. Atomnaya Energ. **3**, 542.
ZAMYATNIN, YU. S., SAFINA, I. N., GUTNIKOVA, E. K., and IVANOVA, N. I. 1958. Atomnaya Energ. **4**, 337.

APPENDIX

The Partial Cross Sections of U^{238} for 14.1-Mev Neutrons

The total non-elastic cross section at 14 Mev has been measured as 3.00±0.04 barns by Almqvist and Clarke (1955) and by Lebedev *et al.* (1958) as 2.91±0.14 barns. Beyster, Walt, and Schrandt (1956) give 2.89 barns, and an extrapolation of the data of MacGregor, Ball, and Booth (1957) gives 2.8±0.1. A value of 2.90 barns will be used here.

The fission cross section of U^{238} has been measured by Smith, Henkel, and Nobles (1957) as a function of neutron energy; at 14.1 Mev the total fission cross section is 1.17±0.05 barns.* Their results show that the competition between fission and neutron emission, which have similar "thresholds" in all the nuclei involved, is not very sensitive to an increase in excitation energy beyond the threshold. It is therefore possible to extrapolate with some confidence from lower energies to obtain values of 0.55±0.1 barns for $\sigma(n,f)$, 0.45±0.1 barns for $\sigma(n,nf)$, and 0.17±0.05 barns for $\sigma(n,2nf)$ at 14.1-Mev neutron energy.

Of the non-fission cross sections, $\sigma(n,\gamma)$ is negligible (Hughes and Schwartz 1958), $\sigma(n,n')$ has been measured by Clarke (1961) as 0.15±0.05 barns,† and $\sigma(n,2n)$ as 0.84±~0.15 barns at 14.1 Mev by Graves, Conner, Ford, and Warren (1958). $\sigma(n,3n)$ may then be obtained by difference, as $\sigma_{ne}-\sigma_t-\sigma(n,n')-\sigma(n,2n) = 0.74\pm\sim 0.16$ barns.

The Number of Neutrons Emitted in Fission

The number of neutrons evaporated from the different uranium isotopes is given directly by the values of the partial cross sections. The number of neutrons following fission can be calculated from the experimental data on ν for neutrons of different energies.

Probably the best values for ν in the thermal neutron fission of U^{235} and U^{233} are 2.43 and 2.50 respectively (Hughes *et al.* 1960). After subtracting the delayed neutron contributions and correcting for changes in excitation energy by taking $\partial\nu/\partial E = 0.14$ Mev^{-1} (see below), values of 2.35_0 and 2.37_5 for U^{236} and U^{234} at 6-Mev excitation are obtained. There are a large number of measurements for ν for the fission of U^{238} by neutrons of a few Mev energy (see Leachman 1958) which give a value of 2.50_8 for U^{239} with an excitation energy of 6 Mev. A value of ν appropriate to the fission of U^{237} at this excitation energy has been obtained by weighting the three values for U^{239}, U^{236}, and U^{234} inversely as the difference in mass; it is 2.40± ~0.05.

Values of ν for the 14-Mev fission of U^{238} have been reported as follows:

4.55±0.15, Gaudin and Leroy (1958);
4.50±0.32, Flerov and Talyzin (1958);
4.45±0.35, Flerov and Tamanov (1958);
4.12±0.25, Johnstone (1956).

*A rather lower value 1.13±0.05 barns at 14.6 Mev has been reported by Flerov, Berezin, and Chelnokov (1958).

†This value does not include the contribution from inelastic scattering events in which the neutron loses less than 0.5 Mev. It is the appropriate number to use in conjunction with the value given earlier for the total non-elastic cross section, since this also fails to include such low-energy-loss events.

The first of these measurements needs correcting for the revision of the value of ν in the thermal neutron fission of U^{235}. The second needs a correction for the effect of the (n,n') and $(n,3n)$ cross sections, which were ignored. With relative weights of 4, 1, 1, and 2, the weighted mean is 4.32 ± 0.12, which agrees well with an unpublished value of 4.31 ± 0.12 due to Allen (1960).

If it is assumed that the number of postfission neutrons per fission N_t is independent of mass number and increases linearly with excitation, then the values of N_t for U^{239} at 18.86 Mev and U^{238} at 13.1 Mev can be calculated from the value of $\nu(=N_t)$ for U^{237} at 6 Mev and the value of ν (which includes prefission evaporation) for the 14-Mev neutron fission of U^{238}. The value of $\partial N_t/\partial E$ deduced from the change of ν between 6 and 18.86 Mev is 0.14_2 Mev^{-1}. This value, which has been used above to correct ν values to a nuclear excitation of 6 Mev, is only slightly less than the value of $\partial\nu/\partial E$ since prefission evaporation requires about 6.5 Mev per neutron (see Table I). Values of $\partial\nu/\partial E$ in other nuclei are similar (Leachman 1958).

VERTICAL DISTRIBUTION OF SODIUM IN THE UPPER ATMOSPHERE[1]

W. R. Bullock and D. M. Hunten

ABSTRACT

The sodium twilight has been observed over the period October 1958 to December 1959 with a birefringent photometer. Abundances and vertical distributions have been found for 120 twilights. The abundance variation is similar to that found previously but is more nearly symmetrical about the solstices. A small seasonal variation in peak height is found, 3 to 5 kilometers with maximum in March. In general, changes in abundance cannot be correlated with changes in distribution; however, a few exceptions to this were found in June and July, when a large overnight increase in abundance accompanied a large decrease in the height of the whole distribution.

1. INTRODUCTION

There are many unsolved problems in the attempt to understand the behavior of atmospheric sodium. These have been discussed by Hunten (1956*b*), Omholt (1957), and Blamont, Donahue, and Stull (1958). The observations show a large abundance variation with its maximum in winter and minimum in summer; it would not be surprising if this were accompanied by a change in height or vertical distribution, but Hunten (1956*a*) found that no significant change in height could be observed at Saskatoon. This puts severe restrictions on any proposed explanation of the abundance variation. Since greatly improved methods of observation and of treating the observations are now available (Rundle, Hunten, and Chamberlain 1960; Hunten 1960), a further investigation seemed justified. This is all the more true since Montalbetti and McEwen (1959) have observed a considerable height variation at Churchill, which is only 7° further north than Saskatoon. Moreover, their abundance variation has a somewhat different shape from the one observed at Saskatoon, and a still different shape has been found by Blamont and Donahue (1958) at a latitude of 44°. The new measurements show a small but apparently significant height variation of 3 to 5 kilometers with maximum in March; this is exactly out of phase with the smaller variation found by Hunten (1956*a*), which was not considered significant. The abundance variation is now found to be nearly symmetrical about the solstices and thus resembles the results of Montalbetti and McEwen.

2. OBSERVATIONAL METHOD

The photometer which was used has been described by Rundle, Hunten, and Chamberlain (1960). It includes a birefringent filter of the type now widely used for airglow studies, mounted in a large vertical telescope which observes near the zenith. Electrical compensation is used to eliminate the

[1]Manuscript received February 10, 1961.
Contribution from the Department of Physics, University of Saskatchewan, Saskatoon, Saskatchewan. Supported by the Geophysics Research Directorate of the Air Force Research Division, Air Research and Development Command, under Contracts No. AF 19(604)-1831 and AF 19(604)-7265.

signal caused by the Rayleigh component of the twilight. The field of view is rotated around the zenith to permit a direct measurement of the derivative of sodium intensity versus shadow height; we will call this ΔB. The derivative may also be calculated numerically from the ordinary record of total intensity; this version will be called $\dot{B}$. In principle, as explained by Rundle, Hunten, and Chamberlain, ΔB is preferable to $\dot{B}$, but we have found in practice that ΔB is less useful because its signal-to-noise ratio is lower.

$\dot{B}$ was found from the chart records in the following way. Intensity (B) was measured at 1-minute intervals and punched into computer tape. The computer calculated the geometrical shadow height (z_1) for each of these times, and then the ratio $[B(t)-B(t+3 \text{ min})]/[z_1(t)-z_1(t+3 \text{ min})]$ which can be taken as $\dot{B}$ (that is, dB/dz_1) for the average z_1. To find the distribution, the procedure given by Hunten (1960) was used: $\dot{B}$ was plotted against $(z_1+\bar{x})$ with $\bar{x}$ taken in the range 26.3 to 27.0 km according to season, and a smooth curve drawn.* The self-absorption correction tabulated by Hunten was applied when the abundance was large. Then the Bracewell chord-correction method was applied to unfold the distribution from the curve, using a chord appropriate to the season. The ΔB data were plotted in the same way, after removing the geometrical factors discussed by Rundle, Hunten, and Chamberlain (1960), and the Bracewell treatment applied.

A typical result is shown in Fig. 1 where the results from $\dot{B}$ and ΔB are seen to agree well. Both curves show negative densities around 70 km; this effect was general in all the runs made and was also found by the matrix method used by Rundle, Hunten, and Chamberlain. The Bracewell procedure does produce small oscillations as shown by Hunten (1960), but these are much smaller than the one in Fig. 1. The error was finally traced to an instrumental defect: during the bright part of twilight, the noise level from the white light is very large and was overloading the phase-sensitive detector. The result was to reduce its sensitivity to the sodium signal; therefore, the derivative goes to zero too quickly and may even go negative. The effect was demonstrated experimentally with an artificial interfering signal to simulate the noise, and found to be of the right order of magnitude. One or two twilight runs were made at reduced sensitivity; they gave good distributions as expected with no negative densities.

Since the reason for the error was not discovered until after all the observations had been made, it was necessary to find a method of correcting them. The overload is serious only when the white light is bright, that is, for depression angles less than about 7° corresponding to a shadow height of 48 km or a sodium height of $(48+\bar{x}) = 75$ km. Therefore, the part of the distribution above this should be little affected, and the part below, as observed, too small or even negative. A reasonable correction can be made by extending the curve from 75 km smoothly to the axis at 55 or 60 km, since there is good evidence from earlier work that there is little or no free sodium below this height. Such corrected curves are shown in Fig. 1.

The density scale was found by measuring the "plateau" brightness corre-

*$\bar{x}$ can be regarded as a screening height, that is, the effective height of the shadow of the atmosphere and ozone layer.

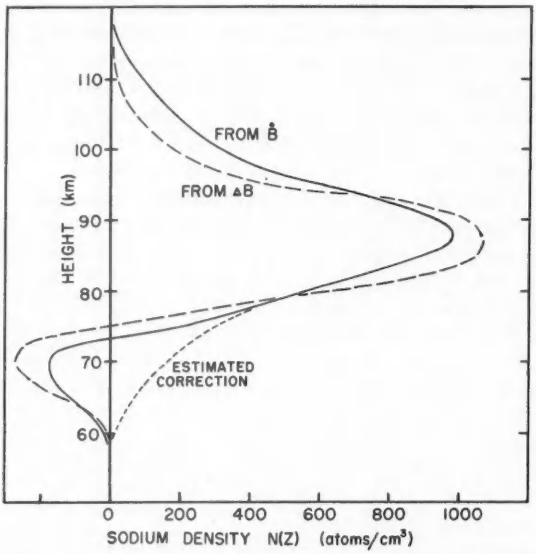

FIG. 1. Sodium distributions measured January 24, 1959, in morning twilight. The one labelled $\dot{B}$ was found from the derivative calculated from the total intensity; the one labelled ΔB, from the directly measured derivative. As described in the text, the dotted lines are believed to give a nearly correct distribution from 50 to 75 km.

sponding to a solar depression angle of 6.5°; at this angle, the whole sodium layer is fully illuminated. Because of the instrumental error just discussed, the values recorded were too low and were multiplied by a factor 1.15. This was estimated from several distributions similar to Fig. 1 by comparing the areas under the corrected and uncorrected curves, counting the part to the left of the axis as negative.

The resulting brightness was converted to an abundance by Fig. 3 of Chamberlain, Hunten, and Mack (1958). The calculations of Blamont, Donahue, and Stull (1958) are probably more accurate, but the difference is less than the uncertainty in the solar intensity; we preferred to use the results of Chamberlain, Hunten, and Mack to facilitate comparison with our earlier measurements given there.

RESULTS

Average Distributions

These were found by averaging the data for $\dot{B}$ and applying the chord correction to the result. It would perhaps have been preferable to average the distributions themselves, but this would have been much more difficult because they were available in graphical form only. The average distribution for each quarter is shown in Fig. 2; a strong seasonal variation of abundance is present and there is indication of a small height variation. The shape of the distribution does not change appreciably and it seems to be symmetrical about the peak.

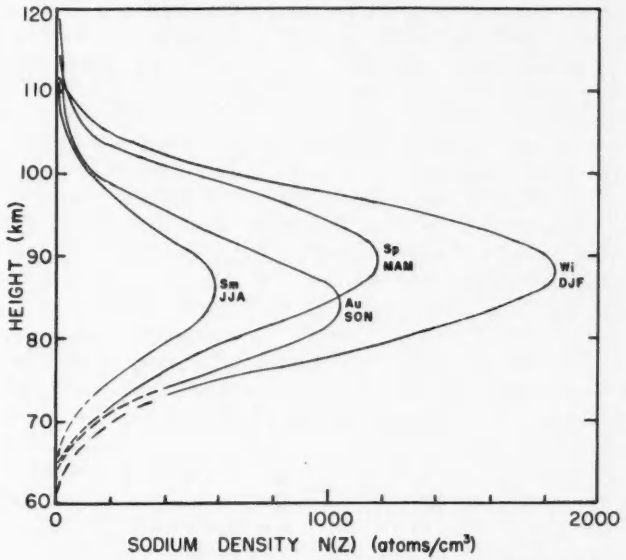

FIG. 2. Average distributions for each season of the year.

Seasonal Variations

The abundances found are plotted in Fig. 3 along with a sine curve found by harmonic analysis of the monthly means. The results observed previously

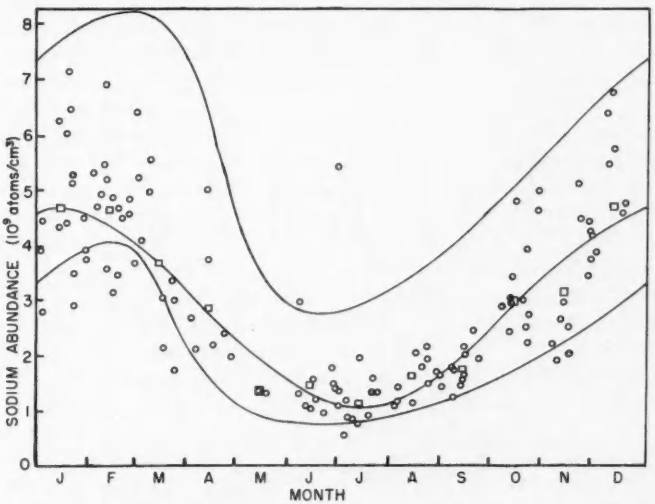

FIG. 3. Annual variation of abundance. Large squares denote monthly means, and the sine curve is from their harmonic analysis. The other two curves are the "extremes" transferred from Fig. 4 of Chamberlain, Hunten, and Mack (1958).

at Saskatoon (Chamberlain, Hunten, and Mack 1958) are indicated by the two "extreme" lines given in Fig. 4 of that paper; actually, about half a dozen points lay outside these "extremes". The agreement of general magnitudes in the two sets of measurements is surprisingly good, considering the difficulty of standardizing a calibrator containing a sodium lamp. The large "spring hump" which was so evident in the earlier results has disappeared, and the sine curve drawn through the monthly means represents them well. Its extremes are 4.7×10^9 atoms/cm^2 and 1.0×10^9, about 3 weeks after the solstices. These times cannot be considered accurate to better than 3 or 4 weeks. Part of the "random" variation about the average may be due to observational difficulties, but most of it is believed to be real. The largest abundance was about 7×10^9 atoms/cm^2 and the smallest about 0.6×10^9.

A quantity called "70% peak height" was found from each distribution; it is the average height of the two points having densities 70% of the peak value. Such a measure is expected to be less affected by noise than the position of the peak itself. The harmonic analysis gave a maximum height of 88.0 km in March and a minimum of 85.2 km in September. The average distributions shown in Fig. 2 suggest a slightly larger variation, from 89 to 84 km. Individual heights were mostly between 82 and 92 km, with a few outside these limits.

The "20% thickness" of the layer was defined as the height difference between the two points at 20% of the peak density. There was some sign of seasonal variation, but it is not considered significant; the mean value is about 29 kilometers.

"Random" Variations

All the quantities measured showed large variations about the means for

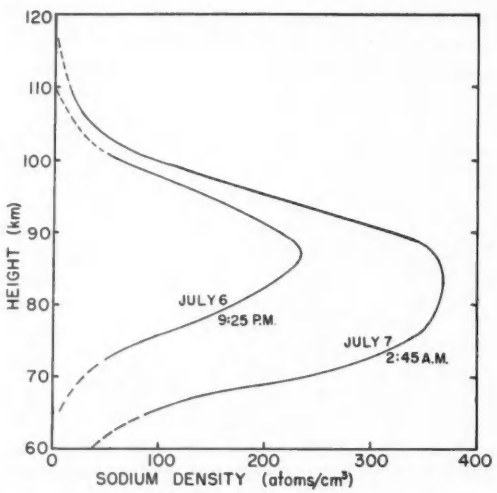

FIG. 4. One of the summer events in which a sudden large increase in abundance seems to be confined to the lower part of the sodium layer.

a given time, a behavior which has been reported in many earlier papers. The variations are not really random, since there are many occasions when two or three successive results agree closely, but they are certainly unpredictable. Almost without exception, no correlation could be found between the sudden changes in the various parameters described above. Large overnight increases in abundance occurred once in June and four times in July; on all five occasions, a proportional decrease in peak height was found, so that the density above the original peak was almost unchanged (see the example in Fig. 4). It is interesting that a similar occurrence was observed by Rundle, Hunten, and Chamberlain (1960), but in May and over an interval of 3 days. In these few cases, the change in abundance appears to have been caused by a lowering of the height at which sodium compounds become almost completely dissociated, but this mechanism does not explain the changes observed during the rest of the year, nor the seasonal variation.

4. DISCUSSION

The seasonal variation of abundance at Saskatoon (52° N.) has been given, from earlier measurements, by Chamberlain, Hunten, and Mack (1958). The present results are similar except that they do not show the pronounced hump at the end of March and give an average variation which is much more nearly symmetrical about the solstices. At Churchill (59° N.) McEwen and Montalbetti (1959) have found a similar variation whose amplitude may be slightly smaller. But at Haute-Provence Observatory (44° N.) Blamont and Donahue (1958) find a considerably different curve with two very high maxima in December and March and a low, almost constant value for the rest of the year. (If their peaks were plotted on Fig. 2, they would be off-scale by factors of $2\frac{1}{2}$ to 4.) And recently Donahue (1960) has found still different results at 23° N. in the Sahara. We thus have indications of a strong latitude variation, much stronger than the hemisphere-to-hemisphere effect which has been postulated up to now.

This suggestion is reinforced by the height measurements. The Churchill results give a variation of 10 kilometers with minima in February and November, maxima in May and December. At Saskatoon we find a smaller variation, 3 to 5 kilometers, with only one maximum in March. Earlier results (Hunten 1956*a*) gave a still smaller variation of just the opposite phase; it was not considered significant since the measurements then available were much poorer than the present ones. At Haute-Provence, Donahue (1960) gives a variation of the same magnitude as at Churchill but with a deep minimum in June when Churchill is near its major maximum. The behavior in the Sahara is even more violent and does not resemble any of the others.

It thus appears that a detailed study of the seasonal and geographical variations will require a network of many stations and several years' observation. Particular attention should be paid to the southern hemisphere. The effort required for such a program is considerable, but the results may shed light on the meteorology of a part of the atmosphere which is difficult to study by other means.

ACKNOWLEDGMENTS

Much of the labor of reading charts and plotting results was done by B. G. Pratt and D. J. McKay. T. M. Donahue and R. Montalbetti were most generous in communicating and discussing their results.

REFERENCES

BLAMONT, J. E. and DONAHUE, T. M. 1958. Compt. rend. acad. sci. (Paris), **247**, 496.
BLAMONT, J. E., DONAHUE, T. M., and STULL, V. R. 1958. Ann. géophys. **14**, 253.
CHAMBERLAIN, J. W., HUNTEN, D. M., and MACK, J. E. 1958. J. Atmospheric and Terrest. Phys. **12**, 153.
DONAHUE, T. M. 1960. Paper given at the Copenhagen Symposium on Aeronomy, July.
HUNTEN, D. M. 1956*a*. The airglow and the aurorae, *edited by* E. B. Armstrong and A. Dalgarno (Pergamon Press, London), p. 114.
——— 1956*b*. The airglow and the aurorae, *edited by* E. B. Armstrong and A. Dalgarno (Pergamon Press, London), p. 183.
——— 1960. J. Atmospheric and Terrest. Phys. **17**, 295.
MONTALBETTI, R. and MCEWEN, D. J. 1959. Paper given at the meeting of the Canadian Association of Physicists, June.
OMHOLT, A. 1957. J. Geophys. Research, **62**, 207.
RUNDLE, H. N., HUNTEN, D. M., and CHAMBERLAIN, J. W. 1960. J. Atmospheric and Terrest. Phys. **17**, 205.

RADIO-FREQUENCY BREAKDOWN CONTROLLED BY DRIFT OF ELECTRONS IN AN INHOMOGENEOUS MAGNETIC FIELD[1]

L. T. SHEPHERD AND H. M. SKARSGARD

ABSTRACT

A study has been made of r-f. breakdown in which the controlling loss mechanism arises from the drift of electrons in an inhomogeneous magnetic field. The study was carried out using a toroidal system with parallel r-f. electric and steady magnetic fields. An approximate average-electron theory of drift-controlled breakdown is presented. Experimental measurements of breakdown r-f. electric field versus magnetic field were made at various pressures from 1.25 to 6.0×10^{-3} mm of Hg, using hydrogen and helium gases. A radio frequency of 8 Mc/sec was used. Magnetic fields up to 2000 gauss were employed. The r-f. breakdown field was found to vary as the inverse square root of the magnetic field as predicted by the theory.

I. INTRODUCTION

Breakdown in a gas involves a sudden, large increase in the density of electrons and positive ions. In r-f. breakdown the production phenomenon is the primary ionization caused by relatively few electrons, initially present in the gas, receiving power from the r-f. field. At the same time electrons are lost from the gas by one or more loss mechanisms. The competition between the production and loss mechanisms determines the conditions required for breakdown. When the production rate exceeds the loss rate a sudden build-up of the degree of ionization occurs.

Various types of breakdown in gases have already been studied by several workers. A review of this work has recently been made by Brown (1959). Most of the previous work has been done on diffusion-controlled high-frequency breakdown in which the dominant loss mechanism is diffusion of the electrons through the gas to the walls of the chamber.

In this paper a study is reported of r-f. breakdown controlled by the loss of electrons due to drift in an inhomogeneous magnetic field. So far as is known no previous study of this type of breakdown has been reported. The work was initiated in connection with an experiment being planned at this laboratory on betatron acceleration of electrons in plasma (Skarsgard 1959). In this experiment the plasma is to be formed within a toroidal vacuum chamber by striking a r-f. discharge in a gas at low pressure. In previous experiments of this kind (Reynolds and Skarsgard 1958, 1959) a similar scheme of plasma formation was successfully employed without much understanding of the process of r-f. breakdown involved.

The study of r-f. breakdown has been carried out with a system shown in Fig. 1. A discarded Allis-Chalmers betatron donut was employed as the

[1]Manuscript received February 13, 1961.
Contribution from the Physics Department, University of Saskatchewan, Saskatoon, Saskatchewan.

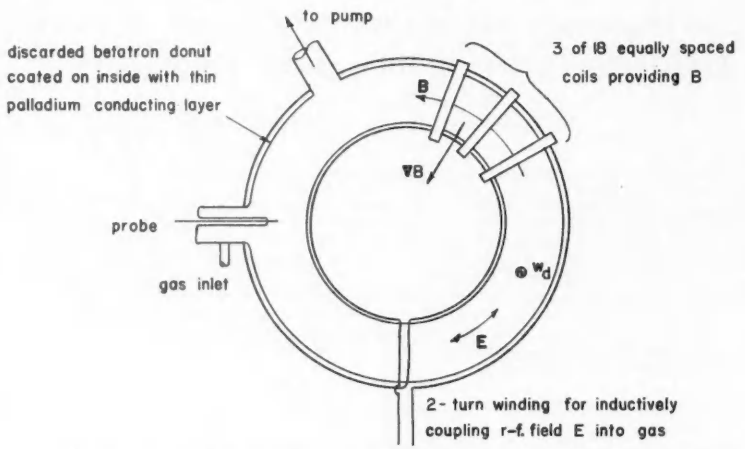

FIG. 1. Toroidal system used for study of r-f. breakdown.

vacuum chamber. Breakdown at low pressure was facilitated by a "steady" magnetic field **B** parallel to the direction of the r-f. electric field **E**. The coils used to provide these fields are indicated in Fig. 1.

II. THEORY

An accurate theoretical description of r-f. breakdown can only be given in terms of the velocity distribution function for the electrons. Here an average-electron theory is presented in an attempt to predict the broad features to be expected in r-f. breakdown controlled by drift of electrons in an inhomogeneous magnetic field. The rates of ionization and loss of electrons are determined in terms of average properties of the electrons. Since the degree of ionization is extremely small at the beginning of breakdown, conditions for breakdown can be examined without considering such plasma phenomena as ambipolar diffusion, plasma oscillations, or instabilities.

II.1. Average-electron Theory of Drift-controlled Breakdown

The magnetic field B of Fig. 1 is inhomogeneous, increasing toward the axis of the system as shown. When an electron moves in an inhomogeneous field of this nature it experiences a drift in the direction of $\nabla B \times \mathbf{B}$ (Spitzer 1956) with a speed

$$w_d = \frac{w_\perp^2}{2\omega_c R} + \frac{w_\parallel^2}{\omega_c R}, \tag{1}$$

where $\omega_c = qB/m$ is the cyclotron frequency for the electron,

R is the radius of curvature of the magnetic lines of force,

$w_\perp, w_\parallel$ are the components of electron velocity perpendicular and parallel to the magnetic lines of force, and

w_d is the speed of drift of the instantaneous center of gyration.

Mixed Gaussian units are employed unless otherwise noted.

Equation (1) is derived from a first-order theory and its validity demands that B be large enough so that $w_d \ll w$, the particle velocity. The first term on the right of (1) is the so-called "gradient drift" arising from ∇B. The second term is a consequence of the centrifugal force experienced by the electron moving along the curved magnetic lines of force.

The electron drift given by (1) leads to a loss of electrons from the gas inside the chamber. The name "drift-controlled breakdown" is given in this paper to r-f. breakdown in which the controlling loss mechanism is this drift of electrons toward the walls of the chamber. Breakdown occurs when the rate of production of electrons due to ionization exceeds the rate of loss of electrons due to drift. The condition for equality of the rates of production and loss is called the breakdown condition and may be expressed by the equation

$$\nu_i = \nu_{\text{drift}} \tag{2}$$

where ν_i is the average rate of production of electrons per electron due to ionization and ν_{drift} is the average rate of loss of electrons per electron due to drift.

First consider ν_i. In the absence of collisions an electron oscillating in a r-f. electric field gains no energy on the average. However, elastic collisions with the neutral gas atoms alter the phase relationship between the r-f. field and the electron velocity so that power is received by the electrons. Kinetic energy of directed motion gained from the r-f. field between collisions is transformed into kinetic energy of random motion upon collision. In this way the kinetic energy can be increased in successive collisions until the electron has acquired sufficient energy to ionize a gas atom. The average power received by an electron from a r-f. electric field (Brown 1959) is given by

$$P = \frac{q^2E^2}{m} \frac{\nu_m}{\nu_m^2+\omega^2}, \tag{3}$$

where ν_m is the frequency of collision for momentum transfer,
ω is the angular frequency of the r-f. field,
E is the r.m.s. field.

If all the power goes into ionization, the ionization rate per electron is P/qu_i where u_i is the ionization potential for the gas under consideration. In general, part of the power gained from the r-f. field will be spent in excitation of the gas atoms resulting in subsequent emission of optical radiation. Generally, also, part of the power goes into heating up the gas atoms through the elastic collisions with the electrons; however, for the low pressures considered here power dissipated in this way can be shown to be negligible. In any case

$$\nu_i = \frac{P}{K_1 q u_i} = \frac{qE^2}{K_1 m u_i} \frac{\nu_m}{\nu_m^2+\omega^2} \tag{4}$$

where K_1 is a factor, greater than unity, which accounts for the fact that only part of the power goes into ionization. It is assumed that K_1 is constant for

any given gas. In equation (4) ν_m should be averaged over all the electrons. However, for hydrogen and helium, the gases considered in this work, ν_m is approximately independent of electron energy, at least for energies above a few electron volts (Brown 1959).

Now consider ν_{drift}. If $\bar{z}$ is the average distance to the chamber wall in the direction of the electron drift

$$\nu_{drift} = \frac{(w_d)_{average}}{\bar{z}} . \tag{5}$$

Averaging the drift velocity given by (1) over all the electrons gives

$$\nu_{drift} = \frac{K_2 v^2}{\omega_c R \bar{z}} \tag{6}$$

where v is the root mean square electron velocity and K_2 is a factor, assumed constant, which depends on the electron velocity distribution. For a purely random velocity distribution $K_2 = \frac{2}{3}$. However, for the low pressures studied in this work there is significant peaking of the velocity distribution in the direction of the r-f. electric field. This leads, furthermore, to a non-zero average magnetic force on the electrons due to the r-f. magnetic field produced by the r-f. winding. This magnetic force affects the average electron drift velocity and consequently the value of K_2 to an extent which is difficult to determine for the system used.

Substituting for ω_c and putting $v^2 = 2q\bar{u}/m$ gives

$$\nu_{drift} = 2K_2 \frac{\bar{u}}{BR\bar{z}} . \tag{7}$$

Equations (2), (4), and (7) then determine E_b, the electric field required for breakdown.

$$E_b = K\left[\frac{2m\bar{u}u_1}{qBR\bar{z}} \frac{\nu_m^2+\omega^2}{\nu_m}\right]^{1/2} \tag{8}$$

where $K = (K_1K_2)^{\frac{1}{2}}$. This result is valid only if B is large enough to satisfy the criterion for validity of the first-order drift theory employed. Thus, the apparent singularity at $B = 0$ has no significance.

For the system used (Fig. 1) R is 19 cm and $\bar{z}$ is approximately 2 cm. For hydrogen, taking $\bar{u} = u_1 = 15.4$ volts gives

$$E_b\left(\frac{\text{volts}}{\text{cm}}\right) = \frac{0.84\times10^{-3}}{B^{1/2}} K_{(H_2)} \left(\frac{\nu_m^2+\omega^2}{\nu_m}\right)^{1/2} . \tag{9}$$

The value of ν_m depends on the gas pressure according to the approximate relationship $\nu_m = 5.93\times10^9\, p$ where p is in mm of Hg. For helium, taking $\bar{u} = u_1 = 24.5$ volts gives

$$E_b\left(\frac{\text{volts}}{\text{cm}}\right) = \frac{1.34\times10^{-3}}{B^{1/2}} K_{(He)} \left(\frac{\nu_m^2+\omega^2}{\nu_m}\right)^{1/2} . \tag{10}$$

For helium $\nu_m = 2.37\times10^9\, p$. The ionization potentials and collision frequencies for hydrogen and helium are taken from Brown (1959).

It is notable that the predicted breakdown field for both gases varies inversely as the square root of the magnetic field. This relationship appears to be unique for drift-controlled r-f. breakdown.

II.2. Possible Importance of Other Loss Mechanisms

Here the relative importance of loss mechanisms other than electron drift in the inhomogeneous magnetic field will be examined.

Diffusion

If diffusion of electrons to the walls of the chamber is the dominant loss mechanism the loss rate can be found from a solution of the diffusion equation. When a magnetic field is present the diffusion loss rate per electron, ν_{diff}, can be expressed (Brown 1959) in the average-electron approximation by

$$\nu_{\text{diff}} = \bar{D}/\Lambda_e^2 \tag{11}$$

where $\bar{D} = (v^2/3\nu_m)_{\text{average}}$ is the average diffusion coefficient, assuming a random velocity distribution for the electrons, and Λ_e is the equivalent diffusion length for the system. For a cylindrical chamber of length L and radius r, with a longitudinal magnetic field, Λ_e is given by

$$\frac{1}{\Lambda_e^2} = \frac{\nu_m^2}{\nu_m^2+\omega_c^2}\left(\frac{2.405}{r}\right)^2+\left(\frac{\pi}{L}\right)^2. \tag{12}$$

The magnetic field effectively increases the chamber dimensions perpendicular to the field, reducing the diffusion to the walls.

For the present purposes the toroidal chamber of Fig. 1 may be represented by an endless cylinder of mean radius $\bar{r}$ between 2 and 3 cm. Equation (12) then gives

$$\frac{1}{\Lambda_e^2} = \frac{\nu_m^2}{\nu_m^2+\omega_c^2}\frac{1}{\Lambda^2} \tag{13}$$

with Λ approximately equal to 1 cm. If ν_m is independent of electron energy equations (11) and (13) give

$$\nu_{\text{diff}} = \frac{v^2}{3\nu_m}\frac{\nu_m^2}{\nu_m^2+\omega_c^2}\frac{1}{\Lambda^2}. \tag{14}$$

From (6) and (14)

$$\frac{\nu_{\text{drift}}}{\nu_{\text{diff}}} = \frac{3K_2\Lambda^2}{R\bar{z}}\frac{1+(\omega_c/\nu_m)^2}{\omega_c/\nu_m}. \tag{15}$$

In obtaining this result the possibility that one loss mechanism affects another, through its influence on the electron velocity or space distribution for example, is ignored. It should be noted, however, that both ν_{drift} and ν_{diff} have the same dependence on the mean square velocity so that the ratio given by (15) is not explicitly dependent on the mean electron energy.

A rough estimate of the ratio of drift and diffusion loss rates for the system of Fig. 1 may be obtained by putting in equation (15) $\Lambda = 1$ cm, $R = 19$ cm, $\bar{z} = 2$ cm, and $K_2 = 1$. For hydrogen, taking $B = 200$ gauss and $p = 2.5\times10^{-3}$

mm Hg, equation (15) then gives $\nu_{drift}/\nu_{diff} \simeq 19$. Similarly for helium, with $B = 200$ gauss and $p = 6\times10^{-3}$ mm Hg, equation (15) gives $\nu_{drift}/\nu_{diff} \simeq 20$. For lower pressures or higher magnetic fields these ratios increase. Thus for the conditions under which breakdown measurements have been carried out, loss of electrons due to drift in the inhomogeneous magnetic field should be roughly an order of magnitude more important than loss by diffusion.

Electron Attachment

The possibility of electron attachment to neutral gas atoms providing a competing loss mechanism has been examined. Oxygen has a relatively large cross section for electron attachment. Estimates for the concentration of air impurity in the gas together with measured electron attachment cross sections for air (Harrison and Geballe 1953) were used to calculate the rate of loss of electrons to be expected from this phenomenon. It was concluded that electron losses due to attachment would be approximately two orders of magnitude less than drift losses.

III. EXPERIMENTAL DETAILS

Observations of r-f. breakdown have been made in hydrogen and helium. Commercial grades of these gases were used; the specified impurity content was less than 0.2 mole per cent for hydrogen and less than 0.01 mole per cent for helium. Measurements of breakdown r-f. field, E_b, versus magnetic field, B, were made at various pressures in the range 1.25 to 6.0×10^{-3} mm Hg. A r-f. frequency of 8 Mc/sec was used. Magnetic fields up to 2000 gauss were employed.

A photograph of the apparatus is shown in Fig. 2. Initially gas is allowed into the vacuum chamber (donut) until the desired pressure is reached. The breakdown field is found by using pulsed r-f. and magnetic fields. Each pulsed operation is initiated by a push button, controlled by conventional electronic trigger and delay circuits (Fig. 4), and proceeds as follows. The push button activates a trigger circuit, which, in turn, initiates the time sequencing and also fires the B supply, connecting a charged condenser bank across the coils used to provide the magnetic field. The current through these coils reaches a maximum after $\sim$1 msec, at which time the r-f. oscillator is turned on for a period of $\sim$200 μsec. The magnetic field B is nearly steady during the time the r-f. is on (Fig. 3). The r-f. field is increased in successive pulsed operations until breakdown is observed. Then the donut is flushed out with the gas under study, pumped down to a pressure of $\sim10^{-4}$ mm Hg, and the cycle is repeated for a different value of B.

The breakdown can usually be observed visually. However, a probe method was found more reliable. The unshielded tip of the probe extends into the donut (Fig. 1) and is connected through a high impedance to the grounded coating of the donut. At the moment of breakdown the probe (and presumably the plasma in contact with it) swings negative by as much as several hundred volts, providing a clearly recognizable signal on an oscilloscope trace. The generation of this large voltage is not at present well understood.

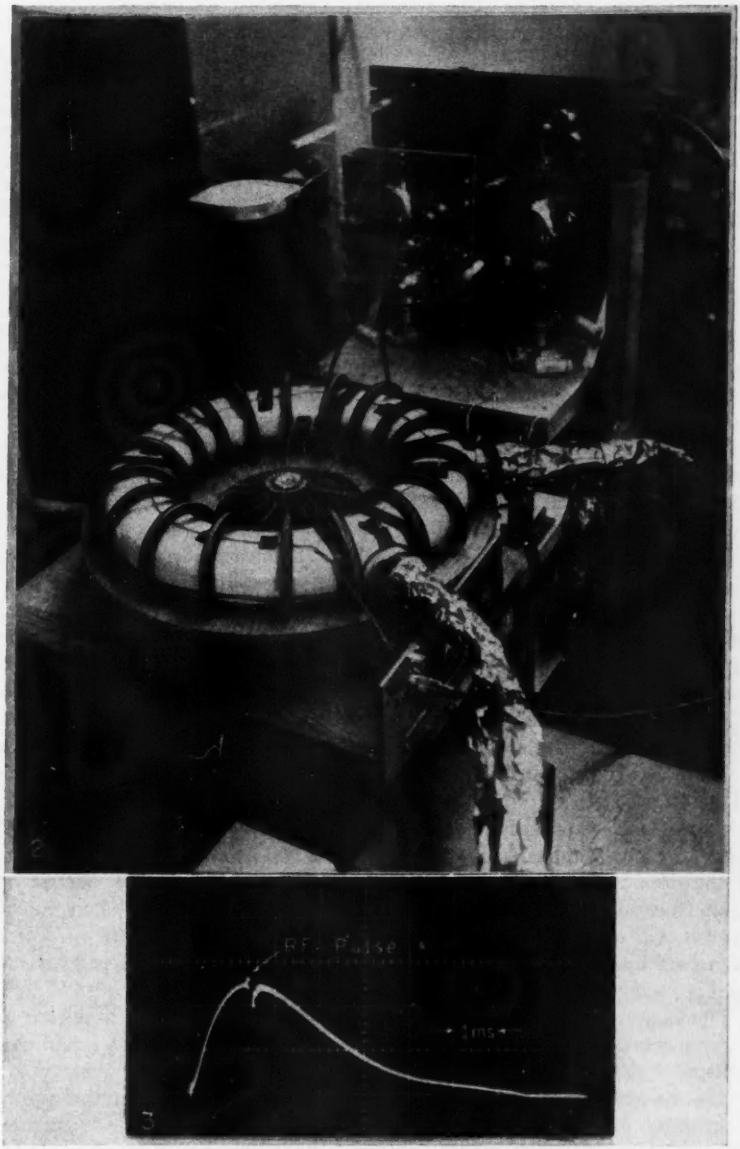

FIG. 2. Photograph of part of the apparatus including the toroidal vacuum chamber (donut).

FIG. 3. Oscillogram showing the time scale for the magnetic field and the r-f. electric field. The envelope of the pulsed r-f. is superimposed on a Rojofsky coil measurement of the current through the coils providing the magnetic field.

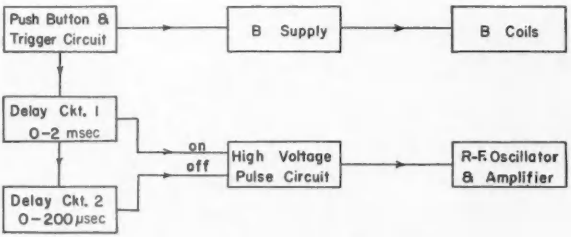

FIG. 4. Block diagram of electronics.

The B supply employs a 20,000-μf bank of electrolytic condensers with a voltage rating of 450 volts. A 5550 ignitron switch is used to connect the condenser bank to the parallel connection of 18 coils, of 70 turns each, equally spaced around the donut. High current silicon diodes (International Rectifier type 45LR70) are used to protect the electrolytic condensers against reverse voltage. Calibration of the B supply was carried out by Rojofsky coil measurements of the maximum current versus initial condenser voltage. A check was made on this calibration by direct measurement of the magnetic field inside the donut, using a small test coil.

The r-f. circuit (behind the donut in Fig. 2) consists of a Colpitts oscillator followed by an amplifier whose tank circuit is tuned to the frequency of the Colpitts oscillator. The two turns wound around the donut (Fig. 1) provide the inductance of the tank circuit and inductively couple the r-f. electric field into the gas. The duration of the r-f. is controlled by the high voltage pulse providing the plate voltage for the Colpitts stage. The value of the r-f. electric field is controlled by the adjustable voltage on a 5-μf condenser providing the plate voltage for the amplifier stage. Plate voltages of up to 16 kv were employed on the Eimac 6C21 triode used as the amplifier tube. Corresponding r-f. fields of up to 6 volts/cm (r.m.s.) were induced inside the donut. Calibration of the r-f. field versus amplifier plate voltage was based upon measurement of the r-f. voltage induced around a single-turn coil inserted around the interior of the donut. This determination therefore gives the average electric field around the donut. Since the voltage around the single turn was inconveniently large it was compared, at low amplifier plate voltage, with the r-f. voltage picked up by a small coil coupled loosely to the r-f. turns; this coil was then used to calibrate the oscillator.

The vacuum system included a mercury diffusion pump with liquid air trap and an isolation and baffle valve. Pressures were measured by a pirani gauge calibrated against a McLeod gauge and an ionization gauge.

The various calibrations involve uncertainties, especially in the absolute magnitude of the quantities involved. Estimated probable errors are: $E \sim 15\%$, $p \sim 10\%$, $B \sim 15\%$.

IV. RESULTS AND DISCUSSION

Figures 5 and 6 show the experimental results together with the normalized results of the simple average-electron theory of drift-controlled breakdown.

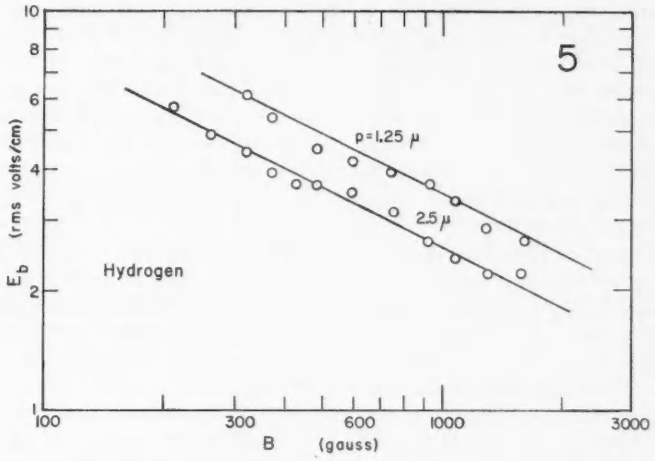

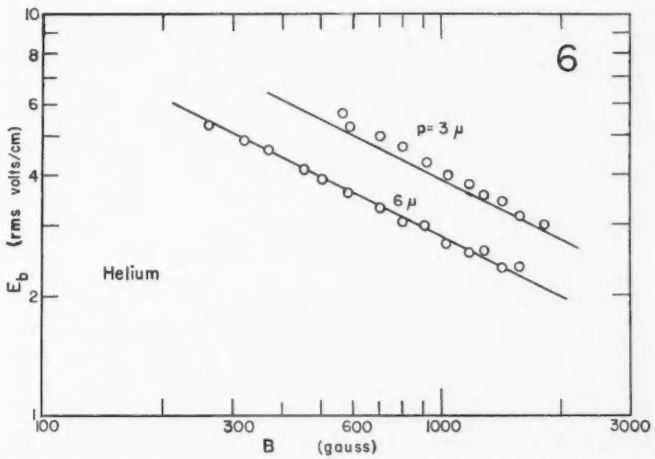

FIG. 5. Breakdown r-f. electric field versus magnetic field for hydrogen. Points are measured values. Straight lines are theoretical with $K_{(H_2)} = 7.0$ in equation (9).

FIG. 6. Breakdown r-f. electric field versus magnetic field for helium. Points are measured values. Straight lines are theoretical with $K_{(He)} = 4.8$ in equation (10).

On a log plot the predicted dependence of breakdown field on the magnetic field appears as a straight line of slope minus one-half. The normalization of the theory for hydrogen was made by arbitrarily drawing a line of slope minus one-half through the experimental points for a pressure of 2.5 microns. This gives $K_{(H_2)} = 7.0$ in equation (9). Similarly, for helium, fitting the theory to the experimental results for a pressure of 6.0 microns gives $K_{(He)} = 4.8$.

Within the accuracy of the measurements, indicated by the scatter of the points, the breakdown field appears to vary as the inverse square root of the

magnetic field as predicted by the theory. Also the predicted increase of breakdown field with decreasing pressure is in fair agreement with the experimentally observed dependence, although with measurements at only two pressures for each gas a conclusive test of the theory in this respect cannot be claimed. It should be pointed out also that the dependence of breakdown field on pressure, indicated by (9) and (10), is not unique for drift-controlled breakdown; it only describes the effectiveness of energy transfer to the electrons from the electric field through collisions and is therefore not directly connected with the loss mechanism.

Without more knowledge of the electron velocity distribution the significance of the values obtained for $K_{(H_2)}$ and $K_{(He)}$ cannot be determined conclusively. The larger value obtained for $K_{(H_2)}$ is possibly connected with greater excitation losses of power in hydrogen. In hydrogen there are excitation levels well below the ionization potential whereas in helium the lowest excitation level is at 19.8 volts, not much below the ionization potential.

The maximum electric field available with the present system determines the lowest pressure at which useful breakdown observations can be made. Measurements were attempted at higher pressures but results were irreproducible and inconsistent with the results at lower pressure. The reasons for this are not clear. There is evidence, at pressures as high as 10^{-1} mm Hg, that breakdown occurs at localized regions within the donut. This suggests regions of stronger r-f. electric field due, perhaps, to nonuniformities in the conductive coating on the inside of the donut. Such effects could lead to localized discharges provided the oscillation amplitude of the electrons is small compared to the geometrical scale of the nonuniformities. At pressures and r-f. fields indicated in Figs. 5 and 6 the estimated oscillation amplitude is several centimeters, and decreases with increasing pressure (and decreasing r-f. field). Since this is small compared with the circumference of the donut, difficulties may be expected due to irregularities in the r-f. field and could possibly account for the curious behavior at higher pressure.

The considerable spacing of the coils providing the magnetic field (Fig. 1) leads to inhomogeneities in the field along the direction of **B**. The system resembles somewhat the "bumpy torus" investigated by Gibson, Jordan, and Lauer (1960). Under certain conditions and over restricted regions of the torus cross section these workers found closed precessional orbits for the single particle drift motion perpendicular to the magnetic field. Such effects of "bumpiness" in the system of Fig. 1 are estimated to be small but they nevertheless add to the uncertainty in the value of the constant K_2, introduced in the expression for ν_{drift}, the rate of loss of electrons due to drift.

REFERENCES

Brown, S. C. 1959. Basic data of plasma physics (co-published by Technology Press of Massachusetts Institute of Technology and John Wiley & Sons, Inc., New York).

Gibson, G., Jordan, W. C., and Lauer, E. J. 1960. Phys. Rev. Letters, **4**, 217.

Harrison, M. A. and Geballe, R. 1953. Phys. Rev. **91**, 1.

Reynolds, P. and Skarsgard, H. M. 1958. CERN 58–19.

——— 1959. J. Nuclear Energy, Part C, **1**, 36.

Skarsgard, H. M. 1959. University of Saskatchewan Physics Dept. Internal Report P.R. 1-1959.

Spitzer, L., Jr. 1956. Physics of fully ionized gases (Interscience Publishers Inc., New York).

THE PRESSURE PULSE PRODUCED BY A LARGE EXPLOSION IN THE ATMOSPHERE[1]

V. H. WESTON

ABSTRACT

The pressure pulse produced by a large explosion in the atmosphere is investigated. The explosion is represented in terms of the excess pressure and normal velocity on a closed surface, outside of which the hydrodynamical equations are linearized. The pulse is represented in terms of a Fourier transform of the associated harmonic frequency problem, for which a ring-source Green's function is obtained in terms of an expansion of the discrete modes. It is shown that the excess pressure may be represented in terms of an integral (containing the Green's function) over the surface surrounding the source. The gravity wave portion of the pressure pulse at the ground is computed for various ranges from the source, which is located at various altitudes, and for three models of the atmosphere. In calculating the head of the pulse a new asymptotic technique is introduced which gives very good results for intermediate and long ranges.

1. INTRODUCTION

There have been many recent efforts devoted to the study of "free" waves in the atmosphere and the pressure pulse produced by large explosions such as the Krakatoa volcanic eruption of 1883, the great Siberian meteorite of 20 June, 1908, and, recently, nuclear explosions. As an example of the latter, the Japanese have recorded such atmospheric waves from nuclear explosions (Yamamoto 1957). These waves travel great distances around the earth.

The pressure pulse produced by such explosions can be decomposed into two portions, a low-frequency "gravity" wave train, plus high-frequency "acoustic" wave trains. Theoretical analysis has been mainly devoted to the "gravity" wave portion of the pressure pulse produced by large explosions on the ground for simple models of the atmosphere (Pekeris 1939, 1948; Scorer 1950).

Hunt *et al.* (1960) have calculated both the gravity wave and acoustic wave portions of the pressure pulse produced by explosions on the ground.

Here the interest will be mainly concerned with the head of the gravity wave portion of the pulse produced by explosions not only on the ground but at various heights in the atmosphere. The results presented here are discussed in more detail by Weston (1960).

Initial Nomenclature

(1) Spherical polar co-ordinates (r, θ, ϕ)
(2) Radius of earth $r = a$
(3) T = absolute temperature
R = gas constant
γ = ratio of specific heats

[1]Manuscript received February 10, 1961.
Contribution from the Radiation Laboratory, University of Michigan, Ann Arbor, Michigan. The research reported in this paper was supported by Contract AF 19(604)-5470 with the Geophysics Research Directorate, Air Force Cambridge Research Laboratories, Air Research and Development Command, United States Air Force, Bedford, Massachusetts.

p = gas pressure
ρ = gas density
$c_0^2 = \gamma RT_0 = \gamma p_0/\rho_0$
$\mathbf{u}$ = velocity = (u_r, u_θ, u_ϕ)

(4) Unperturbed state denoted by subscripts zero, i.e., T_0, ρ_0, etc.

(5) Perturbed state is represented in terms of the unperturbed state plus a perturbation term (which has no subscript) i.e., p_0+p, $T_0+T, \ldots$

2. CHARACTERIZATION OF THE SOURCE OF THE PRESSURE PULSE

A large explosion in the atmosphere is usually detected at large distances by changes in pressure. Hence the excess pressure $p(\mathbf{r}, t)$ will be obtained. At a sufficient distance from the source of the explosion it is known that the excess variables, pressure, density, and temperature are small in comparison with the corresponding unperturbed variables for the atmosphere.

Let the source of the explosion be at the point $(R_0, 0, 0)$ where $R_0 > a$ (the radius of the earth). It will be assumed that the explosive effects are independent of the azimuth angle ϕ. The source can be enclosed by a surface of revolution S_0 with axis of revolution $\theta = 0$ (i.e. the z axis), such that outside this surface, the excess pressure, density, etc. are small in comparison with their respective unperturbed values. The surface S_0 may be a small sphere with center $(R_0, 0, 0)$. However, its actual form at present will not be specified.

In the region outside S_0 and outside the earth ($r = a$), it will be assumed that the excess variables are small in comparison with their respective unperturbed values. In addition, viscosity and the effects of winds will be neglected.

The source of the pressure pulse will be characterized by boundary conditions on the surface S_0. To specify the problem uniquely $p(r, t)$ and $\mathbf{n}\cdot\mathbf{u}$ for $\mathbf{r}$ on S_0 must be specified. $\mathbf{n}$ represents the unit outward normal to S_0.

3. THE EQUATIONS OF MOTION

To begin with, note that the explosive effects are independent of ϕ, hence all the variables will be independent of ϕ.

From Ramsey (1949), we have the equations of motion

$$(1) \qquad \frac{\partial \mathbf{u}}{\partial t} + (\mathbf{u}\cdot\nabla)\mathbf{u} + \mathbf{K} = -\frac{1}{(\rho+\rho_0)}\nabla(p+p_0) + (-g, 0, 0)$$

where

$$\mathbf{K} = \frac{1}{r}\left(-[u_\theta^2+u_\phi^2], [u_r u_\theta - u_\phi^2 \cot\theta], [u_r u_\phi + u_\theta u_\phi \cot\theta]\right),$$

the equation of continuity

$$(2) \qquad \frac{\partial}{\partial t}(\rho+\rho_0) + (\mathbf{u}\cdot\nabla)(\rho+\rho_0) + (\rho+\rho_0)\nabla\cdot\mathbf{u} = 0,$$

the adiabatic energy equation

$$\frac{\partial}{\partial t}(p+p_0)+(\mathbf{u}\cdot\nabla)(p+p_0) = c^2\left[\frac{\partial}{\partial t}(\rho+\rho_0)+(\mathbf{u}\cdot\nabla)(\rho+\rho_0)\right], \tag{3}$$

and the equation of state

$$(p+p_0) = (\rho+\rho_0)R(T+T_0).$$

If use is made of the hydrostatic equations for the unperturbed atmosphere and second-order pressure and density terms neglected, equation (1) becomes

$$\frac{\partial \mathbf{u}}{\partial t}+(\mathbf{u}\cdot\nabla)\mathbf{u}+\mathbf{K} \simeq -\frac{1}{\rho_0}\nabla p+\left(-\frac{g\rho}{\rho_0}, 0, 0\right). \tag{4}$$

Also equations (2) and (3) become

$$\frac{\partial \rho}{\partial t}+u_r\rho_0'+\rho_0\nabla\cdot\mathbf{u} = 0 \tag{5}$$

$$\frac{\partial p}{\partial t}+u_r p_0' = c^2\left[\frac{\partial \rho}{\partial t}+u_r\rho_0'\right] \tag{6}$$

where the prime indicates differentiation with respect to r.

4. THE UNPERTURBED VARIABLES

Before proceeding further, several relations are needed involving the unperturbed variables ρ_0, p_0, and T_0. From the hydrostatic equation

$$p_0' = -g\rho_0$$

and equation of state

$$p_0 = R\rho_0 T_0$$

we obtain, on integration, the following

$$p_0(r) = p_0(a)\exp\left[-\frac{1}{R}\int_a^r\left(\frac{g}{T_0}\right)dr\right], \tag{7}$$

$$\rho_0(r) = \frac{p_0(a)}{RT_0(r)}\exp\left[-\frac{1}{R}\int_a^r\left(\frac{g}{T_0}\right)dr\right]. \tag{8}$$

The following relation can be obtained from (8)

$$\frac{\rho_0'}{\rho_0} = -\frac{T_0'}{T_0}-\frac{\gamma g}{c_0^2}. \tag{9}$$

5. REDUCTION OF THE EQUATIONS FOR HARMONIC TIME DEPENDENCE

The pulse problem is reduced to that of a harmonic time-dependent problem by representing the excess pressure pulse in terms of a Fourier transform. For the present the harmonic time-dependent problem will be considered.

For harmonic time dependence of the form $e^{-i\omega t}$ equations (4), (5), and (6) become, on neglecting second-order terms in $\mathbf{u}$,

$$-i\omega\mathbf{u}+\frac{1}{\rho_0}\nabla p+\left(\frac{g\rho}{\rho_0}, 0, 0\right) = 0, \tag{10}$$

$$-i\omega\rho+u_r\rho_0'+\rho_0\nabla\cdot\mathbf{u}=0, \tag{11}$$

$$-i\omega p+u_r p_0'=c_0^2[-i\omega\rho+u_r\rho_0']. \tag{12}$$

If the hydrostatic equation is used, equations (12) and (11) become

$$-i\omega[p-c_0^2\rho]=u_r[c_0^2\rho_0'+g\rho_0] \tag{13}$$

$$c_0^2\nabla\cdot\mathbf{u}-\frac{i\omega}{\rho_0}p-gu_r=0. \tag{14}$$

Using equation (13), eliminate ρ from equation (10) to give

$$-i\omega\mathbf{u}\rho_0^{1/2}=-\mathbf{L}(\rho_0^{-1/2}p)-\hat{\imath}_r ph^{-1}\rho_0^{-1/2}A \tag{15}$$

where

$$h=1+\frac{g}{\omega^2}\left(\frac{\rho_0'}{\rho_0}+\frac{g}{c_0^2}\right), \tag{16}$$

$$A=\left[\frac{g}{c_0^2}+\frac{1}{2}\frac{\rho_0'}{\rho_0}\right], \tag{17}$$

and the operator $\mathbf{L}$ has components

$$\mathbf{L}=\left(\frac{1}{h}\frac{\partial}{\partial r},\frac{1}{r}\frac{\partial}{\partial\theta},\frac{1}{r\sin\theta}\frac{\partial}{\partial\theta}\right). \tag{18}$$

The velocity vector $\mathbf{u}$ may now be eliminated from (14) and (15) giving

$$\nabla\cdot\mathbf{L}(\rho_0^{-1/2}p)+\frac{q(r)}{r^2}(\rho_0^{-1/2}p)=0 \tag{19}$$

with

$$q(r)=\left[\frac{\omega^2r^2}{c_0^2}+\frac{r^2}{h}\left(-A^2+A'-A\frac{h'}{h}+\frac{2}{r}A\right)\right]. \tag{20}$$

Let L_r and L_θ represent the differential operators

$$L_r\psi=\frac{\partial}{\partial r}\left(\frac{r^2}{h}\frac{\partial\psi}{\partial r}\right)+\psi q(r) \tag{21}$$

$$L_\theta\psi=\frac{1}{\sin\theta}\frac{\partial}{\partial\theta}\left(\sin\theta\frac{\partial\psi}{\partial\theta}\right). \tag{22}$$

Then (19) becomes

$$(L_r+L_\theta)(\rho_0^{-1/2}p)=0, \tag{23}$$

which is separable.

The required solution of (23) must satisfy the boundary condition that the vertical velocity vanish at $r=a$, and that the total kinetic energy be finite.

Let $\phi(r)$ be the r component of $\rho_0^{-1/2}(r)\,p(r)$, and $\mu^2-\frac{1}{4}$ the separation constant. The separated equation involving $\phi(r)$ is then

$$L_r\phi+(\tfrac{1}{4}-\mu^2)\phi=0$$

or more explicitly,

$$\frac{d}{dr}\left(\frac{r^2}{h}\frac{d\phi}{dr}\right)+\phi\left\{r^2\left(\frac{\omega^2}{c_0^2}-\frac{A^2}{h}\right)+\frac{d}{dr}\left(\frac{Ar^2}{h}\right)+\frac{1}{4}-\mu^2\right\}=0. \tag{24}$$

The next problem is to find the particular modes resulting from the separation of (23), subject to the appropriate boundary conditions, and then expand $\rho_0^{-1/2}p(r,\theta)$ in terms of these separated solutions.

6. FREE-WAVE MODES

In discussing the various modes (particular solutions of equation (24)), the following restrictions will be placed upon the models of the atmosphere that will be considered. First, it will be assumed that above some altitude, the temperature is isothermal. Secondly, since the basic problem under consideration is the investigation of the form of the pressure pulse in the lower atmosphere produced by a source which is at not too high an altitude (say less than 80 kilometers) the flat earth approximation will be made, whereby in (24) the terms r^2 will be set equal to a^2, giving

$$\frac{d}{dr}\left(\frac{1}{h}\frac{d\phi}{dr}\right)+\phi\left\{\frac{\omega^2}{c_0^2}-\frac{A^2}{h}+\frac{d}{dr}\left(\frac{A}{h}\right)-\omega^2\lambda^2\right\}=0 \tag{25}$$

where

$$\mu^2-\tfrac{1}{4}=\omega^2\lambda^2a^2. \tag{26}$$

Both terms μ and λ will be used later in the remaining analysis depending on which is the more convenient. Of the two, λ, being the inverse phase velocity of the wave, has the most physical significance.

As was indicated above, the appropriate solution of (23) must be such that the total kinetic energy be finite. For the flat earth approximation, this reduces to the condition that $\rho_0^{-1/2}(r)\,p(r,\theta)$ be squared integrable over the range $a\leqslant r\leqslant\infty$.

The required boundary condition at $r=a$ is that the vertical velocity must vanish. This reduces to the condition that

$$\phi'+A\phi=0. \tag{27}$$

The problem represented by equation (25) and (27) is self-adjoint, but because of the infinite upper limit of the independent variable, it is the singular case. If we define the constant Λ by

$$\begin{aligned}\Lambda&=-A_s^2/h_s-\omega^2\lambda^2+\omega^2/c_s^2 && \text{for } h_s>0\\ \Lambda&=A_s^2/(\omega^2h_s)+\lambda^2-1/c_s^2 && \text{for } h_s<0\end{aligned} \tag{28}$$

where the subscript s refers to the values in the upper isothermal layer, it can be shown (Weston, to be published) that for high frequencies such that $h>0$, and low frequencies such that $h<0$, for all r in the range $a\leqslant r\leqslant\infty$, there exist a discrete spectrum $\Lambda_i<0$, which is bounded below, and a continuous spectrum $\Lambda>0$. The modes corresponding to the discrete spectrum are such that they attenuate exponentially in the upper isothermal layer, whereas the modes of the continuous spectrum are oscillatory there.

From Titchmarsh (1946) the excess pressure can be represented in terms of a summation over the discrete set of modes plus an integral over the continuous set. However, in the problem on hand, that of propagation of a pressure pulse around the earth, the discrete modes will play the dominant role. Henceforth the effect of the continuous spectrum will be ignored, and only the contribution of the discrete set of modes to the excess pressure will be considered. In addition it will be assumed that the expansion holds in the frequency domain wherein at some r, h vanishes.

For expediency, $\phi_j(r)$ will be defined as the particular discrete mode of equation (25), corresponding to the eigenvalue Λ_j. To each value Λ_j, there correspond two values λ_j, namely $\pm|\lambda_j|$. However, the positive value will always be taken. The negative value corresponds to the same mode, but represents propagation in the opposite direction. In addition the same value of λ_j holds for both positive and negative value of ω.

7. THE GREEN'S FUNCTION

Instead of working directly with the excess pressure, we shall consider first a ring-source Green's function, defined to be a solution of

$$\nabla \cdot \mathbf{L}G + \frac{q(r)}{r^2} G = \frac{\delta(r-r_0)\delta(\theta-\theta_0)}{2\pi \sin\theta\, r^2} \tag{29}$$

such that at $r = a$

$$\frac{\partial G}{\partial r} + AG = 0 \tag{30}$$

where δ is the Dirac delta function.

Making the flat earth approximation, equation (29) becomes

$$\frac{d}{dr}\left(\frac{1}{h}\frac{d}{dr}G\right) + \frac{1}{a^2 \sin\theta}\frac{\partial}{\partial\theta}\sin\theta\frac{\partial G}{\partial\theta} + G\left\{\frac{\omega^2}{c_0^2} - \frac{A^2}{h} + \frac{d}{dr}\left(\frac{A}{h}\right)\right\} = \frac{\delta(r-r_0)\delta(\theta-\theta_0)}{2\pi \sin\theta\, a^2}. \tag{31}$$

Since we require that G be squared integrable with respect to r we can expand G in the form

$$G(\mathbf{r}, \mathbf{r}_0) = \sum_j \frac{\phi_j(r)\phi_j(r_0)X_j(\theta, \theta_0)}{\int_a^\infty \phi_j^2(r)dr} \tag{32}$$

where the continuous spectrum is neglected. The denominator can be expressed explicitly in the form

$$\int_a^\infty \phi_j^2(r)dr = \frac{-\phi(a, \lambda_j)}{2\omega^2\lambda_j}\left\{\frac{\partial}{\partial\lambda}\left[\frac{A\phi(\lambda)+\phi'(\lambda)}{h}\right]\right\}_{\substack{\lambda=\lambda_j \\ r=a}}. \tag{33}$$

Setting expression (32) in equation (31), and using equation (25) together with the orthogonality property of ϕ_j we obtain

$$\frac{1}{\sin\theta}\frac{\partial}{\partial\theta}\left(\sin\theta\frac{\partial}{\partial\theta}X_j\right)+\omega^2a^2\lambda_j^2X_j=\frac{\delta(\theta-\theta_0)}{2\pi\sin\theta}. \tag{34}$$

By usual techniques the solution is found

$$X_j(\theta,\theta_0)=-\frac{1}{4\cos\pi\mu_j}\begin{cases}P_{-1/2+\mu_j}(\cos\theta)P_{-1/2+\mu_j}(-\cos\theta_0) & 0\leqslant\theta\leqslant\theta_0\\ P_{-1/2+\mu_j}(\cos\theta_0)P_{-1/2+\mu_j}(-\cos\theta) & \theta_0\leqslant\theta\leqslant\pi\end{cases} \tag{35}$$

with $\mu_j=(\omega^2a^2\lambda_j^2+\frac{1}{4})^{1/2}$ and $P_n(\cos\theta)$ is the Legendre function of order n.

A note of caution is due here. There may exist a set of values of ω for which one or more μ_j is equal to half an odd integer, in which case the denominator of (35) vanishes. For present we will restrict ourselves to the values of ω not contained in this set. This problem will be circumvented later.

Using the Green's function we may now express the excess pressure at a point (r,θ) in terms of an integral representing the source. Multiply equations (19) and (29) by $G(\mathbf{r},\mathbf{r}_0)$ and $\rho_0^{-1/2}p(r)$ respectively, subtract the two resulting equations, and integrate over all space outside the earth's surface and the surface S_0 surrounding the source. Using the divergence theorem, the volume integral may be reduced to a surface integral, the result being

$$\int_S\mathbf{n}\cdot\{G\mathbf{L}_0(\rho_0^{-1/2}p)-\rho_0^{-1/2}p\mathbf{L}_0G\}\,dS_0=\rho_0^{-1/2}(r)p(\mathbf{r}). \tag{36}$$

The surface S comprises of S_0, $r=a$, and the limiting surface $r=\infty$. Because both $\rho_0^{-1/2}p$ and G satisfy the same boundary on $r=a$, the surface integral over $r=a$ vanishes. Since both G and $\rho_0^{-1/2}p$ are squared integrable for the flat earth approximation, the integral over $r=\infty$ vanishes. Thus the surface integral in (36) reduces to an integral over S_0.

Upon applying equation (15), the excess pressure has the form

$$\rho_0^{-1/2}(r)p(\mathbf{r})=i\omega\int_{S_0}G\rho_0^{1/2}(r_0)\mathbf{n}\cdot\mathbf{u}(r_0)\,dS-\int_{S_0}\rho_0^{-1/2}(r_0)p(\mathbf{r}_0)\left\{\left(\frac{A}{h}\right)_{r_0}G\mathbf{n}\cdot\hat{\mathbf{r}}_0+\mathbf{n}\cdot\mathbf{L}_0G\right\}dS \tag{37}$$

where $\mathbf{n}$ is the unit outward normal to the surface S_0. The variables of integration are denoted by the subscript zero. The vector $\mathbf{L}_0$ is the vector $\mathbf{L}$ with the variables r,θ replaced by r_0 and θ_0, and $\mathbf{r}_0$ is the unit vector in the direction of increasing r_0.

Using the representation of $G(\mathbf{r},\mathbf{r}_0)$ given by (32), formally rewrite it in the form

$$G(\mathbf{r},\mathbf{r}_0)=\sum_j\frac{f_j(\mathbf{r},\mathbf{r}_0)}{2\cos\pi\mu_j} \tag{38}$$

and then express $p(\mathbf{r})$ by the following

$$\rho^{-1/2}(r)p(\mathbf{r})=\sum_j\frac{I_j}{2\cos\pi\mu_j} \tag{39}$$

where I_j is the equivalent of the right-hand side of (37) with G replaced by $f_j(\mathbf{r}, \mathbf{r}_0)$. These relations will simplify further analysis.

8. THE EXCESS PRESSURE PULSE

With the associated harmonic time-dependent problem established, the corresponding pulse problem can now be treated. The explosion is characterized by known values of $p(\mathbf{r}, t)$ and $\mathbf{n}\cdot\mathbf{u}\ (\mathbf{r}, t)$ on the surface S_0, namely

$$p(\mathbf{r}, t) = 0 \qquad t < 0 \tag{40}$$
$$= m(\mathbf{r}, t) \qquad t > 0$$

$$\mathbf{n}\cdot\mathbf{u}(\mathbf{r}, t) = 0 \qquad t < 0 \tag{41}$$
$$= n(\mathbf{r}, t) \qquad t > 0$$

for $\mathbf{r}$ on S_0, with $m(\mathbf{r}, t)$ and $n(\mathbf{r}, t)$ being known functions. Let the Fourier transforms of m and n be $M(\mathbf{r}, \omega)$ and $N(\mathbf{r}, \omega)$ respectively.

Then the excess pressure pulse generated by initial conditions (40) and (41) is given by

$$p(\mathbf{r}, t) = \frac{1}{2\pi}\rho^{1/2}(r)\int_{-\infty}^{\infty} e^{-i\omega t}\sum_j \frac{I_j}{2\cos\pi\mu_j}\,d\omega \tag{42}$$

where I_j are given by the relation

$$I_j = i\omega\int_{S_0} f_j(\mathbf{r}, \mathbf{r}_0)\rho_0^{1/2}(r_0)N(\mathbf{r}_0, \omega)\,dS \tag{43}$$
$$-\int_{S_0}\rho_0^{-1/2}(r_0)M(\mathbf{r}_0, \omega)\left\{\left(\frac{A}{h}\right)_{r_0}\mathbf{n}\cdot\hat{\mathbf{r}}_0+\mathbf{n}\cdot\mathbf{L}_0\right\}f_j\,dS.$$

However, as was pointed out earlier, there may exist a set of ω such that there exists one or more μ_j for which $\cos\pi\mu_j$ vanishes. Hence the line integral in (42) must be deformed to pass around these values of ω.

Perform the following decomposition

$$\frac{1}{2\cos\pi\mu_j} = \sum_{m=0}^{n-1}(-1)^m\exp i\{\pi(2m+1)\mu_j\}+\frac{(-1)^n\exp(i2\pi n\mu_j)}{2\cos\pi\mu_j} \tag{44}$$

and set

$$p(\mathbf{r}, t) = \sum_{m=0}^{n-1} p^{(m)}(\mathbf{r}, t)+P^{(n)}(\mathbf{r}, t) \tag{45}$$

where $p^{(m)}(\mathbf{r}, t)$ and $P^{(n)}(\mathbf{r}, t)$ are given by the right-hand side of (42) with the denominator in the integrand replaced by

$$(-1)^m\exp i\{\pi(2m+1)\mu_j\} \quad \text{and} \quad (-1)^n\exp(i2\pi n\mu_j)/(2\cos\pi\mu_j)$$

respectively. In the exponents involving $\mu_j = (\omega^2a^2\lambda_j^2+\tfrac{1}{4})^{1/2}$, we will make the approximation

$$\mu_j \sim \omega a\lambda_j, \tag{46}$$

which is only inaccurate for an extremely small and negligible range of ω, roughly given by $\omega < 10^{-4}$ sec. Using (46), the only difference between the integral expressions for $p(\mathbf{r}, t)$ and $P^{(n)}(\mathbf{r}, t)$ is that the former contains $\exp(-i\omega t)$ and the latter $(-1)^n \exp -i\omega[t-2\pi a\lambda_j n]$. Thus it immediately follows that

$$P^{(n)}(\mathbf{r}, t) \simeq (-1)^n p(\mathbf{r}, t-2\pi n a\lambda_j). \tag{47}$$

Since λ_j is the inverse phase velocity, the time interval represented by $2\pi n a\lambda_j$ is the time taken for the mode to encircle the earth n times. Hence $P^{(n)}(\mathbf{r}, t)$ represents the portion of the pulse that has encircled the earth at least n times. Finally it may be shown that $p^{(m)}(\mathbf{r}, t)$ represents the portion of the pulse that has encircled the earth m times.

Henceforth we will be concerned with the portion of the pulse that has arrived directly without encircling the earth. This portion is given by

$$p^{(0)}(\mathbf{r}, t) = \frac{\rho_0^{1/2}(r)}{2\pi} \int_{-\infty}^{\infty} \sum_j I_j e^{-i\omega[t-\pi a\lambda_j]} d\omega. \tag{48}$$

This splitting up of the pressure wave into the above components removes the problem of poles on the path of integration.

9. THE PRESSURE PULSE PRODUCED BY A SIMPLE SOURCE

The relation given by (48) together with (43), for the directly received portion of the pressure pulse is for a general explosion. Unfortunately, analytical solutions are not available for large explosions. An analytic solution has been found for an intense spherically symmetric explosion (Taylor 1954) but it holds down to only overpressure of about 20 atmospheres. Hence for good source models, values of the excess pressure and normal velocity must be obtained from observational data. For numerical evaluation, the problem will be simplified by letting the surface Σ be a small sphere with center $(R_0, 0)$. Then the limit is taken on letting the radius shrink to zero. In addition, the time dependence taken will be such that the source is an instantaneous velocity source. Taking the limit, one obtains (Weston 1960)

$$I_j = i\omega f_j(\mathbf{r}; R_0, 0) V \rho_0^{1/2}(R_0) \tag{49}$$

where V is the total volume of gas introduced.

The case where the observer is on the ground will be considered, namely $\mathbf{r} = \mathbf{a} = (a, \theta)$. Then from (32), (33), (35), and (38) one obtains

$$f_j(\mathbf{a}; R_0, 0) = \frac{\omega^2 \lambda_j \phi_j(R_0) P_{-1/2+\mu_j}(-\cos\theta)}{\left\{\dfrac{\partial}{\partial\lambda}\left[\dfrac{A\phi+\phi'}{h}\right]\right\}_{\substack{\lambda=\lambda_j \\ r=a}}} \tag{50}$$

and except for a very small negligible interval around $\omega = 0$, the following approximation may be made

$$P_{-1/2+\mu_j}(-\cos\theta) \sim (\tfrac{1}{2}\pi|\omega|a\lambda_j \sin\theta)^{-1/2} \cos\left\{|\omega|a\lambda_j(\pi-\theta) - \frac{\pi}{4}\right\} \tag{51}$$

for $0 < \theta < \pi$.

Of course when $\theta = \pi$ (i.e. the observer at the antipodes of the source) the left-hand side of (51) is unity.

Hence for the simple source model, the directly received pulse on the ground is given by

$$(52)\quad p^{(0)}(a,\theta,t) = -i\left(\frac{\rho_0(R_0)\rho_0(a)}{2\pi a \sin\theta}\right)^{1/2}\frac{V}{\pi}\int_{-\infty}^{\infty}\sum_j e^{-i\omega[t-\pi a\lambda_j]}\cos\left\{|\omega|a\lambda_j(\pi-\theta)-\frac{\pi}{4}\right\} \times \varepsilon\sqrt{\frac{\lambda_j}{|\omega|}}\,Q_j(\omega)\,d\omega$$

where for convenience

$$(53)\quad Q_j(\omega) = \frac{-\omega^2\phi_j(R_0)}{\left\{\frac{\partial}{\partial\lambda}\left[\frac{A\phi+\phi'}{h}\right]\right\}_{\substack{\lambda=\lambda_j \\ r=a}}}.$$

Since λ_j and $Q_j(\omega)$ are even functions of ω, the integral in (52) may be rewritten

$$(54)\quad i\int_0^{\infty}\sum_j \sqrt{\omega\lambda_j}\,Q_j(\omega)\left\{\cos\left[\omega(t-a\lambda_j\theta)+\frac{\pi}{4}\right] +\cos\left[\omega(t-a\lambda_j(2\pi-\theta))+\frac{3\pi}{4}\right]\right\}d\omega.$$

The first integral in (54) corresponds to the wave that has taken the shortest route, whereas the second integral in (54) corresponds to the wave that has travelled by way of the antipodal route.

10. EVALUATION OF THE GRAVITY WAVE PORTION OF THE PULSE

We will be concerned with the contribution to (52) of one particular mode, the low-frequency gravity wave mode. For particular models of the atmosphere there exist other modes which have a low-frequency cutoff (usually called acoustical modes). The observed pressure pulses produced by large explosions (Yamamoto 1957; Scorer 1950; Hunt *et al.* 1960) indicate the low-frequency gravity wave superimposed on which there may exist the high-frequency phenomena. For some models of the atmosphere (mainly those with the upper isothermal layer the coldest) the gravity wave mode has a high-frequency cutoff (Weston, to be published).

We shall consider the portion of the gravity wave that has taken the shortest route. (The antipodal wave is discussed in Weston (1960).) The excess pressure has the form

$$(55)\quad p(a,\theta,t) = \sqrt{\frac{\rho_0(R_0)\rho_0(a)}{2\pi a\sin\theta}}\,\frac{V}{\pi}\int_0^{\infty}\sqrt{\omega\lambda}\,Q(\omega)\cos\left[\omega(t-a\lambda\theta)+\frac{\pi}{4}\right]d\omega$$

where the subscript j is omitted, and it is understood that the values of λ, $Q(\omega)$ correspond to the gravity wave mode. If the gravity wave in question has a high-frequency cutoff, ω_c, then it will be understood that the integrand in (55) vanishes for $\omega > \omega_c$.

The integral in (55) is equal to the real part of

$$\int_0^\infty \sqrt{\omega\lambda}\, Q(\omega) \exp i\left[\omega(t-a\lambda\theta)+\frac{\pi}{4}\right] d\omega. \tag{56}$$

For large ranges ($a\theta$ sufficiently large) the above integral may be evaluated by the method of stationary phase.

If ω_0 is the value of ω for which

$$t-a\theta(\omega\lambda)' = 0 \tag{57}$$

where the prime indicates the derivative with respect to ω, then the stationary phase technique gives the asymptotic approximation to (56)

$$\sqrt{\frac{2\pi}{a\theta}}\, Q(\omega_0) \sqrt{\frac{\omega_0\lambda}{(\omega_0\lambda)''}}\pi \cos[\omega_0 t-\omega_0\lambda a\theta]. \tag{58}$$

Of course if there is an upper frequency cutoff, ω_c, this will hold provided that $\omega_0 < \omega_c$. In addition the stationary phase technique for (56) is not accurate unless $(\omega\lambda)'''/[(\omega\lambda)'']^{3/2} < \sqrt{a\theta}$ and $(\omega\lambda)^{iv}/[(\omega\lambda)'']^2 < a\theta$. It has been shown by Hunt *et al.* (1960) that this critique fails for most models of the atmosphere under consideration when the range $a\theta$ is of the order of 1000 km or less, and for some models of the atmosphere, even when the range is of the order of 3000 km.

For these cases it is best at present to perform numerical integration to evaluate (56) in the manner that is suggested by Hunt *et al.* (1960).

In addition, even at very large ranges, the stationary phase technique fails for the initial part of the received pressure pulse. We shall give here an asymptotic technique for calculating the initial part or head of the pulse for the gravity wave portion. This method will hold for models of the atmosphere where the gravity wave mode does not have a low-frequency cutoff, i.e., the wave exists at $\omega = 0$.

Define the following series

$$\lambda(\omega) = \sum_{n=0}^{\infty} \lambda_n \omega^{2n}, \tag{59}$$

$$(\lambda)^{1/2} Q(\omega) = \lambda_0^{1/2} Q(0) \sum_{n=0}^{\infty} d_n \omega^{2n} \tag{60}$$

where $d_0 = 1$. It can be shown that the above expansions are valid for a sufficiently large range of ω around $\omega = 0$, for the models of atmosphere under present consideration.

Define the time interval

$$\tau = t-a\theta\lambda_0. \tag{61}$$

By the stationary phase technique, the condition $\tau = 0$ or $t = a\theta\lambda_0$ would indicate the beginning of the pulse. However, for $|\tau|$ small, the stationary phase technique fails and we shall show that $\tau = 0$ does not represent the beginning of the pulse, but a point near the peak of the first compression.

The integral (56) may now be written in the form

$$(62)\qquad \lambda_0^{1/2}Q(0)\int_0^\infty \omega^{1/2}\cdot\sum_{n=0} d_n\omega^{2n}\cdot[1-ia\theta(\omega^5\lambda_2+\omega^7\lambda_3+\ldots)+\ldots]$$
$$\times\exp i\left[\omega\tau-\omega^3\lambda_1 a\theta+\frac{\pi}{4}\right]d\omega.$$

Making the substitution

$$(63)\qquad \omega = \sigma(\lambda_1 a\theta)^{-1/3}$$

$$(64)\qquad q = \tau(\lambda_1 a\theta)^{-1/3}$$

and defining the integral

$$(65)\qquad F_n(q) = \int_0^\infty \sigma^{-1/2+n}\, e^{i[\sigma q-\sigma^3]}\, d\sigma,$$

expression (64) has the asymptotic form

$$(66)\qquad \sqrt{\frac{\lambda_0}{\lambda_1 a\theta}}\,Q(0)\,e^{i\pi/4}\left\{F_1(q)+\frac{d_1}{(\lambda_1 a\theta)^{2/3}}F_3(q)+\frac{d_2}{(\lambda_1 a\theta)^{4/3}}F_5(q)+\ldots\right.$$
$$\left.-\frac{ia\theta}{(\lambda_1 a\theta)^{5/3}}\lambda_2 F_6(q)-\frac{ia\theta}{(\lambda_1 a\theta)^{7/3}}[\lambda_3+d_1\lambda_2]\,F_8(q)+\ldots\right\}.$$

It is shown (Weston 1960) that the $F_n(q)$ can be expressed in terms of products of Airy integrals. Thus expression (66) may be represented in terms of Airy integrals (which are tabulated by Miller (1946)). After much algebraic manipulation (Weston 1960), the real part of (66) has the following asymptotic form

$$(67)\qquad 2Q(0)\sqrt{\frac{\lambda_0\pi^3}{3\lambda_1 a\theta}}\,\{-A_i A_i' C_1+A_i^2 C_2-[(A_i')^2+y(A_i)^2]C_3\}$$

where $A_i(y)$ is the Airy integral, with A_i' being its derivative. The argument y is given by

$$(68)\qquad y = -\frac{\tau}{(12\lambda_1 a\theta)^{1/3}}.$$

The functions $C_i(\tau)$ have the forms

$$C_1(\tau) = 1+\frac{\tau}{(12\lambda_1 a\theta)}\left(4d_1-\frac{20\lambda_2}{3\lambda_1}\right)+\frac{8\tau^2}{(12\lambda_1 a\theta)^2}\left(2d_2-7\,\frac{[\lambda_3+d_1\lambda_2]}{\lambda_1}\right),$$

$$(69)\qquad C_2(\tau) = \frac{1}{(12\lambda_1 a\theta)^{2/3}}\left(d_1-\frac{7\lambda_2}{6\lambda_1}\right)+\frac{4\tau}{(12\lambda_1 a\theta)^{5/3}}\left(d_2-3\,\frac{[\lambda_3+d_1\lambda_2]}{\lambda_1}\right),$$

$$C_3(\tau) = \frac{10}{(12\lambda_1 a\theta)^{4/3}}\left(d_2-\frac{11[\lambda_3+d_1\lambda_2]}{6\lambda_1}\right)+\frac{\tau^2}{(12\lambda_1 a\theta)^{4/3}}\frac{4\lambda_2}{3\lambda_1}$$
$$+\frac{\tau^3}{(12\lambda_1 a\theta)^{7/3}}\frac{16[\lambda_3+d_1\lambda_2]}{3\lambda_1}.$$

11. NUMERICAL RESULTS

With the theory set up in the previous sections, one can now compute the pulse forms. The first problem is to evaluate the radial eigenfunctions and eigenvalues corresponding to the gravity wave. For some simple models of the atmosphere, good analytical approximations to the eigenfunctions may be made using an iteration technique. This is discussed by Weston (1960). However, for the models of atmosphere that will be considered here, it is best to use numerical techniques.

Instead of solving for $\phi(r)$ we will investigate the function $\psi(r)$ given by

$$\psi(r) = \phi(r) \exp \int_a^r A \, dx. \tag{70}$$

Using equations (25) and (70), the resulting equation obtained for ψ is

$$\psi'' + \psi' \left[-2A - \frac{h'}{h} \right] + h\omega^2 \left[\frac{1}{c_0^2} - \lambda^2 \right] \psi = 0. \tag{71}$$

The boundary condition at $r = a$ reduces to $\psi' = 0$.

In the upper isothermal layer, the required eigenfunction ψ will have the form

$$\psi(r) \sim \exp[A_s - \beta]r \tag{72}$$

where

$$\beta = \left[\left(\frac{2-\gamma}{2} \right)^2 \frac{g^2}{c_s^4} - \left(\frac{1}{c_s^2} - \lambda^2 \right) \left(\omega^2 + (1-\gamma) \frac{g^2}{c_s^2} \right) \right]^{1/2} \tag{73}$$

and the subscript s refers to the values in the upper isothermal atmosphere where in particular

$$A_s = \left(\frac{2-\gamma}{2} \right) \frac{g}{c_s^2}.$$

The models of atmosphere that will be considered below will be such that the values of temperature are given at a set of altitudes (or data points), up to a certain height l, above which the temperature will be taken constant. For simplicity in numerical integration the temperature between two adjacent sets of data points will be taken linear, the gradient of temperature determined by the values at the end points. Hence for numerical integration, the model is approximated by a set of straight elements, the points of discontinuity of the gradient of temperature being at the data points.

In transversing these points of discontinuity of T_0' in the numerical integration of (71), use is made of the conditions that both ψ and ψ'/h be continuous. These results are obtainable from the condition that the pressure and vertical velocity be continuous.

At the lower boundary of the upper isothermal layer (namely at $r = a+l$), equation (72) and the upper continuity conditions are utilized to obtain

$$\psi' = \left[-\beta+\left(\frac{2-\gamma}{2}\right)\frac{g}{c_s^2}\right]\frac{h_t}{h_s}$$

where ψ is normalized so that at $r = a+l$, ψ is unity, and h_t and h_s are the values of h below and above the discontinuity at $r = a+l$.

Using the results of Weston (to be published), upper and lower bounds may be placed on the required values of λ. Hence initially λ can be guessed quite accurately.

Two models of the atmosphere are given in the following tables, where the altitudes are given in geopotential kilometers and the temperature in degrees centigrade.

Atmosphere I		Atmosphere II	
Altitude	Temperature	Altitude	Temperature
Surface	29	Surface	17
1.5	18	1.5	8
3.1	10	3.0	− 3
5.9	− 5	5.6	−19
9.7	−31	9.2	−46
12.4	−53	11.9	−49
14.2	−67	13.8	−47
16.6	−81	16.4	−47
20	−66	20	−48
25	−65	25	−46
30	−45	30	−42
35	−34	35	−34
40	−20	40	−18
45	− 5	45	− 2
50	7	50	4

For the sake of comparison we will include Scorer's model (1950), such that the lower non-isothermal atmosphere has a constant temperature gradient with temperatures 286.91° K and 229.53° K at the surface and at a height of 9.6137 km, respectively.

The calculated inverse phase velocities for the gravity wave are given in Table I. Scorer's model of the atmosphere has a high-frequency cutoff at around 5000 $\omega^2 = 15.9$. The gravity wave for the other two models exists for much higher frequencies than shown in the table.

The pressure pulse forms are computed for Scorer's model of the atmosphere for explosions both on the ground and at a height of 9.6137 km, and plotted in Fig. 1. The pressure pulses were computed using the stationary phase technique for $\tau \geqslant 160$ sec, and the asymptotic expansion involving Airy integrals for $\tau \leqslant 160$ sec. There is good matching of the results obtained by both methods in the vicinity of $\tau = 160$ sec. The complete pulse forms are not given, but there is a cutoff at τ about $10\frac{1}{4}$ minutes and 17 minutes for the ranges 3600 km and 6000 km respectively. The pulse forms calculated here do differ appreciably from those calculated by Scorer. As pointed out by Hunt *et al.* (1960), Scorer's pulse forms are in error. The first compression as computed by the asymptotic expansion (67) is the most realistic yet calculated. It agrees remarkably well with observed results.

TABLE I

	Inverse phase velocities λ (km^{-1} sec)		
5000 ω^2	Atmosphere I	Atmosphere II	Scorer's model
0	3.15283	3.16379	3.18947
1	3.15819	3.16773	3.19148
2	3.16277	3.17072	3.19355
3	3.16695	3.17319	3.19570
4	3.17091	3.17534	3.19793
5	3.17472	3.17728	3.20025
6	3.17844	3.17907	3.20266
7	3.18209	3.18074	3.20517
8	3.18569	3.18233	3.20778
9	3.18923	3.18384	3.21052
10	3.19274	3.18530	3.21338
11	3.19620	3.18672	3.21638
12	3.19962	3.18809	3.21953
13	3.20301	3.18943	3.22286
14	3.20635	3.19073	3.22637
15	3.20965	3.19201	3.23006
16	3.21290	3.19327	—
17	3.21611	3.19450	—
18	3.21928	3.19571	—
19	3.22239	3.19690	—
20	3.22545	3.19807	—
21	3.22846	3.19922	—
22	3.23142	3.20035	—
23	3.23433	3.20147	—
24	3.23718	3.20257	—
25	3.23998	3.20365	—

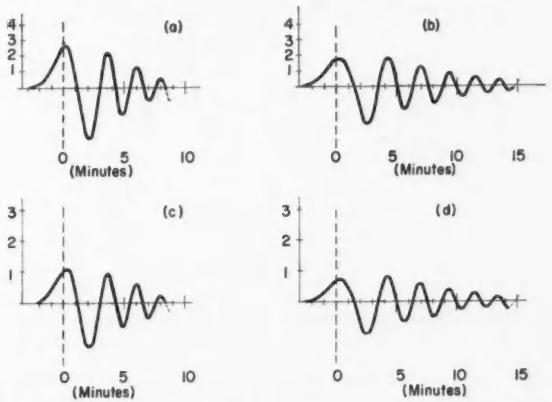

FIG. 1. The pressure pulse at the ground at a distance of 3600 km (*a*) and (*c*), and 6000 km (*b*) and (*d*) for Scorer's atmosphere, for an explosion on the ground (*a*) and (*b*), and at a height of 9.6137 km (*c*) and (*d*). One unit of amplitude corresponds to 0.614 μbar per 1 km^3 of gas released.

In addition, pulse forms for atmospheres I and II are computed and given in Figs. 2 and 3, for a range of 7000 miles. The tail of the pulse extends beyond the section calculated for a very long period. There is much less dispersion for atmosphere II than atmosphere I.

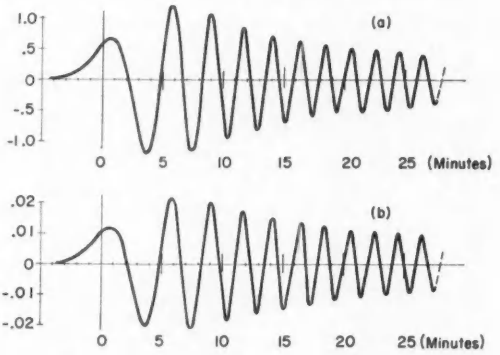

FIG. 2. The head of the pressure pulse at ground level at a distance of 7000 km from an explosion on the ground (*a*), and at a height of 39 km (*b*), for atmosphere model I. One unit of amplitude corresponds to 1 μbar per 1 km^3 of gas released. (The tail of the pulse which extends for a very long time interval beyond the broken lines is not given.)

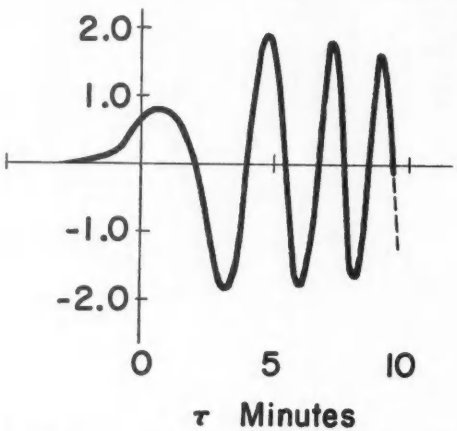

FIG. 3. The head of the pressure pulse at ground level at a distance of 7000 km from an explosion on the ground for atmosphere model II. One unit of amplitude corresponds to 1 μbar per 1 km^3 of gas released.

12. COMMENTS

The asymptotic methods given here give good results for the gravity wave portion of the pulse. To agree completely with some of the observed data, the higher modes must be included, although in some instances they do not appear.

Previous authors have been limited to the investigation of simple point sources at ground level, where their derivation of the pressure pulse forms are based more on a restricted intuitive rather than a general rigorous approach.

Although the calculations here have been confined to a simple source model, the effects of realistic source models in the atmosphere may be studied by

using equation (48) together with (43). In addition, the technique used here to obtain the pressure pulse form represented by equations (48) and (43), is not limited to models of the atmosphere for which the upper atmosphere is isothermal. Winds play an important role in determining the phase velocity of the modes.

The effects of winds on the gravity wave are discussed by Weston and van Hulsteyn (to be published).

More realistic models of the upper atmosphere are being investigated at the present time.

ACKNOWLEDGMENT

The author wishes to thank L. Evans and D. Hodgins for the computational work that they performed.

REFERENCES

HUNT, J. N., PALMER, R., and PENNEY, SIR WILLIAM. 1960. Phil. Trans. Roy. Soc. A, **252** (1011), 275.
MILLER, J. C. P. 1946. The Airy integral, British Association for the Advancement of Science, Math. Tables, B (Cambridge University Press, Cambridge).
PEKERIS, C. L. 1939. Proc. Roy. Soc. A, **171**, 434.
——— 1948. Phys. Rev. **73** (2), 145.
RAMSEY, A. S. 1949. A treatise on hydromechanics, Part II (C. Bell and Son).
SCORER, R. C. 1950. Proc. Roy. Soc. A, **201**, 137.
TAYLOR, J. L. 1954. Phil. Mag. **46**, 317.
TITCHMARSH, E. C. 1946. Eigenfunction expansion, Part I (Oxford University Press).
WESTON, V. H. 1960. The University of Michigan Radiation Laboratory Report 2886-1-T.
——— To be published.
WESTON, V. H. and VAN HULSTEYN, D. B. To be published.
YAMAMOTO, R. 1957. J. Meteorol. Soc. Japan, II, **35**, 5.

GAMMA-ACTIVE FALL-OUT IN ONTARIO 1958–60[1]

K. G. McNeill, O. A. D. Trojan, and D. J. Dawson

ABSTRACT

Measurements have been made of the Cs^{137} content of man and of milk and of the Zr^{95} and Cs^{137} activity of air-borne dust. They show that the Cs^{137} content of man went through a maximum of 67 $\mu\mu$c/g K in the fall of 1959, and that the Cs^{137} content of milk reached a low of 7.5 $\mu\mu$c/g K in September 1960. The results suggest stratospheric and tropospheric residence times of 2 years and 2 months respectively.

INTRODUCTION

During the last decade, many measurements have been made of the radioactivity caused by fall-out. Most of these measurements have been made of the total beta activity of the fall-out (for example, by Wolfson and Terentiuk 1960), or of one particular beta-active nuclide, particularly Sr^{90}. Relatively few groups have studied those nuclides which emit gamma rays, largely because of the greater complexity of the apparatus necessary.

During the last three years, measurements of the gamma activity of the human body and its environment have been carried out using the "steel room" at the University of Toronto. In this paper results obtained are reported and commented upon.

CAESIUM-137 IN THE HUMAN BODY

The method by which whole-body measurements of the gamma activity of people are made using a steel room and a 5-in. NaI crystal was described in a previous publication (McNeill and Green 1959*b*). It is, in essence, the same as that employed at the Argonne National Laboratories (for example, by Miller and Marinelli 1956).

Two groups of test subjects have been used in the Toronto work, each of about 25 persons without any history of contact with radioactivity. Not one of the subjects has shown any gamma activity except that due to K^{40} and Cs^{137}. Figure 1 shows the results of measurements of the Cs^{137} content of the body made at the University of Toronto during the period fall 1958 to December 1960, and at the Argonne National Laboratories since 1955. Following normal procedure, the caesium burden of the body is expressed in relation to its potassium content. The absolute values of the figures are based on a calibration made in 1958 with K^{42} in the body. Substandard measurements were made to check the reliability of this calibration at subsequent times.

The figure shows that the Cs^{137} burden passed through a maximum in the fall of 1959. This agrees with measurements made at other centers (for example, by Miller 1960), and it is expected as a result of the reduction of Cs^{137} in foodstuffs consequent to the moratorium on bomb-testing.

[1]Manuscript received January 31, 1961.
Contribution from the Department of Physics, University of Toronto, Toronto 5, Ontario.

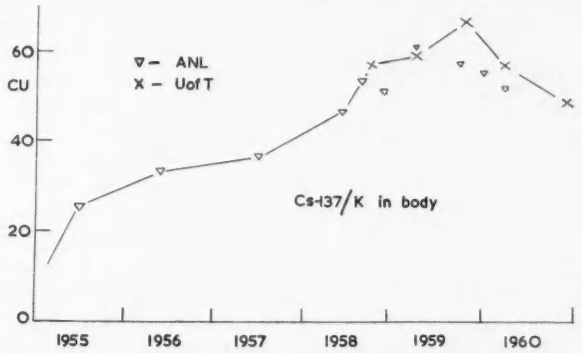

FIG. 1. The variation of the Cs^{137} burden in the human body as a function of time, using measurements made at the Argonne National Laboratories (ANL) and University of Toronto (U of T). The results are expressed in terms of the potassium content of the body, in caesium units of $\mu\mu c$ of Cs^{137}/g of K.

For 21 male students (of average age 22 years) on whom measurements were made in December 1960, the average Cs^{137} burden was 7.5×10^{-3} μc, the average potassium content 0.207% of the total body weight, and the average Cs/K ratio 48.5 $\mu\mu c$/g K. The average weight of the subjects was 159 lb. This Cs^{137} burden is 2.5×10^{-4} the maximum permitted (ICRP 1959).

A level of 7.5×10^{-3} μc in the body is reasonably consistent with a daily intake of 32 $\mu\mu c$ of Cs^{137} via food and with a 115-day half-life for caesium in the body (McNeill and Green 1959*a*). The daily intake figure is based on values found in the spring of 1959 (McNeill and Trojan 1960*b*) reduced by an amount equal to the reduction in Cs^{137} levels in milk between the spring of 1959 and December 1960.

CAESIUM-137 IN MILK AND MEAT

It has been shown that milk and meat are the main contributors of Cs^{137} to the normal Ontario diet (McNeill and Trojan 1960*b*). Using a method discussed earlier (McNeill and Trojan 1960*a*), we have measured the Cs^{137} content of samples of dried milk produced near Toronto since the spring of 1959. Figure 2 illustrates the results.

Reference to the figure shows that the Cs^{137} content rose sharply from a winter plateau in May 1959, fell during the summer until October, and then rose to a winter plateau. In 1960 the Cs^{137} level dropped in May, continued to fall during the summer to a low in late September, and then rose to a winter plateau. These changes are associated with the feeding habits of the cows and the deposition of Cs^{137} onto pasture. May is the month in which cows in Ontario leave the barns for summer pasture; in October they return to barns for the winter. In the barns part of their food is hay collected during the early summer, and it is therefore reasonable that the winter level of the Cs^{137} content reflects the Cs/K ratio of the early summer. The sharp peak

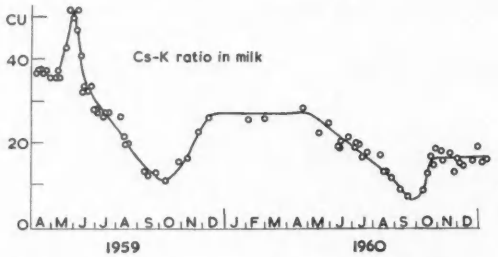

FIG. 2. The variation of the Cs^{137} content, with time, of dried milk from the Toronto milkshed.

in May 1959 is considered to be due to the deposition of relatively large amounts of fall-out from the bomb tests of 1958. May 1960 did not show any such peak.

The lowest value recorded was in September 1960, at which time the specific caesium activity was 7.5 $\mu\mu$c/g K, and the highest value was in May 1959, when the specific caesium activity was 51.5 $\mu\mu$c/g K.

Disregarding the transient effect in May 1959, it can be seen from Fig. 2 that there are three factors with different time constants governing the variation with time of the Cs^{137} content of milk.

One of these factors is the biological half-life of caesium in the cow. When the animal changes diet suddenly, its total Cs^{137} content, and consequently its Cs^{137} output, will change at a rate governed by this half-life. (This conclusion assumes that the caesium content of the body as a whole does not alter radically, and that the only effect is a change in the proportion of radiocaesium.) The rate of change of Cs^{137} in milk after the return of the cows to barns is consistent with a value of 10 to 20 days for the biological half-life, in agreement with the results of Hood and Comar (1953).

Evidence will be presented later that the major introduction of fission products into the troposphere from the stratosphere occurs during the winter and spring, and that during the summer the rate of fall-out decreases at a rate governed by the residence time for tropospheric fall-out. This decrease in rate of fall-out should be reflected in a decrease in the Cs^{137} content of milk if, as is assumed to be the case, most of the Cs^{137} entering the cow comes from dust on the vegetation eaten rather than by absorption of Cs^{137} from the soil by plants and subsequent ingestion by animals. Figure 4, in which we attempt to correlate the data on milk with that obtained from air sampling, discussed in the next section, shows that the rates of decrease of long-lived fission products in milk and air during the summers of 1959 and 1960 are similar. During 1959, the Cs^{137} content in milk decreased by a factor of 2.7 in 3 months, and in 1960 the rate was approximately the same. The corresponding half-life of 2 months for tropospheric fall-out is longer than that found by other groups. Anderson *et al.* (1960) found a value of 20 days, and Gustafson *et al.* (1960) a value of 1 month. Both these values are based on

air sampling, and indeed the results at Toronto on air sampling, presented later, suggest a lower value for 1959. The difference may be due to the fact that not all the Cs^{137} in cows is received via pasture feeding.

During a period free from substantial bomb-testing, the long-term variation of Cs^{137} in milk will be governed by the rate of transfer from the stratospheric reservoir to the troposphere. In the period under review, any nuclear decay of the nuclide is insignificant. It would be expected then that the relative contents of Cs^{137} in milk from year to year would give the half-life for residence of fission products in the stratosphere. Comparing the three winter plateaux, they are in the ratios 37:26:17. This corresponds to a half-life of 1.8 years.

Measurements of the Cs^{137} content of meat have not been so detailed as the milk determinations, but they show a trend similar to that exhibited by the results for milk. The Cs/K ratio in meat is approximately 1.3 times the Cs/K ratio in milk, showing a discrimination against caesium by the mammary gland.

GAMMA ACTIVITY IN AIR-BORNE DUST

The activity of gamma-active fission products in dust has been studied using a Staplex Hi-volume air sampler, with pleated filters TFA type S. It was found that these filters had a collection efficiency identical with that of filters 934-AH, which have approximately 100% collection efficiency for atmospheric dust (Wolfson and Terentiuk 1960). The air sampler was placed on the roof of the Physics Building of the University of Toronto, 80 feet above the ground. Toronto has a latitude of 43° 40′ and a height above sea level of 350 feet. The standard sampling period was 3 days, during which time a total volume of air of 5000 cubic meters passed through the filter (for comparison, it may be noted that the weekly intake of a man is 140 cubic meters).

After removal from the air sampler, the filter papers were placed in individual plastic petri dishes, and then left for 1 week to allow radium products to decay. The dishes were then individually placed under a 5-in. NaI crystal inside the steel room and the spectrum of the gamma rays emitted by the samples was found. By comparison with standard sources the activities of the various components of the gamma rays could be obtained. It should be noted that all figures quoted subsequently in this section refer to "micro-microcuries of gamma activity" i.e., in accord with normal practice in this field, the decay scheme has not been taken into account.

Some preliminary work on the activity of the air was carried out in the spring of 1959, and complete records were kept since the fall of that year. The only clear lines in the spectra can be ascribed to gamma rays resulting from the decay of Zr^{95}, Ru^{103}, and Ru^{106}, and Cs^{137}.

The average monthly results for Zr^{95} and Cs^{137} are shown in Fig. 3. The interpolated values for Zr^{95} activity during the summer of 1959 (for which period no data are available) have been substantiated by direct comparison of spring and fall samples. Furthermore, the indicated rate of decrease during the summer agrees with that found by Gustafson *et al.* (1960).

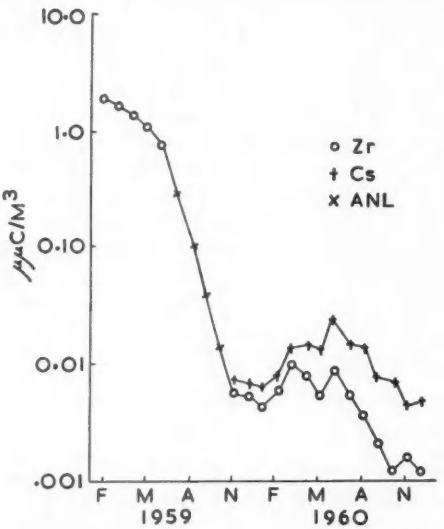

FIG. 3. The variation of the Zr^{95} and Cs^{137} activity, with time, of air-borne dust in Toronto. The results labelled ANL come from the work of Gustafson *et al.* (1960).

Some question has been raised (Stewart *et al.* 1957 and Martell 1959) about whether the rising levels of activity found each spring from 1955 to 1960 are caused by the introduction of old fission products from the stratospheric reservoir into the troposphere through a break in the tropopause or by the fact that until 1959 bomb tests were carried out in the fall of each year. As 1959 was free of bomb tests, the spring maximum in 1960 is strong evidence that a meteorological phenomenon is responsible at least in part. The French tests in February 1960 introduce complication; however, the levels were rising before the tests, and at least in the case of a long-lived nuclide such as Cs^{137} the added amount of activity is small compared with the total amount already present.

Since the major part of the decrease in Zr^{95} activity is due to radioactive decay rather than to a reduction in the rate of fall-out, it is of interest to correct the results for nuclear decay using the start of the experiments, in February 1959, as a convenient base time. In this way the variations in the activity of the shorter-lived isotope may be compared directly with those of Cs^{137}.

The corrected figures corresponding to measurements subsequent to the French tests of 1960 must be treated with reserve as the correction would greatly overemphasize any Zr^{95} from these tests in comparison to Cs^{137} from them. The corrected values for Zr^{95} activity in air-borne dust from February 1959 to February 1960, and Cs^{137} values from November 1959 to December 1960, are shown in Fig. 4.

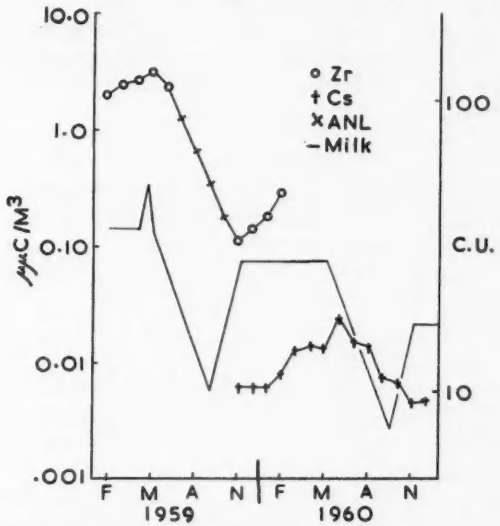

FIG. 4. The variation of Zr^{95} activity of air-borne dust corrected for nuclear decay (to February 1959) compared with the variation in Cs^{137} activity of milk and air-borne dust.

A simplified diagram of the variation of the Cs/K ratio in milk is also drawn in Fig. 4. If we take into account complications introduced by the feeding habits of cows, there is a considerable measure of agreement between the two types of data based on air and milk sampling. For the purpose of making quantitative comparisons, only the decreases in activities in the summers of 1959 and 1960 and the decrease in Cs^{137} activity between December 1959 and December 1960 may be employed. (A comparison employing Zr^{95} data before and after the French tests in February 1960 must be suspect.) From the middle of July 1959 to the middle of October 1959, the air-sampling data gave a decrease in long-lived fall-out by a factor of 7, corresponding to a tropospheric residence time of approximately one month. This agrees with the results of other workers previously quoted. In 1960, the corresponding figures are different, a decrease by a factor of only 2 occurring in the same 3 months. The Cs^{137} figures for milk in the summers have already been given, i.e., a decrease by a factor of about 3 in 3 summer months in both years.

From December 1959 to December 1960, the Cs^{137} content of air-borne dust fell by a factor of 1.4, corresponding to a 2-year half-life for residence of fission products in the stratosphere. This agrees very well with the value derived from the results for milk.

Clearly there is no absolute correlation between the two sets of data, but considering the complications in this field, including, for instance, the possibility of soil-bound Cs^{137} being splashed onto grass and subsequently ingested by animals (Van Wijk and Braams 1960), the agreement is quite reasonable.

In summary, it may be concluded that the measurements show a gradual decrease in long-lived fall-out in Ontario, at a rate corresponding to a stratospheric residence half-life of approximately 2 years. The tropospheric residence half-life would appear to be between 1 and 2 months. This decrease has resulted in a decrease in the Cs^{137} burden in man.

ACKNOWLEDGMENTS

This work has been made possible by a Public Health Grant of the Department of National Health and Welfare, Ottawa, and the Ontario Department of Health. We would like to thank Mr. V. K. Mohindra, who assisted on some of the later measurements, and Dr. W. H. Watson for many helpful discussions.

REFERENCES

ANDERSON, W., BENTLEY, R. E., BURTON, L. K., CROOKALL, J. O., and GREATOREX, C. A. 1960. Nature, **186**, 925.
GUSTAFSON, P. F., BRAR, S. S., and KERRIGAN, M. A. 1960. Argonne National Laboratory Report ANL 6104, 69.
HOOD, S. L. and COMAR, C. L. 1953. Arch. Biochem. Biophys. **45**, 423.
I.C.R.P. 1959. Recommendations of the International Commission on Radiological Protection (Pergamon Press, London).
MCNEILL, K. G. and GREEN, R. M. 1959*a*. Can. J. Phys. **37**, 528.
——— 1959*b*. Can. J. Phys. **37**, 683.
MCNEILL, K. G. and TROJAN, O. A. D. 1960*a*. Nature, **186**, 399.
——— 1960*b*. Health Phys. **4**, No. 2, 109.
MARTELL, E. A. 1959. Science, **129**, 1197.
MILLER, C. E. 1960. Argonne National Laboratory Report ANL 6104, 78.
MILLER, C. E. and MARINELLI, L. D. 1956. Radiology, **66**, 104.
STEWART, N. G., CROOKS, R. N., OSMOND, R. G. D., and FISHER, E. M. R. 1957. A.E.R.E. Harwell Report H.P./R. 2354.
VAN WIJK, H. F. and BRAAMS, R. 1960. Nature, **188**, 951.
WOLFSON, J. F. and TERENTIUK, F. 1960. Can. J. Phys. **38**, 991.

THE ELECTROMAGNETIC FIELDS OF A HORIZONTAL DIPOLE IN THE PRESENCE OF A CONDUCTING HALF-SPACE[1]

JAMES R. WAIT

ABSTRACT

The problem considered is a horizontal electric dipole which is located above or below the plane surface of a conducting half-space. Expressions for the fields are obtained using three different approaches. The formulas developed are quite simple and, taken together, the whole range of distances from the far-zone to the near-zone is adequately covered.

INTRODUCTION

It is well known that a horizontal wire antenna will radiate horizontally polarized electromagnetic waves along the surface of the earth. It is not quite so well known that such an antenna will also radiate vertically polarized radiation. In fact the statement is sometimes made that the field of a horizontal electric dipole in the direction of maximum field is proportional to the field of a vertical *magnetic* dipole. Actually, at low radio frequencies, the field radiated from a low horizontal antenna is predominantly vertically polarized and is proportional to the field of a vertical *electric* dipole.

At very low frequencies (less than 30 kc/s) it would be expected that the radiated field of a horizontal antenna is almost purely polarized in the vertical direction. However, if the range is comparable to the wavelength it is not immediately obvious that this situation prevails. It is the purpose of this paper to investigate this general problem. Expressions are derived for the electromagnetic fields of a horizontal electric dipole which is over, on, or below the surface of a homogeneous conducting half-space.

To facilitate discussion of the past work in this field three overlapping distance ranges are considered. These are:

(i) $\rho \gg \lambda_0$,

(ii) $\rho \sim \lambda_0$,

(iii) $\rho \ll \lambda_0$,

where ρ is the horizontal separation between transmitter and receiver and λ_0 is the free-space wavelength.

Case (i), the radiation field, has been treated in detail by Sommerfeld (1926) and Norton (1937) for the case where the dipole and the observer are in the upper half-space (i.e., the air). The extension to a spherical earth has also been developed (Wait 1956). The radiation field of the horizontal dipole immersed in the half-space has been treated by Moore (1951) in a doctoral thesis and by Banös and Wesley (1953). The problem was also discussed by Wait (1953*a*) in a published note.

Case (ii), the near field, has been considered by Norton (1937), who states that his formulas are valid for distances down to a wavelength. His results are

[1]Manuscript received March 23, 1961.
Contribution from the Central Radio Propagation Laboratory, National Bureau of Standards, Boulder, Colo.

restricted to the upper half-space. This intermediate distance region has also been treated by Banös and Wesley (1953) for the dipole in the half-space.

Case (iii), the quasi-static case, has been treated by Foster (1931) and Fock (1933) for the horizontal dipole on the surface and by Lien (1953) and Wait (1959) for the dipole inside the conducting half-space.

In the present paper simple field expressions are obtained for the three distance ranges mentioned above. No attempt was made to adapt specialized results developed by others; rather, self-contained derivations are given for each case. However, some of the methods are very similar to those employed by the author in earlier papers treating the fields of a magnetic dipole in and over a conducting half-space (Wait 1951, 1952, 1953*b*, 1954, 1959; and Wait and Campbell 1953).

FORMAL SOLUTION

The earth is assumed to be a homogeneous medium with conductivity σ_1, dielectric constant ϵ_1. With reference to a Cartesian co-ordinate system (x,y,z) it occupies the half-space $z < 0$. The air with dielectric constant ϵ_0 occupies the space $z > 0$. The magnetic permeability of the whole space is assumed to be constant and equal to μ. The electric dipole, of infinitesimal length ds, is situated at $(0,0,h)$ and is oriented in the x direction.

The formal solution of this problem was given by Sommerfeld (1926). The method he used is now considered to be straightforward. Expressions for the components of the Hertz vector are derived by matching tangential fields at the interface $z = 0$. He showed that for $z > 0$ and $h \geqq 0$,

$$\frac{\Pi_x}{C_0} = \frac{e^{-\gamma_0 R_0}}{R_0} - \frac{e^{-\gamma_0 R_1}}{R_1} + 2\int_0^\infty \frac{e^{-u_0(z+h)}}{u_0+u_1} J_0(\lambda\rho)\lambda\, d\lambda, \tag{1}$$

$$\Pi_y = 0,$$

$$\frac{\Pi_z}{C_0} = -2\frac{\partial}{\partial x}\int_0^\infty \frac{(u_0-u_1)e^{-u_0(z+h)}}{\gamma_0^2 u_1+\gamma_1^2 u_0} J_0(\lambda\rho)\lambda\, d\lambda, \tag{2}$$

where

$$R_0 = [(z-h)^2+\rho^2]^{\frac{1}{2}}, \qquad R_1 = [(z+h)^2+\rho^2]^{\frac{1}{2}}, \qquad \rho = (x^2+y^2)^{\frac{1}{2}},$$

$$\gamma_0^2 = -\epsilon_0\mu\omega^2, \qquad \gamma_1^2 = i\sigma_1\mu\omega - \epsilon_1\mu\omega^2,$$

$$u_0^2 = \lambda^2+\gamma_0^2, \qquad u_1^2 = \lambda^2+\gamma_1^2, \qquad \text{and } C_0 = Ids/(4\pi i\epsilon_0\omega).$$

Time enters according to the factor $\exp(i\omega t)$.

The fields are then to be obtained from:

$$\mathbf{E} = -\gamma_0^2\boldsymbol{\Pi} + \text{grad div}\,\boldsymbol{\Pi}, \tag{3}$$

$$\mathbf{H} = i\epsilon_0\,\omega\,\text{curl}\,\boldsymbol{\Pi}. \tag{4}$$

When $z < 0$ and $h \geqq 0$ it is found that

$$\frac{\Pi_z}{C_1} = 2\int_0^\infty \frac{e^{uz}e^{-u_0 h}}{u_0+u_1} J_0(\lambda\rho)\lambda\, d\lambda, \tag{5}$$

$$\Pi_y = 0,$$

$$\frac{\Pi_z}{C_1} = -2\frac{\partial}{\partial x}\int_0^\infty \frac{(u_0-u_1)e^{-u_0 h}e^{uz}}{\gamma_0^2 u_1+\gamma_1^2 u_0} J_0(\lambda\rho)\lambda\, d\lambda, \tag{6}$$

where $C_1 = Ids/[4\pi(\sigma_1+i\epsilon_1\omega)]$.

FAR-ZONE FIELDS

In the present work it is assumed consistently that $|\gamma_1| \gg |\gamma_0|$. This situation is quite typical for low radio frequencies. Exceptions may occur when the ground is frozen. Because of the largeness of γ_1^2 it is permissible to replace u_1 by γ_1. Thus

$$\frac{\Pi_z}{C_0} \cong \frac{e^{-\gamma_0 R_0}}{R_0} - \frac{e^{-\gamma_0 R_1}}{R_1} + 2\int_0^\infty \frac{e^{-u_0(z+h)}}{u_0+\gamma_1} J_0(\lambda\rho)\lambda\, d\lambda \tag{7}$$

and

$$\frac{\Pi_z}{C_0} \cong \frac{2}{\gamma_1}\frac{\partial}{\partial x}\int_0^\infty \left(\frac{1}{u_0+\gamma_0^2/\gamma_1} - \frac{1}{u_0+\gamma_1}\right) e^{-u_0(z+h)}\lambda J_0(\lambda\rho)\lambda\, d\lambda. \tag{8}$$

These integrals are of a type which has already been evaluated by Sommerfeld (1926). They may also be treated by a modified saddle-point method (Wait 1957). Therefore, if $k\rho \gg 1$

$$\frac{\Pi_z}{C_0} \cong \frac{e^{-\gamma_0 R_0}}{R_0} - \frac{e^{-\gamma_0 R_1}}{R_1} + 2[1-(p'/w')^{\frac{1}{2}}(1-F(w'))]\frac{e^{-\gamma_0 R_1}}{R_1} \tag{9}$$

where

$$p' = -(ikR_1/2)(\gamma_1/\gamma_0)^2,$$

$$w' = p'\left(1+\frac{z+h}{R_1}\frac{\gamma_0}{\gamma_1}\right)^2,$$

and

$$F(w') \cong -\frac{1}{2w'}.$$

Similarly,

$$\frac{\Pi_z}{C_0} \cong \frac{2}{\gamma_1}\frac{\partial}{\partial x}[1-i(\pi p)^{\frac{1}{2}}e^{-w}\operatorname{erfc}(iw^{\frac{1}{2}})]\frac{e^{-\gamma_0 R_1}}{R_1} \tag{10}$$

where

$$p = -(ikR_1/2)(\gamma_0/\gamma_1)^2,$$

and

$$w = p\left(1+\frac{z+h}{R_1}\cdot\frac{\gamma_1}{\gamma_0}\right)^2.$$

It is immediately evident that the fields derived from Π_x are very similar to those of a vertical magnetic dipole whereas the fields derived from Π_z are related to those of a vertical electric dipole. This is particularly evident when these expressions for Π_x and Π_z are written in the form

$$\frac{\Pi_x}{C_0} \cong 2F(p')(1+\gamma_1 z)(1+\gamma_1 h)e^{-\gamma_0\rho}/\rho \cong [2\gamma_0/(\gamma_1\rho)^2](1+\gamma_1 z)(1+\gamma_1 h)e^{-\gamma_0\rho}, \tag{11}$$

and

$$\frac{\Pi_z}{C_0} \cong -[2\gamma_0/(\gamma_1\rho)]F(p)(\cos\phi)(1+\gamma_0^2 z/\gamma_1)(1+\gamma_0^2 h/\gamma_1)e^{-\gamma_0\rho}, \tag{12}$$

which are valid for small heights (i.e., z^2 and $h^2 \ll \rho^2$). It is seen that the factors which depend on height have the form $(1+ik\Delta z)$ in which $\Delta = \gamma_1/\gamma_0$ or $\Delta = \gamma_0/\gamma_1$.

Using equations (11) and (12) it is a relatively straightforward matter to obtain the following expressions for the fields:

$$E_\rho \cong -\frac{i\mu\omega}{\gamma_1} H_\phi \cong \frac{i\mu\omega Ids}{2\pi\rho}\frac{\gamma_0^2}{\gamma_1^2} F(p)e^{-\gamma_0\rho}(\cos\phi), \qquad \text{for } z = h = 0, \tag{13}$$

$$E_\phi \cong \frac{i\mu\omega}{\gamma_1} H_\rho \cong \frac{i\mu\omega Ids}{\pi\rho^2}\frac{\gamma_0}{\gamma_1^2} e^{-\gamma_0\rho}(\sin\phi), \qquad \text{for } z = h = 0, \tag{14}$$

$$E_z \cong \frac{i\mu\omega Ids}{2\pi\rho}\frac{\gamma_0}{\gamma_1} F(p)e^{-\gamma_0\rho}(\cos\phi)G_V, \qquad \text{for } z \text{ and } h \geqq 0, \tag{15}$$

$$H_z \cong \frac{Ids}{2\pi\rho^2}\frac{\gamma_0^2}{\gamma_1^2} e^{-\gamma_0\rho}(\sin\phi)G_H, \qquad \text{for } z \text{ and } h \geqq 0, \tag{16}$$

where

$$F(p) = 1 - i(\pi p)^{\frac{1}{2}} e^{-p}\operatorname{erfc}(ip^{\frac{1}{2}}),$$

$$G_V = (1+\gamma_0^2 z/\gamma_1)(1+\gamma_0^2 h/\gamma_1),$$

and

$$G_H = (1+\gamma_1 z)(1+\gamma_1 h).$$

Equations (13) to (16) are valid subject to the following approximations:

(i) $|\gamma_0\rho| = k\rho \gg 1$ (i.e., far-field),
(ii) h^2 and $z^2 \ll \rho^2$ (i.e., small heights),
(iii) $|\gamma_1| \gg |\gamma_0|$ (i.e., highly conducting ground).

NEAR-ZONE FIELDS

The use of the saddle-point method to reduce the exact integral forms for Π_x and Π_z to the forms given by equations (9) and (10) requires that $k\rho \gg 1$. When $k\rho$ becomes comparable with unity it is necessary to use a different tack.

In the case $h = z = 0$ it is shown in the Appendix that

$$\frac{\Pi_x}{C_0} = \frac{2}{(\gamma_1^2-\gamma_0^2)\rho^3}[(1+\gamma_0\rho)e^{-\gamma_0\rho} - (1+\gamma_1\rho)e^{-\gamma_1\rho}]. \tag{17}$$

This is an exact result. Now under the restriction that $|\gamma_1\rho| \gg 1$, this simplifies to

$$\frac{\Pi_z}{C_0} \cong \frac{2}{\gamma_1^2\rho^3}(1+\gamma_0\rho)e^{-\gamma_0\rho}. \tag{18}$$

For $|\gamma_0\rho| \gg 1$, this agrees with equation (11). Furthermore, since $|\gamma_1^2| \gg |\gamma_0^2|$ it is reasonable to assume that the factor $\gamma_1^2u_0+\gamma_0^2u_1$ in the exact integral form for Π_z can be replaced by $\gamma_1^2u_0$ for the near zone. Thus

$$\frac{\Pi_z}{C_0} \cong \frac{2}{\gamma_1}\frac{\partial}{\partial x}\int_0^\infty u_0^{-1}e^{-u_0(z+h)}J_0(\lambda\rho)d\lambda \tag{19}$$

$$\cong \frac{2}{\gamma_1}\frac{\partial}{\partial x}(e^{-\gamma_0R_1}/R_1).$$

For $z = h = 0$, this becomes

$$\frac{\Pi_z}{C_0} \cong -(2/\gamma_1\rho^2)(1+\gamma_0\rho)e^{-\gamma_0\rho}\cos\phi. \tag{20}$$

When $|\gamma_0\rho| \gg 1$ and *provided* $p \ll 1$, this agrees with equation (12).

The corresponding forms for Π_z and Π_z when z and $h > 0$ are

$$\frac{\Pi_z}{C_0} \cong (2/\gamma_1^2\rho^3)(1+\gamma_0\rho)e^{-\gamma_0\rho}G_H, \tag{21}$$

$$\frac{\Pi_z}{C_0} \cong -(2/\gamma_1\rho^2)(1+\gamma_0\rho)e^{-\gamma_0\rho}(\cos\phi)G_V. \tag{22}$$

The resulting field expressions are then given by

$$E_\rho \cong -\frac{i\mu\omega}{\gamma_1}H_\phi \cong \frac{i\mu\omega Ids}{2\pi\rho^3\gamma_1^2}(1+\gamma_0\rho+\gamma_0^2\rho^2)e^{-\gamma_0\rho}(\cos\phi) \qquad \text{for } z = h = 0, \tag{23}$$

$$E_\phi \cong \frac{i\mu\omega}{\gamma_1}H_\rho \cong \frac{i\mu\omega Ids}{\pi\rho^3\gamma_1^2}(1+\gamma_0\rho)e^{-\gamma_0\rho}(\sin\phi), \qquad \text{for } z = h = 0, \tag{24}$$

$$E_z \cong \frac{i\mu\omega Ids}{2\pi\rho^2\gamma_1}(1+\gamma_0\rho)e^{-\gamma_0\rho}(\cos\phi)G_V, \qquad \text{for } z \text{ and } h \geqq 0, \tag{25}$$

$$H_z \cong \frac{Ids}{2\pi\rho^4\gamma_1^2}(3+3\gamma_0\rho+\gamma_0^2\rho^2)e^{-\gamma_0\rho}(\sin\phi)G_H, \qquad \text{for } z \text{ and } h \geqq 0. \tag{26}$$

These expressions are valid subject to the following approximations:

(i) $|p| \ll 1$, (i.e., small 'numerical' distances)
(ii) h^2 and $z^2 \ll \rho^2$,
(iii) $|\gamma_1| \gg |\gamma_0|$.

It is seen that the range of validity of equations (13) to (16) and of equations (23) to (26) overlap when, simultaneously, $|p| \ll 1$ and $|\gamma_0\rho| \gg 1$.

The preceding discussion has been restricted to the case where the observer is in the upper half-space. The analysis for the situation where the observer

is in the lower half-space (i.e., $z < 0$) is very similar. The exact integral expressions for Π_x and Π_z then contain a factor $\exp(u_1 z)$ in the integrand. If $|\gamma_1| \gg |\gamma_0|$ and $|\gamma_1 \rho| \gg 1$, this factor may be approximated by $\exp(\gamma_1 z)$ and thus taken outside the integral. The resulting expressions for the fields are identical with equations (23) to (26) for the field components E_ρ, H_ϕ, E_ϕ, H_ρ, and H_z but now G_V and G_H are defined by

$$G_V \cong (1+\gamma_0^2 h/\gamma_1) \exp(\gamma_1 z), \tag{27}$$

$$G_H \cong (1+\gamma_1 h) \exp(\gamma_1 z), \tag{28}$$

and (23) and (24) have a factor $\exp(\gamma_1 z)$ on the right-hand sides. The E_z field component is not continuous at the interface. In fact,

$$E_z(z \to 0-) \cong (\gamma_0^2/\gamma_1^2) E_z(z \to 0+),$$

which indicates that equations (15) and (25) for E_z are applicable to $z < 0$ if G_V is replaced by G_V^1 where

$$G_V^1 = (1+\gamma_0^2 h/\gamma_1)(\gamma_0^2/\gamma_1^2) \exp(\gamma_1 z). \tag{29}$$

The other obvious extension is to the case where the horizontal dipole is lowered into the conducting half-space (i.e., $h < 0$). A factor $\exp(u_1 h)$ is now contained within the integrand of the exact integral expressions. This can be approximated by $\exp(\gamma_1 z)$ subject again to the limitations that $|\gamma_1 \rho| \gg 1$ and $|\gamma_1^2| \gg |\gamma_0^2|$. For $z > 0$, the resulting expressions for the fields are again given by equations (13) to (16) and (23) to (26) if

$$G_V \cong \exp(\gamma_1 h)(1+\gamma_0^2 z/\gamma_1), \tag{30}$$

$$G_H \cong \exp(\gamma_1 h)\ (1+\gamma_1 z), \tag{31}$$

and (23) and (24) for $z = 0$ are now multiplied by $\exp(\gamma_1 h)$.

For $z < 0$

$$G_V \cong \exp(\gamma_1 h) \exp(\gamma_1 z) \cong G_H \tag{32}$$

except for the E_z component which requires that

$$G_V \cong (\gamma_0^2/\gamma_1^2) \exp(\gamma_1 h) \exp(\gamma_1 z). \tag{33}$$

Furthermore, (23) and (24) are still valid provided the right-hand sides are multiplied by $\exp(\gamma_1 h) \exp(\gamma_1 z)$.

QUASI-STATIC APPROACH

At very short distances where the condition $|\gamma_1 \rho| \gg 1$ becomes violated it is necessary to use a quasi-static treatment. If $|\gamma_0 \rho| \ll 1$ it is permissible to regard the fields in the upper insulating half-space as solutions of Laplace's equation. This is equivalent to setting γ_0 equal to zero in the exact integral expressions for Π_x and Π_z. For $z < 0$ and $h \leqq 0$ these may be written

$$\Pi_z = \frac{Ids}{4\pi(\sigma+i\omega\epsilon)}\left[\frac{e^{-\gamma R_0}}{R_0}-\frac{e^{-\gamma R_1}}{R_1}+2\int_0^\infty \frac{e^{u(z+h)}}{u+\lambda} J_0(\lambda\rho)\lambda\, d\lambda\right] \tag{34}$$

and

$$\Pi_z = \frac{Ids}{2\pi(\sigma+i\omega\epsilon)}\frac{\partial}{\partial x}\int_0^\infty \frac{e^{u(z+h)}}{u+\lambda} J_0(\lambda\rho)\, d\lambda \tag{35}$$

where $\gamma^2 = \gamma_1^2 = i\mu\omega(\sigma+i\epsilon\omega)$ and $u = u_1 = (\lambda^2+\gamma^2)^{\frac{1}{2}}$. (The subscript 1 is dropped for the sake of brevity in the remainder of this section.)

As z and h approach zero (from negative values) it easily follows, from equation (17), that

$$\Pi_z = \frac{Ids}{2\pi(\sigma+i\omega\epsilon)}\frac{1}{\gamma^2\rho^3}[1-(1+\gamma\rho)e^{-\gamma\rho}]. \tag{36}$$

The integral involved in Π_z is not quite so simple. However, it may be reduced as follows

$$\int_0^\infty \frac{J_0(\lambda\rho)}{u+\lambda}\, d\lambda = \frac{1}{\gamma^2}\int_0^\infty (u-\lambda) J_0(\lambda\rho)\, d\lambda. \tag{37}$$

Since

$$\int_0^\infty \lambda J_0(\lambda\rho) d\lambda = 0$$

and using

$$\left(\frac{1}{\rho}\frac{\partial}{\partial\rho}\rho\frac{\partial}{\partial\rho}+\lambda^2\right)J_0(\lambda\rho) = 0,$$

it is seen that

$$\gamma^2\int_0^\infty \frac{J_0(\lambda\rho)}{u+\lambda}\, d\lambda = \left(\gamma^2-\frac{1}{\rho}\frac{\partial}{\partial\rho}\rho\frac{\partial}{\partial\rho}\right)\int_0^\infty \frac{J_0(\lambda\rho)}{u}\, d\lambda. \tag{38}$$

According to Watson (1944) the integral on the right-hand side is equal to $I_0(\gamma\rho/2)K_0(\gamma\rho/2)$ where I_0 and K_0 are modified Bessel functions of the first and second kind, both with argument $\gamma\rho/2$. Thus, for $z = h = 0-$

$$\Pi_z = \frac{Ids\cos\phi}{2\pi(\sigma+i\epsilon\omega)\gamma^2}\frac{\partial}{\partial\rho}\left(\gamma^2-\frac{1}{\rho}\frac{\partial}{\partial\rho}\rho\frac{\partial}{\partial\rho}\right)[I_0(\gamma\rho/2)K_0(\gamma\rho/2)]. \tag{39}$$

In a similar fashion it is found that, for $z = h = 0-$,

$$\frac{\partial\Pi_z}{\partial z} = -\frac{Ids}{2\pi(\sigma+i\epsilon\omega)\gamma^2}\left(\frac{1}{\rho}\frac{\partial}{\partial\rho}\rho\frac{\partial}{\partial\rho}\right)\left(\frac{1}{\rho}\frac{\partial}{\partial\rho}\rho\frac{\partial}{\partial\rho}-\gamma^2\right)[I_0(\gamma\rho/2)K_0(\gamma\rho/2)] \tag{40}$$

and

$$\operatorname{div}\mathbf{\Pi} = -\frac{Ids\cos\phi}{2\pi(\sigma+i\epsilon\omega)\rho^2}. \tag{41}$$

The field components in the interface are then obtained from

$$E_\rho = -\gamma^2 \Pi_z \cos\phi + \frac{\partial}{\partial\rho} \operatorname{div} \mathbf{\Pi}, \tag{42a}$$

$$E_\phi = \gamma^2 \Pi_z \sin\phi + \frac{1}{\rho}\frac{\partial}{\partial\phi} \operatorname{div} \mathbf{\Pi}, \tag{42b}$$

$$H_\rho = (\sigma + i\epsilon\omega)\left[\frac{\partial \Pi_z}{\rho\partial\phi} + \frac{\partial \Pi_z}{\partial z}\sin\phi\right], \tag{42c}$$

$$H_\phi = (\sigma + i\epsilon\omega)\left[\frac{\partial \Pi_z}{\partial z}\cos\phi - \frac{\partial \Pi_z}{\partial\rho}\right], \tag{43a}$$

$$H_z = -(\sigma + i\epsilon\omega)\frac{\partial \Pi_z}{\partial\rho}\sin\phi. \tag{43b}$$

Within the limits of quasi-static theory E_z vanishes inside the conducting medium for $h = 0$ and z tending to zero from negative values (i.e., $z \to 0-$). On the other hand, if $h = 0$ and z tends to zero from the positive values (i.e., $z \to 0+$) it is found that

$$E_z = -\frac{i\mu\omega Ids}{2\pi}\frac{\partial}{\partial x}\int_0^\infty \frac{J_0(\lambda\rho)}{u+\lambda}\,d\lambda \tag{44}$$

$$= -\frac{i\mu\omega Ids}{2\pi\gamma^2}\cos\phi\,\frac{\partial}{\partial\rho}\left(\gamma^2 - \frac{1}{\rho}\frac{\partial}{\partial\rho}\rho\frac{\partial}{\partial\rho}\right)\left[I_0\left(\frac{\gamma\rho}{2}\right)K_0\left(\frac{\gamma\rho}{2}\right)\right]. \tag{45}$$

In the limiting case where $|\gamma\rho| \gg 1$ it is seen that

$$E_z \cong \frac{i\mu\omega Ids}{2\pi\gamma\rho^2}\cos\phi. \tag{46}$$

The field components E_ρ, E_ϕ, and H_ϕ in this quasi-static approximation may then be written concisely in the form

$$E_\rho = \frac{Ids}{2\pi(\sigma + i\epsilon\omega)\rho^3}\left[1 + (1+\gamma\rho)e^{-\gamma\rho}\right]\cos\phi, \tag{47}$$

$$E_\phi = \frac{Ids}{2\pi(\sigma + i\epsilon\omega)\rho^3}\left[2 - (1+\gamma\rho)e^{-\gamma\rho}\right]\sin\phi, \tag{48}$$

$$H_z = \frac{Ids}{2\pi\gamma^2\rho^4}\left[3 - (3+3\gamma\rho+\gamma^2\rho^2)e^{-\gamma\rho}\right]\sin\phi. \tag{49}$$

These results are valid for $z = h = 0$ and $|\gamma_0\rho| \ll 1$. The value of $\gamma\rho$ is unrestricted. In particular, if $|\gamma\rho|$ approaches zero the above reduce to

$$E_\rho = \frac{Ids}{\pi(\sigma + i\epsilon\omega)\rho^3}\cos\phi, \tag{50}$$

$$E_\phi = \frac{Ids}{2\pi(\sigma + i\epsilon\omega)\rho^3}\sin\phi, \tag{51}$$

$$H_z = \frac{Ids}{4\pi\rho^2}\sin\phi. \tag{52}$$

These elementary forms are consistent with potential theory.

Another interesting check is to note that if, simultaneously, $|\gamma_0\rho| \ll 1$ and $|\gamma\rho| \gg 1$, equations (47), (48), and (49) agree with (23), (24), and (26) for $z = h = 0$.

Apparently the field components H_ρ and H_ϕ for $z = h = 0$ cannot be written in a concise form. The higher derivatives of I_0K_0 can be reduced to a linear combination of the functions I_0K_0, I_0K_1, I_1K_0, and I_1K_1 where I_1 and K_1 are modified Bessel functions of order unity. These forms will not be written out. However, it is of interest to note that if $|\gamma\rho| \gg 1$ each of these products can be replaced by $1/(\gamma\rho)$ where the error is of order $1/(\gamma\rho)^2$. To this approximation

$$H_\rho \cong \frac{Ids \sin \phi}{\pi\gamma\rho^3} \cong \frac{\gamma}{i\mu\omega} E_\phi, \tag{53}$$

$$H_\phi \cong -\frac{Ids \cos \phi}{2\pi\gamma\rho^3} \cong -\frac{\gamma}{i\mu\omega} E_\rho. \tag{54}$$

The previous discussion of the quasi-static case was restricted to the case $z = h = 0$. The manner in which the fields vary with z or h in this range (i.e., $|\gamma_0\rho| \ll 1$) is quite complicated. For example, the fields do not generally vary in a simple exponential manner with depth into the conductor. Nevertheless, for the case z and $h < 0$, it is possible to express the fields in terms of modified Bessel functions. Setting $\gamma_0 = 0$ it is found that

$$\Pi_z = \frac{Ids}{4\pi(\sigma+i\epsilon\omega)}\left[\frac{e^{-\gamma R_0}}{R_0} - P + \frac{2}{\gamma^2}\left(\frac{\partial^2 P}{\partial z^2} - \frac{\partial^3 N}{\partial z^3} + \gamma^2 \frac{\partial N}{\partial z}\right)\right] \tag{55}$$

and

$$\Pi_z = \frac{Ids}{2\pi(\sigma+i\epsilon\omega)}\left(\frac{\partial^3 N}{\partial x \partial z^2} - \frac{\partial^2 P}{\partial x \partial z}\right) \tag{56}$$

where

$$N = \int_0^\infty \frac{e^{u(z+h)}}{u} J_0(\lambda\rho) d\lambda, \tag{57}$$

$$P = \int_0^\infty \frac{e^{u(z+h)}}{u} J_0(\lambda\rho)\lambda\, d\lambda = \frac{e^{-\gamma R_1}}{R_1}. \tag{58}$$

The form of equations (55) and (56) may be readily verified by carrying out the indicating differentiations and comparing the results with equations (34) and (35).

The integral N is known. From Foster (1931) or Magnus and Oberhettinger (1954)

$$N = I_0[(\gamma/2)[R_1+(z+h)]]K_0[(\gamma/2)[R_1-(z+h)]]. \tag{59}$$

This result can be checked by noting that equation (59) reduces to the integral in equation (38) when $z+h = 0$, and by seeing that N satisfies the wave equation $(\nabla^2-\gamma^2)N = 0$ when z and $h < 0$.

The electric field in the conducting half-space may now be found from

$$\mathbf{E} = -\gamma^2\mathbf{\Pi} + \text{grad div } \mathbf{\Pi}.$$

Expressing these in Cartesian co-ordinates it is found, after some simplification, that

$$(60)\quad E_x = \frac{Ids}{4\pi(\sigma+i\epsilon\omega)}\left[-\left(\frac{\partial^2}{\partial y^2}+\frac{\partial^2}{\partial z^2}\right)\left(\frac{e^{-\gamma R_0}}{R_0}-P\right)-2\left(\frac{\partial^3 N}{\partial y^2\partial z}+\frac{\partial^2 P}{\partial z^2}\right)\right],$$

$$(61)\quad E_y = \frac{Ids}{4\pi(\sigma+i\epsilon\omega)}\left[\frac{\partial^2}{\partial x\partial y}\left(\frac{e^{-\gamma R_0}}{R_0}-P\right)+2\frac{\partial^3 N}{\partial x\partial y\partial z}\right],$$

$$(62)\quad E_z = \frac{Ids}{4\pi(\sigma+i\epsilon\omega)}\left[-\frac{\partial^2}{\partial x\partial z}\left(\frac{e^{-\gamma R_0}}{R_0}+P\right)\right].$$

As a check on these results it may be noted that as $|\gamma R_0|$ and $|\gamma R_1| \to 0$, the electric field components can be expressed as gradients of a scalar potential. Thus

$$(63)\quad \mathbf{E} = \frac{Ids}{4\pi(\sigma+i\epsilon\omega)}\,\text{grad}\left[\frac{\partial}{\partial x}\left(\frac{1}{R_0}+\frac{1}{R_1}\right)\right].$$

This result is consistent with potential theory.

Another interesting limiting case is when $|\gamma\rho| \gg 1$ and $z+h \ll \rho$. Under these conditions the Bessel functions I_0 and K_0 may be replaced by the first terms in their respective asymptotic expansions. This leads to the asymptotic approximations

$$(64)\quad N \cong (1/\gamma\rho)\exp(\gamma(z+h))$$

and

$$\partial N/\partial z \cong (1/\rho)\exp(\gamma(z+h)).$$

The field components are then given by

$$(65)\quad E_x \cong -\frac{Ids}{2\pi(\sigma+i\epsilon\omega)}e^{\gamma(z+h)}\frac{\partial^2}{\partial y^2}\left(\frac{1}{\rho}\right),$$

$$(66)\quad E_y \cong \frac{Ids}{2\pi(\sigma+i\epsilon\omega)}e^{\gamma(z+h)}\frac{\partial^2}{\partial x\partial y}\left(\frac{1}{\rho}\right).$$

Expressing these in cylindrical co-ordinates

$$(67)\quad E_\rho \cong \frac{Ids\cos\phi}{2\pi(\sigma+i\epsilon\omega)\rho^3}e^{\gamma(z+h)},$$

$$(68)\quad E_\phi \cong \frac{Ids\sin\phi}{\pi(\sigma+i\epsilon\omega)\rho^3}e^{\gamma(z+h)}.$$

These are in agreement with equations (23) and (24) under the conditions that $|\gamma_0\rho| \ll 1$, $|\gamma\rho| \gg 1$, and z and $h \leqq 0$.

The manner in which the exponential factor $\exp(\gamma(z+h))$ occurs is rather interesting. It is only in the integral N that this factor emerges. The integral P, within the approximation that $|\gamma\rho| \gg 1$, gives a negligible contribution.

This exponential factor is usually obtained by somewhat heuristic arguments. In the quasi-static treatment it is established on a sound basis and the limits of its validity are given.

ACKNOWLEDGMENTS

I would like to thank Mrs. Eileen Brackett for her assistance in preparing the manuscript and Mr. Kenneth Spies for his careful reading of the paper. I also wish to thank F. J. Zucker for suggesting the problem. The research was sponsored by the U.S. Air Force Cambridge Research Laboratories under contract A58-40.

REFERENCES

BANÖS, A. and WESLEY, J. P. 1953. Report from Marine Physical Laboratory, University of California.
FOCK, V. A. 1933. Ann. phys. **17**, 401.
FOSTER, R. M. 1931. Bell System Tech. J. **10**, 408.
LIEN, R. H. 1953. J. Appl. Phys. **24**, 1.
MAGNUS, W. and OBERHETTINGER, F. 1954. Functions of mathematical physics (Chelsea Publ. Co. New York), p. 133.
MOORE, R. K. 1951. Ph.D. Thesis, Cornell University.
NORTON, K. A. 1937. Proc. I.R.E. **25**, 1203.
SOMMERFELD, A. N. 1926. Ann. Physik, **81**, 1135.
WAIT, J. R. 1951. Can. J. Phys. **29**, 577.
——— 1952. J. Appl. Phys. **23**, 497.
——— 1953*a*. J. Appl. Phys. **24**, 958 (in equation (6) V should be replaced by U).
——— 1953*b*. Trans. Am. Geophys. Union, **34**, 185.
——— 1954. Can. J. Technol. **32**, 1.
——— 1956. Can. J. Phys. **34**, 586.
——— 1957. J. Research Natl. Bur. Standards, **59**, 365.
——— 1959. Appl. Sci. Research, **B8**, 213.
WAIT, J. R. and CAMPBELL, L. L. 1953. J. Geophys. Research, **58**, 167.
WATSON, G. N. 1944. Bessel functions, 2nd ed. (Cambridge University Press).

APPENDIX

It is of interest to observe that the vertical component of the magnetic field may be expressed in closed form. The first step is to note that Π_z evaluated at $h = 0$ and $z = 0+$ is given by

$$\frac{\Pi_z}{C_0} = 2\int_0^\infty \frac{J_0(\lambda\rho)}{u_0+u_1}\,\lambda\, d\lambda. \tag{69}$$

Multiplying numerator and denominator by u_1-u_0 it follows that

$$\frac{\Pi_z}{C_0} = \frac{2}{\gamma_1^2-\gamma_0^2}\left[\int_0^\infty \lambda u_1 J_0(\lambda\rho)d\lambda - \int_0^\infty \lambda u_0 J_0(\lambda\rho)d\lambda\right]. \tag{70}$$

From Watson (1944)

$$\int_0^\infty u_1^{-1}\lambda J_0(\lambda\rho)\, d\lambda = \rho^{-1}e^{-\gamma_1\rho} \tag{71}$$

and using

$$\left(\frac{1}{\rho}\frac{\partial}{\partial\rho}\rho\frac{\partial}{\partial\rho}+\lambda^2\right) J_0(\lambda\rho) = 0 \tag{72}$$

it follows that

$$(73)\qquad \frac{\Pi_z}{C_0} = \frac{2}{\gamma_1^2-\gamma_0^2}\left[\left(\gamma_1^2-\frac{1}{\rho}\frac{\partial}{\partial\rho}\rho\frac{\partial}{\partial\rho}\right)\frac{e^{-\gamma_1\rho}}{\rho}-\left(\gamma_0^2-\frac{1}{\rho}\frac{\partial}{\partial\rho}\rho\frac{\partial}{\partial\rho}\right)\frac{e^{-\gamma_0\rho}}{\rho}\right]$$

$$= \frac{-2}{(\gamma_1^2-\gamma_0^2)\rho^3}\left[(1+\gamma_1\rho)e^{-\gamma_1\rho}-(1+\gamma_0\rho)e^{-\gamma_0\rho}\right].$$

Then

$$(74)\qquad H_z = -(i\epsilon_0\omega)\frac{\partial\Pi_z}{\partial\rho}\sin\phi$$

$$= \frac{Ids\sin\phi}{2\pi(\gamma_1^2-\gamma_0^2)\rho^4}\left[(3+3\gamma_0\rho+\gamma_0^2\rho^2)e^{-\gamma_0\rho}-(3+3\gamma_1\rho+\gamma_1^2\rho^2)e^{-\gamma_1\rho}\right].$$

This is an exact result valid when $z = h = 0$. In the limiting case for $|\gamma_1\rho| \gg 1$, it agrees with equation (26), and if $|\gamma_0\rho| \ll 1$, it agrees with equation (49). It should be noted that strictly the integrals in equations (70) and (71) are divergent. The operations performed, using these relations, can be made rigorous by simply replacing

$$\int_0^\infty [\ldots]\,d\lambda \text{ by } \lim_{\alpha\to 0}\int_0^\infty e^{-\lambda\alpha}[\ldots]\,d\lambda.$$

ON MEASUREMENT OF THERMAL CONDUCTIVITY AT HIGH TEMPERATURES[1]

M. J. Laubitz

ABSTRACT

A method is given for exact mathematical analysis of linear heat flow systems used in measuring thermal conductivity at high temperatures. It is shown that a popular version of such a system is very sensitive to the alignment of its components, which seriously limits the temperature range of its satisfactory use.

INTRODUCTION

For the past several years great interest has been shown in the thermal conductivity of solids at high temperature. Diverse methods for the determination of thermal conductivity and the results obtained for various solids have been reported in the literature. However, the agreement among the experimental results, particularly for ceramics, has not been spectacular. The variation in values obtained for the thermal conductivity of ceramics has been generally ascribed to the nature of the specimen and its microstructure and impurities. The variation in the structure and composition of the specimen is undoubtedly responsible for a large part of the disagreement of the reported experimental results, but another factor, the straightforward uncertainty of the experimental determination, also plays an important role, usually grossly underestimated. The exaggerated accuracy sometimes reported for values of thermal conductivity at high temperatures is the result of an excessive confidence in the accuracy of thermocouples, and ignorance of the heat flow and temperature patterns developed in the experimental arrangements. Most experiments, particularly the steady-state ones, aim at the establishment of a simple heat flow pattern. The actual heat flow patterns do, of course, deviate from those assumed, but such deviations are usually considered negligible. This article is written to show the importance of those neglected deviations of the heat flow patterns, and to stress the necessity of precise mathematical analyses of the experimental arrangements used for measuring thermal conductivity.

The steady-state methods of measuring thermal conductivity employ either of two heat flow patterns: radial or linear (the ellipsoidal method of Adams (1954) is essentially a variation of the radial heat flow method). Of the two, the linear method has lately been the more popular and will be discussed mathematically in the following pages, where first there will be given a general outline of the mathematical approach, and then a detailed analysis of one particular experimental arrangement.

[1]Manuscript received March 3, 1961.
Contribution from the Division of Applied Physics, National Research Council, Ottawa, Canada.
Issued as N.R.C. No. 6363.

Can. J. Phys. Vol. 39 (1961)

MATHEMATICAL ANALYSIS OF THE LINEAR HEAT FLOW METHOD OF MEASURING THERMAL CONDUCTIVITY

A general arrangement of a linear heat flow apparatus is shown in Fig. 1. (A) is the specimen of radius a and conductivity k_1, (D) is the guard, of thickness $b-d$ and conductivity k_4. The space between the guard and specimen (B) is filled with an insulating substance of conductivity k_2, and outside the guard (C) there is insulation of conductivity k_3. The outside diameter of the apparatus is $2c$, and its length L. There are several heaters wound on

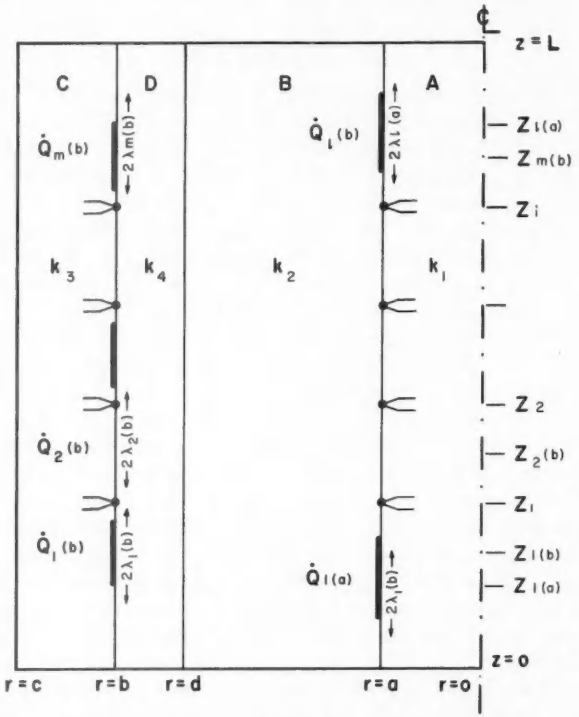

FIG. 1. A general arrangement of a linear heat flow apparatus.

the guard: the mth heater, of length $2\lambda_m(b)$ and positioned at $z_m(b)$, dissipating power $\dot{Q}_m(b)$ per unit length. There are also heaters on the specimen. The lth of these, of length $2\lambda_l(a)$, is positioned at $z_l(a)$ and dissipates power $\dot{Q}_l(a)$ per unit length. There are i thermocouples located at both the guard and the sample, at positions z_i.

A few conditions must be assumed for a complete mathematical analysis

of the system. Primarily, all the conductivities are assumed independent of temperature. This is not a severe limitation, as indicated by the very good agreement between calculated and observed temperature distributions shown in Fig. 2. Then, radial symmetry is assumed, and to make calculation easier, the temperatures along $z = 0$ and $z = L$, and along $r = c$ are all assumed zero. These again are not very critical assumptions, as the surface temperatures have little effect on temperature and heat flow distributions in the inside of the furnace (see, for instance, Laubitz 1959).

Under these conditions, the temperature in region X (X stands for A, B, C, or D) are given by,

$$T(r, z) = \sum_n [F_n(X) I_0(\alpha_n r) + G_n(X) K_0(\alpha_n r)] \sin \alpha_n z$$

where I_0 and K_0 are the associated Bessel functions, $\alpha n = n\pi/L$, and $F_n(X)$ and $G_n(X)$ are constants for each region X. $G_n(A)$ is, of course, zero. The constants $F_n(X)$ and $G_n(X)$ are so chosen as to satisfy the continuity conditions at the interfaces of the regions A, B, C, and D. The temperatures of interest are those along $r = b$ and $r = a$, and it can readily be shown that

$$(1) \quad T(x, z) = \sum_l \sum_n \frac{\dot{Q}_l(a)}{2\pi k_2 a} \cdot f_n(x) \sin \alpha_n \lambda_l(a) \sin \alpha_n z_l(a) \sin \alpha_n z + \sum_m \sum_n \frac{\dot{Q}_m(b)}{2\pi k_3 b} \cdot g_n(x) \cdot \sin \alpha_n \lambda_m(b) \sin \alpha_n z_n(b) \sin \alpha_n z$$

where x is a or b, and $f_n(x)$ and $g_n(x)$ are functions of the ratios of conductivities and the parameters of the apparatus. These functions are too complicated to be given here, but their explicit formulae are given in Laubitz (1961). The above equation shows that the temperatures at any point along a or b are given by equations linear in the power inputs. Once the coefficients of these equations are calculated, it is then a simple matter to study the effects of lateral temperature match or mismatch, of relative displacements of specimen and guard, and other possible conditions affecting the behavior of the apparatus.

To check the stringency of the assumptions made in the derivation of the formulae, calculated and observed temperature distributions were compared for a furnace available in this laboratory. This furnace was 32 cm long and had an outside diameter of 25 cm. The guard, of dense alumina, had seven heaters and six thermocouples. The specimen, also of alumina, had two heaters and also six thermocouples. Regions B and C were filled with powdered alumina. Two comparisons were made: one with the guard maintained at a uniform temperature $T_0 = 1000°$ C, and no heat input into the sample heaters, and the other with only the sample heaters energized. The calculated and observed relative temperature distributions, in excellent agreement with each other, are shown in Fig. 2. In the calculations, the summation of the infinite series was carried up to 12 terms.

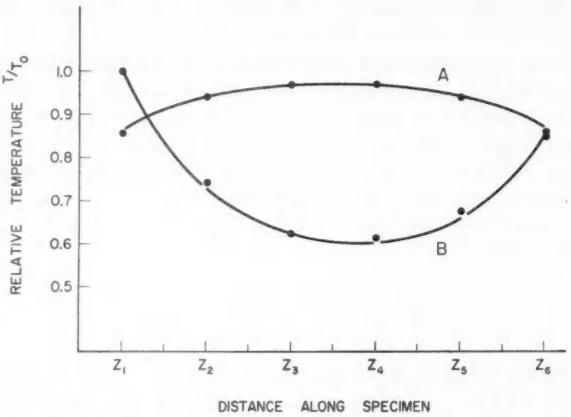

FIG. 2. Comparison of observed and calculated relative temperature distributions: A, uniform guard temperature of T_0, no power into sample heaters; B, no power into guard heaters. Lines are calculated temperatures, and dots observed temperatures.

DETAILED DESCRIPTION OF A PARTICULAR FURNACE

The usefulness of the mathematical analysis in the measurement of thermal conductivity using linear flow lies in the fact that accurate formulae can be obtained for two of the major sources of experimental error, lateral temperature mismatch and relative specimen–guard displacement. Unfortunately, the general formulae for these effects are too unwieldy to show the relationship between the pertinent factors; each apparatus has to be analyzed separately. As an example, one analysis is given here in some detail. It is pertinent to a design very similar to one originally described by Francl and Kingery (1954), with five heaters on the guard, two on the specimen, and four thermocouples located on each of the guard and specimen. In the calculation, the parameters assumed, given as ratios to the length L, were as follows:

$$a = 0.058 \qquad z_1 = 0.326$$
$$b = 0.174 \qquad z_2 = 0.442$$
$$c = 0.465 \qquad z_3 = 0.558$$
$$d = 0.151 \qquad z_4 = 0.674$$
$$z_1(b) = z_1(a) = 0.256 \qquad \lambda_1(b) = \lambda_5(b) = 0.070$$
$$z_2(b) = 0.384 \qquad \lambda_2(b) = \lambda_3(b) = \lambda_4(b) = 0.047$$
$$z_3(b) = 0.500 \qquad \lambda_1(a) = \lambda_2(a) = 0.064$$
$$z_4(b) = 0.616$$
$$z_5(b) = z_2(a) = 0.744$$

The conductivities of guard and specimen were assumed equal (k_1), and so were those of regions B and C (k_2).

Although the factors $f_n(x)$ and $g_n(x)$ of equation (1) decrease as n^{-2}, the convergence of the series is spoiled by the sines. To find the minimum number of terms required to give good results, the temperature distribution along

the specimen was calculated as a function of the number of terms summed for $k_1/k_2 = \infty$ and $\dot{Q}_1(a) = \dot{Q}_2(a)$. The results are shown in Fig. 3, as deviations from the linear interpolation of temperatures between points z_1 and z_4.

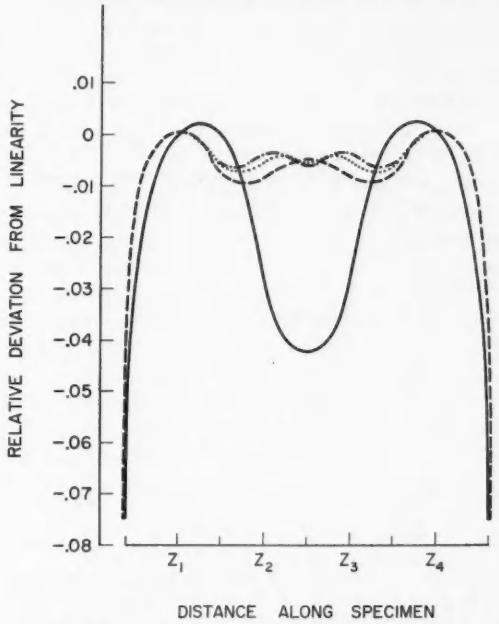

FIG. 3. Calculated deviations from linearity in the temperature distribution along the specimen for $k_1/k_2 = \infty$, as a function of the number of terms in the summation: —— 6 terms; – – – 12 terms; · · · 16 terms; – · – · 24 terms.

Figure 3 is typical of an approach made by a Fourier series to the function it represents: the series quickly reaches a level within about one per cent of the function, and then slowly settles down to its final shape. In this particular case, summation over 12 terms gives temperatures well within one per cent of the ultimate ones, which is sufficient for the study of errors. It is important to note, however, that the ultimate temperature distribution deviates from linearity, best shown by the effect of summation on the temperature of the specimen mid-point.

As all calculations of thermal conductivity in such a system are based on assumption of linearity of temperature, any deviation therefrom is a source of error. There are two aspects to the deviation: its magnitude, which is conveniently given by the magnitude of the deviation at the mid-point of the specimen relative to the specimen temperature, T_0; and its "symmetry", which can be described by the deviation of the ratio R from unity, where

$$R = \frac{2[T(a, z_2) - T(a, z_3)]}{T(a, z_1) - T(a, z_2) + T(a, z_3) - T(a, z_4)}.$$

If the apparatus is used for comparative determination of thermal conductivity, R is the ratio of the conductivity of the unknown to that of the standard. For a system symmetrical in the z-direction, R is only a function of the ratio of the conductivities, k_1/k_2. The relative temperature deviation from linearity of the specimen mid-point depends not only on k_1/k_2, but also on the over-all specimen temperature gradient, $\Delta T = T(a, z_1) - T(a, z_4)$. Figure 4 shows both

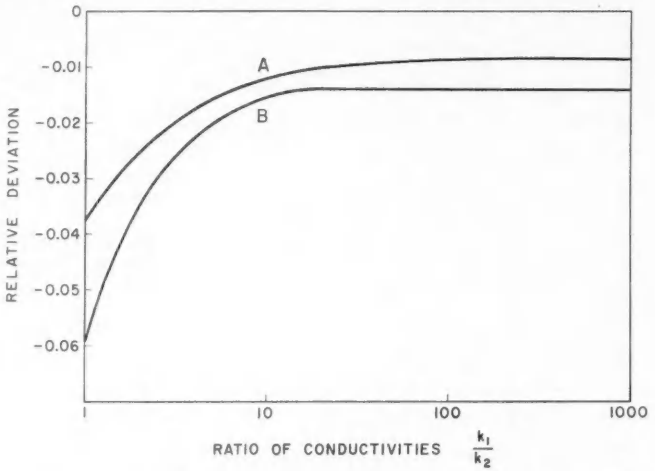

FIG. 4. Relative deviation from linearity of the specimen mid-point temperature (curve A) and deviation from unity of R (curve B) as a function of k_1/k_2.

these deviations as a function of k_1/k_2, for $\Delta T/T_0 = 0.05$. It can readily be appreciated that the deviation from linearity of the mid-point temperature is an error in absolute determination of thermal conductivity, while the deviation of R from unity is an error in comparative measurements.

The errors mentioned above occur in a perfectly matched system, that is one where $T(b, z_i) = T(a, z_i)$. Lateral specimen-guarded temperature mismatch is another source of error. Its treatment within this analysis is elementary. If we define $e_i = T(a, z_i) - T(b, z_i)$, the algebraic mismatch of the ith set of thermocouples, then temperature deviation along the sample caused by these mismatches will be sums of the e_i multiplied by coefficients which, for any particular apparatus, are only functions of k_1/k_2. As an example, the error in R due to mismatch, E, for the particular system here considered is

$$E = -\frac{0.58\,(e_1-e_4)+1.94\,(e_2-e_3)}{\Delta T} \qquad k_1/k_2 = 1,$$

$$= -\frac{0.17\,(e_1-e_4)+0.57\,(e_2-e_3)}{\Delta T} \qquad k_1/k_2 = 10,$$

$$= -\frac{0.03\,(e_1-e_4)+0.09\,(e_2-e_3)}{\Delta T} \qquad k_1/k_2 = 100.$$

The errors e_i can arise from random mismatch, inaccurate thermocouple location or reading, or from relative specimen–guard displacements.

An interesting feature of the apparatus here considered, and one that does not seem to have been appreciated heretofore, is that it contains more arbitrary variables than restraining conditions. The variables are the seven independently variable heaters; the restraining conditions are the specimen temperature T_0, the gradient (ΔT) along it, and the four lateral temperature matches, only six in all. There is a further seventh condition, but it is weak: power inputs cannot be less than zero. Within that last condition, there is a wide range of heater settings that will satisfy the previous six conditions. This in itself has certain advantages, as it facilitates the matching of the guard and specimen temperature. Unfortunately, it also results in an arbitrariness in the temperature distribution of the guard and specimen, which greatly increases the uncertainty of the experimental results. As an example, Fig. 5 shows the relative deviation of temperature from linearity for the guard and specimen for various permissible heater settings. The limits on the settings are given by $\dot{Q}_3(b) = 0$, and $\dot{Q}_4(b) = 0$, and from Fig. 5 it is seen that, although the specimen temperatures are not seriously affected, the guard temperatures vary extensively. The variation in guard temperature is of no consequence if the guard and specimen are perfectly aligned. If, however, there is a relative

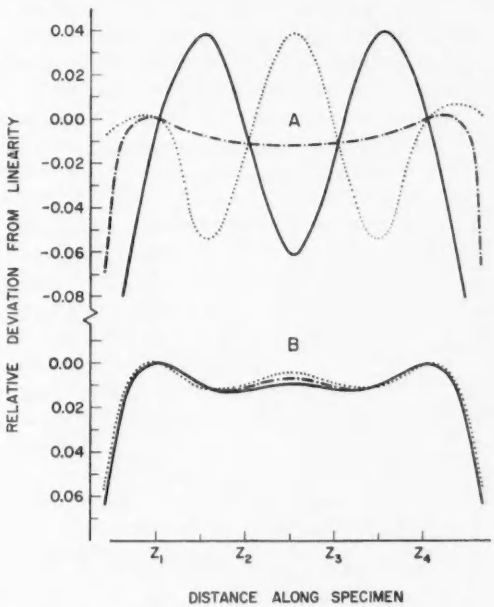

FIG. 5. Relative deviation from linearity of the temperature of the guard (curve A) and of the sample (curve B) for various allowable heater settings:
—— $\dot{Q}_3(b) = 0$; · · · $\dot{Q}_4(b) = 0$; – · – · $\dot{Q}_3(b) = \dot{Q}_4(b)$.

displacement between specimen and guard in the z-direction, temperature mismatches will occur the magnitude of which will depend on the heater settings. These will in turn result in errors in the experimental determination of conductivity. In the apparatus here considered, maximum error for any given specimen–guard displacement will occur when either $\dot{Q}_3(b)$ or $\dot{Q}_4(b)$ equals zero. It turns out that to a first approximation, the error in R due to a relative displacement of guard and specimen of δz, $E(\delta z)$, is the same in magnitude for $\dot{Q}_3(b) = 0$ as for $\dot{Q}_4(b) = 0$, but of different sign. Its magnitude is given by,

$$|E(\delta z)_{\max}| = E_0(k_1/k_2) \cdot \frac{T_0}{\Delta T} \cdot \frac{\delta z}{\Delta z}$$

where $\Delta z = z_n - z_{n-1}$, is the thermocouple separation.

$$E_0(1) = 0.65; \quad E_0(10) = 0.13; \quad \text{and} \quad E_0(100) = 0.01.$$

For any particular heater setting, the error in R will be somewhere between $+E(\delta z)_{\max}$ and $-E(\delta z)_{\max}$, depending on the ratio of $\dot{Q}_3(b)$ to $\dot{Q}_4(b)$. Figure 6 shows the possible error in R, $|E(\delta z)_{\max}|$, as a function of temperature, for dense alumina in insulating brick, as used by Francl and Kingery (1954), and dense alumina in powdered alumina insulation. Two curves are given for each case, one for a constant $\Delta T = 100°$ C, and one for a constant $\Delta T/T_0 = 0.1$. The relative displacement assumed, $\delta z/\Delta z$, was 1 mm in 25 mm, which is certainly very reasonable for a system constructed out of ceramics, unless very special precautions are taken during the lining up of specimen and guard. The errors shown in Fig. 6 are certainly not negligible at higher temperatures. They are, of course, the maximum possible due to the mis-

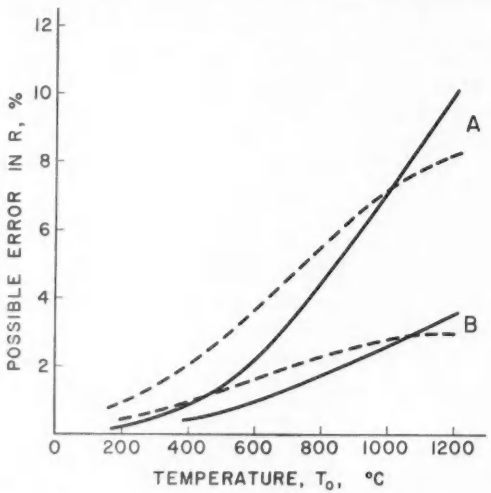

FIG. 6. Error in the comparative method of measuring thermal conductivity due to a misalignment of specimen and guard of 1 mm in 25 mm, for dense alumina in firebrick (curve A) and dense alumina in powdered alumina (curve B). —— $\Delta T = 100°$ C; – – – $\Delta T/T_0 = 0.1$.

alignment, and it is unlikely that in the actual experiment either $\dot{Q}_3(b)$ or $\dot{Q}_4(b)$ would be very close to zero. On the other hand, it should be remembered that dense alumina has a high thermal conductivity for a refractory substance, and for most other ceramics the maximum error would be much larger.

A very important feature of the error arising from the relative specimen–guard displacement, and one which is not obvious, is that it affects the specimen temperature intervals $T(a, z_1) - T(a, z_2)$ and $T(a, z_3) - T(a, z_4)$ in precisely the same way. This means that in a comparative measurement, where the end sections of the specimen are the standards and the middle the unknown, serious errors can arise in R, the ratio of the temperature gradient on the unknown to that on the standard, without any difference between the temperature gradients of the top and bottom standards. Thus, the agreement between the temperature gradients of the standards is no indication whatsoever of the errors in the determination of the unknown, contrary to popular opinion.

The error due to misalignment can be minimized by choice of heater settings. For each particular temperature, there is an optimum ratio of $\dot{Q}_3(b)$ to $\dot{Q}_4(b)$, for which the misalignment error is very small. This ratio can be calculated, and the experimental settings brought close to it. The reduction in uncertainty achieved this way can outweigh the reduction achieved by precision of alignment, which is difficult at high temperatures.

It may be mentioned here that radial displacements of sample relative to the guard are almost of no consequence. For the system here considered, the maximum change in temperature due to a relative radial displacement of 0.5 mm is 0.2% for $k_1/k_2 = 1$; 0.04% for $k_1/k_2 = 10$; and 0.003% for $k_1/k_2 = 100$. Furthermore, this maximum temperature change occurs at the midpoint between thermocouples, and is much smaller at the thermocouple sites.

A few remarks may be made here about the effects of the features in which the real systems differ from the mathematical one. By comparison of calculation with observation, the effect of the temperature variation of the thermal conductivity has been shown to have negligible effect on the temperature distribution. The outside boundary conditions are also not very important; they may change the magnitude of the temperature or its linear gradients, but will not seriously affect the temperature deviations from linearity. Some systems, like that of Francl and Kingery (1954), differ in two further aspects: their specimen is square in cross section, and its central regions have a smaller transverse dimension than its ends on which the heaters are wound. Placing a square specimen in a round guard is very much like the proverbial square peg in a round hole; it defies analysis, if not reason, and only vague statements can be made about its effects on the temperature distribution. There will, of course, be a component added to the sample temperature with a fourfold angular symmetry of the form

$$\sum_n A_n I_4(\alpha_n r) e^{4i\theta} \sin \alpha_n z.$$

It is likely that this component will have little effect on the temperature distribution for perfect alignment. For vertical misalignment, the effect on

the temperature distribution will be larger than for a cylindrical system with specimen diameter equal to the side of the square, but probably smaller than for a cylindrical system with specimen diameter equal to the diagonal of the square. Radial misalignment has very complex results, which may possibly still be negligible for perfect vertical alignment. The extension of the transverse dimensions at the specimen heaters is also very difficult to analyze accurately. However, relaxation calculations have been made for various ratios of heater diameter to specimen diameter, r_H/a. These showed that increasing the ratio from unity to two has very small effects on the specimen temperature distribution. For instance, for $k_1/k_2 = \infty$, it reduces the deviation from linearity of the temperature of the specimen mid-point from -0.016 to -0.011. Its effect on the guard temperature in the central region is negligible.

As a final example, a sample estimation of the uncertainty in the determination of conductivity in a Francl and Kingery type system is given. The temperature, T_0, is assumed to be 600° C, and the over-all temperature gradient, ΔT, 50° C. The thermocouple separation is 25 mm. The specimen and guard are made of alumina, and the insulation is brick, giving a k_1/k_2 of about 20. The uncertainty in the thermocouple separation is of the order of the thermocouple diameter, about 1%, and the uncertainty in the temperature measurement is assumed to be about 0.5%. The possible misalignment of guard and specimen is of the order of 1 mm, and the guard and specimen temperatures are matched to 1° C. The uncertainty in R, the ratio of the conductivity of the unknown to that of the standard, is then as follows:

uncertainty due to thermocouple separation	2%,
uncertainty due to temperature measurement	1%,
error due to deviation of temperature from linearity for perfect matching	1.5%,
uncertainty due to matching error	1.5%,
uncertainty due to possible displacement of guard to specimen	5%.

As these errors and uncertainties are not random, except for the matching error, the total uncertainty is of the order of the sum of the individual ones, about 11%. To that has to be added the uncertainty in the conductivity of the standard.

One can also estimate the expected difference between the temperature gradients of the top and bottom standard. These are:

uncertainty due to thermocouple separation	1.5%,
uncertainty due to temperature measurement	0.7%,
uncertainty due to matching error	1.0%,
error due to deviation of temperature from linearity for perfect matching	8.0%.

The last error always increases the gradient of the hotter standard with respect to the colder. One would then expect the hotter standard to have a gradient 5 to 10% larger than the colder one. This is roughly in agreement with the sample data published by Francl and Kingery (1954, p. 81). There, after due correction has been made for the temperature variation of con-

ductivity of the standard, the gradient of the hotter standard exceeds that of the colder one by 5% for the run with the Pb sample, and by 23% for the run with the MgO sample (if one assumes that the separation of the thermocouples on the standards was identical). The test temperature was about 200° C.

CONCLUSION

The disagreement among the results of thermal conductivity measurements reported in literature is large, particularly for ceramics. Part of the disagreement is real, due to variation of the specimen tested, and as such yields useful information about the substances studied. A significant part of the disagreement, however, is due to experimental error, consistently underestimated. A clear insight into the source and nature of the errors can be gained by exact mathematical analysis of the apparatus employed in the experiments. This is particularly important for errors which will affect the accuracy of the measurements without affecting their apparent precision.

The mathematical analysis of realistic experimental systems is usually within the limits of a desk calculator. In this paper, the method of analysis for systems using linear heat flow is indicated, and one particular system, that of Francl and Kingery (1954), is discussed in detail.

The analysis of the apparatus for comparative measurements of Francl and Kingery brings to light a number of interesting features. It shows that the specimen temperature deviates from linearity even for perfect matching of the guard and specimen temperature. It further shows that the system is very sensitive to the vertical alignment of guard and specimen, and that the agreement between the temperature gradients of the top and bottom standard gives no indication of the accuracy of the determination of conductivity of the unknown.

Evaluation of the uncertainty in a system like that of Francl and Kingery shows that its temperature range is very limited if the accuracy is to be kept within 10%. For alumina in insulating brick the upper temperature at which the uncertainty does not exceed 10% is about 600° C, and this upper limiting temperature rapidly decreases for the specimen whose conductivity is less than that of alumina.

REFERENCES

ADAMS, M. 1954. J. Am. Ceram. Soc. **37**, 74.
FRANCL, J. and KINGERY, W. D. 1954. J. Am. Ceram. Soc. **37**, 80.
LAUBITZ, M. J. 1959. Can. J. Phys. **37**, 1114.
——— 1961. Can. J. Phys. **39**, 951.

THE CRYSTAL STRUCTURE OF Bi_2Te_2Se[1]

J. A. BLAND[2] AND S. J. BASINSKI

ABSTRACT

The crystal structure of Bi_2Te_2Se has been determined by X-ray single crystal methods. The unit cell is trigonal, space group $R\bar{3}m$ with hexagonal cell edges $a = 4.28 \pm 0.02$ Å, $c = 29.86 \pm 0.10$ Å, and there are three formula units per unit cell. The structure is of the $C33$ type and a comparison is made with other $C33$ structures, Bi_2Se_3, Bi_2Te_3, and Bi_2Te_2S. An important common feature of these compounds is that the atom on the center of symmetry has a relatively large contact distance with each of its six Bi neighbors.

There is considerable interest in the relationship of the fundamental electronic properties, activation energies, and charge carrier mobilities of semiconducting compounds to the short-range order existing in those compounds (i.e., co-ordination numbers, bond lengths, and bond angles). Bi_2Te_2Se is a semiconductor belonging to a series of substances with the $C33$ type of structure, namely, Bi_2Se_3, Bi_2Te_3, Bi_2Te_2S, and it therefore appeared useful to determine its structure accurately so that a detailed comparison of interatomic distances in the binary and ternary compounds could be made.

Crystals with the chemical composition Bi_2Te_2Se were obtained from a homogeneous ingot prepared by melting the constituents together in a sealed tube. They were in the form of thin plates with a metallic luster and they could be easily deformed. A single crystal was obtained and accurately set on a Buerger camera with the aid of an optical goniometer. The usual X-ray method of setting the crystal proved to be difficult on account of the high density of reciprocal lattice nets parallel to (0001), the basal plane of the crystal, which resulted in higher layers being present on zero level photographs. These pictures showed, however, that [0001] is a trigonal axis. Reflections in the zero, second, and third reciprocal layers perpendicular to the $[01\bar{1}0]$ axis of the hexagonal cell were recorded using MoKα radiation and the systematic absences were found to be consistent with the trigonal space group $R\bar{3}m$; this choice was supported by the observation that the distributions of the intensities of the reflections in the three layers were identical. Indices of the reflections were assigned according to a hexagonal cell with dimensions $a = 4.28 \pm 0.02$ Å and $c = 29.86 \pm 0.10$ Å. The density calculated on the basis of three formula units per hexagonal cell is 7.93 g cm^{-3} and the density obtained by the displacement method on a small quantity of crystals was shown to be greater than 7.4 g cm^{-3}.

The structure was determined using the $000l$ reflections recorded on the zero level Buerger picture perpendicular to $[01\bar{1}0]$. The intensities were

[1]Manuscript received March 24, 1961.
Contribution from the Imperial Chemical Industries Limited, Akers Research Laboratories, The Frythe, Welwyn, Herts., England, and the Department of Mines and Technical Surveys, Ottawa, Canada.
[2]Now at Imperial Chemical Industries Limited, Plastics Division, Welwyn Garden City, Herts., England.

estimated by visual comparison with a standard scale and corrected for absorption of X rays in the specimen and for the Lorentz-polarization factor. The structure of tetradymite, Bi_2Te_2S (Harker 1934), was used as a starting point in the analysis, and refinement was carried out using F_0 and F_0-F_c one-dimensional syntheses along the c-axis of the hexagonal cell. A typical F_0 synthesis is given in Fig. 1. The positions of the 15 atoms in the hexagonal cell are

$$(000, \tfrac{122}{333}, \tfrac{211}{333})+,$$
$$\text{Bi} \pm 00v,$$
$$\text{Te} \pm 00u,$$
$$\text{Se} \quad 000,$$

where $v = 0.396_1 \pm 0.015$ and $u = 0.211_7 \pm 0.045$. The limits of error were estimated from the gradients at the atomic positions on the final difference

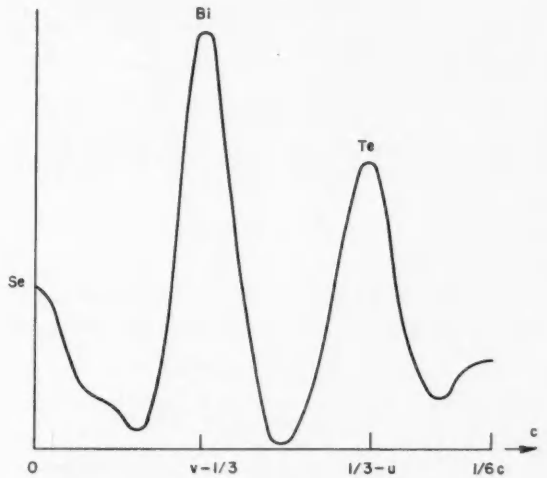

FIG. 1. Bi_2Te_2Se. One-dimensional F_0 synthesis using 000l reflections.

synthesis. In the calculation of structure factors, a temperature factor of 0.7 A^{-2} was assigned to each atom; values of F_0 scaled for comparison with F_c are given in Table I.

Bi_2Te_2Se is isomorphous with tetradymite, Bi_2Te_2S, and may be considered as a layer structure in which each atom is co-ordinated by six neighbors; Bi is linked to three Se atoms and to three Te atoms, and Se is linked to six Bi atoms. In Table II(a), interatomic distances are compared with corresponding distances in other structures of the series, Bi_2Se_3 and Bi_2T3_3 (Semiletov 1956) and Bi_2Te_2S (Harker 1934). Although the accuracy of these structures is not known and detailed comparison is thereby made difficult, a

TABLE I

Comparison of F_0 and F_c values of $000l$ reflections for Bi_2Te_2Se

l	F_0	F_c
3		
6	$\overline{33}$	$\overline{45}$
9	$\overline{15}$	$\overline{17}$
12	$\overline{26}$	$\overline{27}$
15	73	84
18	$\overline{66}$	$\overline{62}$
21	$\overline{43}$	$\overline{38}$
24	$\overline{18}$	$\overline{15}$
27	$\overline{12}$	$\overline{16}$
30	19	19
33	$\overline{33}$	$\overline{61}$
36	$\overline{6}$	$\overline{6}$

TABLE II(a)

Interatomic distances (Å) in $C33$-type compounds

Structure No.								Normal valence radius sum	
I Bi_2Se_3		II Bi_2Te_3		III Bi_2Te_2S		IV Bi_2Te_2Se			
$Bi–Se_0$	3.05	$Bi–Te_0$	3.24	Bi–S	3.06	Bi–Se	3.10±0.03	Bi–S	2.55
Bi–Se	2.99	$Bi–Te_1$	3.04	$Bi–Te_1$	3.13	Bi–Te	3.03±0.05	Bi–Se	2.68
$Se_1–Se_1$	3.31	$Te_1–Te_1$	3.73	$Te_1–Te_1$	3.70	Te–Te	3.65±0.06	Bi–Te	2.88
								Se–Se	2.34
								Te–Te	2.74

feature which emerges from the study is that in each compound, the atom at the origin has a relatively large contact distance with each of its six Bi neighbors. This is apparent in Table II(b) where the Bi–M distances, with

TABLE II(b)

Comparison of interatomic distances (Å), Bi–M, in $C33$-type compounds tabulated as $Bi–M_0$ and $Bi–M_1$

M	M at origin, M_0	M in general position, M_1
S	3.06^{III}	
Se	3.05^{I} 3.10^{IV}	2.99^{I}
Te	3.24^{II}	3.04^{II} 3.13^{III} 3.03^{IV}

The superscripts refer to the four structures in Table II(a).

M representing S, Se, and Te, are set out in two columns, the first showing distances involving M at the origin, M_0, and the second showing distances with M in the general position M_1. The effect is most marked in Bi_2Te_3 where $Bi–Te_0$ is 3.24 Å, which is considerably greater than the largest $Bi–Te_1$ distance of 3.13 Å in Bi_2Te_2S. Similarly the $Bi–Se_0$ distances of 3.05 Å and 3.10 Å in Bi_2Se_3 and Bi_2Te_2Se are probably significantly larger than the $Bi–Se_1$ distance of 2.99 Å in Bi_2Se_3. It is also probable that the $Bi–S_0$ distance of

3.06 Å in Bi_2Te_2S is relatively large because it has the same value as the mean Bi–Se distance in the other structures; the covalent radii of S and Se are 1.04 Å and 1.17 Å (Wells 1950) so that normally the Bi–S distance should be shorter than the Bi–Se distance, Table II(*a*). The relatively large size of the atom at the origin is also clear from a scrutiny of Bi_2Te_2Se. In this structure the Bi–Se_0 distance is just significantly longer than the Bi–Te_1 distance; the inequality is in the opposite direction to that expected from the values of the covalent radius sums given in the final column of Table II(*a*).

We wish to thank Dr. E. Mooser and Dr. W. B. Pearson of the National Research Council of Canada, Ottawa, for suggesting the problem and providing the crystals. We also thank Mr. R. C. McAdam of the Department of Mines and Technical Surveys, Ottawa, for the chemical analyses.

REFERENCES

HARKER, D. 1934. Z. Krist. A, **89**, 175.
SEMILETOV, S. A. 1956. Kristallografiya, **10**, 76.
WELLS, A. F. 1950. Structural inorganic chemistry (Oxford University Press).

WAVES IN A RAREFIED IONIZED GAS PROPAGATED TRANSVERSE TO AN EXTERNAL MAGNETIC FIELD[1]

TOMIYA WATANABE[2]

ABSTRACT

Waves being propagated in a rarefied and fully ionized gas and transverse to an external magnetic field have been studied, particularly hydromagnetic waves. Three modes of waves, in which the perturbed magnetic field is parallel to the external magnetic field, are found to be propagated. In a high-frequency limit, they tend to electromagnetic waves, electron sound waves, and ion sound waves. In the condition that the Alfvén velocity is greater than the ion sound velocity but smaller than the light velocity, the last mode tends to a hydromagnetic wave in the low-frequency limit. The other two modes of waves can be propagated only at frequencies higher than the critical frequencies, both of which almost equal the electron plasma frequency. The condition that hydromagnetic waves should be attenuated severely due to collisions between electrons and ions has been derived.

1. INTRODUCTION

Waves propagated in a uniform conducting fluid under an external uniform magnetic field have been studied by many authors. For instance, we can mention van de Hulst's work (1951), which employed the Navier–Stokes equation but with an additional term representing the ampère force and the ohmic law of electric conduction in the case of moving media:

$$\mathbf{j}/\sigma = \mathbf{E} + \frac{1}{c}\mathbf{u}\wedge\mathbf{H}, \tag{1.1}$$

where the meanings of notations are as follows: **E**, electric field; **H**, magnetic field; **j**, density of electric currents; **u**, velocity of the fluid; and σ, electric conductivity. He reaffirmed the occurrence of hydromagnetic waves discovered by Alfvén (1950), which in an extremely conducting ($\sigma \to \infty$) and non-viscous fluid can be propagated along the external magnetic field with the so-called Alfvén velocity defined by

$$V_A = \frac{H_0}{\sqrt{(4\pi\rho)}},$$

where H_0 is the intensity of the external magnetic field and ρ is the density of the fluid. One of van de Hulst's important and new contributions is that waves can be propagated not only along the external magnetic field but also transverse to it, if the fluid is compressible. In that case, the propagation velocity V is given by

$$V = \sqrt{(V_A^2 + C_s^2)} \tag{1.3}$$

where C_s is the sound velocity of the fluid.

[1]Manuscript received February 6, 1961.
Contribution from the Department of Physics, University of Maryland, College Park, Maryland, U.S.A.

[2]On leave from the Geophysical Institute, Faculty of Science, Tohoku University, Sendai, Japan. Now at the Department of Physics, University of British Columbia, Vancouver 8, B.C.

In many interesting cases, the medium in which hydromagnetic waves should appear is a gas, especially a rarefied gas, which is ionized fully or partially. Ionized gases are good conducting media, and thus, hydromagnetic waves may be expected to occur in them. In that case, however, it is not clear a priori that the law of electric conduction (1.1) would still hold. This is an experimental law concerning metallic substances. The equation of motion is also a problem. Generally, an ionized gas is in a so-called plasma state. Namely, it consists of electrons and ions, number densities of which are equal to each other, in order to avoid the dispersion due to the electrostatic repulsion. Since the ion mass is much greater than the electron mass, the ion gas does not necessarily move with the electron gas. We cannot describe such a situation with only one equation of motion, that is, the Navier–Stokes equation with an additional term due to the ampère force, but we need two equations of motion, one for the ion gas and the other for the electron gas.

These problems must be reviewed from a microscopic point of view. Aström (1951), Schlüter (1952), and Ferraro (1955) treated the problem of waves propagated along the external magnetic field in this manner. Aström also studied waves propagated oblique to the external magnetic field as well as normal to it. But, he did not take into account the gas pressure, which may be of importance in oblique and, especially, normal propagation. Piddington's work (1955) took into consideration the pressure of the electron gas, but he omitted both motion and pressure of the ion gas. In this paper, we shall try to study the problem, taking both motion and pressure of the ion gas into consideration, but we will restrict the problem to the case of normal propagation.

2. FUNDAMENTAL EQUATION

As mentioned above, the first problem is to formulate the equations of motion and of electric conduction rigorously. In order to do so, it may be best to start from the Boltzmann equation. Let us consider waves propagating in a fully ionized gas, which consists of electrons and ions. The mass of an ion, m_i, is assumed much heavier than that of an electron, m_e. In an undisturbed state, that is, in a state where no waves appear, the number density of electrons, N_e, is equal to that of ions, N_i, and it is expressed by N_p. The electric charge of an ion is represented by e (>0). Accordingly, the electronic charge is $-e$. We shall employ the Gaussian system of units of electromagnetic quantities throughout the paper.

Under these conditions, one can derive the equation of the electron gas from the Boltzmann equation as follows (Spitzer 1956):

$$(2.1)\quad \rho_e\left(\frac{\partial \mathbf{u}_e}{\partial t}+(\mathbf{u}_e\cdot\nabla)\mathbf{u}_e\right) = -N_e e\left(\mathbf{E}+\frac{1}{c}\,\mathbf{u}_e\wedge\mathbf{H}\right)-\nabla_e\psi-\rho_e\nabla\phi+\mathbf{P}_{el}.$$

$\rho_e = N_e m_e$ is the mass density of the electron gas. The permeability is assumed equal to 1. ϕ is the potential of the external and non-electromagnetic force per unit mass such as the gravity force, which we shall omit in this paper. $\mathbf{u}_e$ is the mean velocity of electrons in a volume element, ΔV, and is given by

$$\mathbf{u}_e = \frac{1}{N_e \Delta V} \sum \mathbf{v}_e \tag{2.2}$$

where $\mathbf{v}_e$'s are velocities of individual electrons. The quantity ψ_e is the stress tensor, the ψ_{lm} component is given by

$$\psi_{lm} = \frac{m_e}{\Delta V} \sum (\mathbf{v}_e - \mathbf{u}_e)_l (\mathbf{v}_e - \mathbf{u}_e)_m \tag{2.3}$$

the summation extending over the volume element.

In the simplest case that the distribution of the random velocities $\mathbf{v}_e - \mathbf{u}_e$ is isotropic, ψ_{lm} vanishes unless l equals m, and the three diagonal components ψ_{xx}, ψ_{yy}, ψ_{zz} are all equal to each other and to the scalar pressure p (Spitzer 1956). In this situation, we have

$$\nabla \psi \rightarrow \nabla p. \tag{2.4}$$

We assume this simplification throughout the paper. According to Spitzer (1956), this replacement of the stress tensor by a scalar pressure means we ignore the damping in wave propagations discovered by Landau (1946), and thus, the following analysis should be taken only as a model case neglecting this kind of damping.

The quantity $\mathbf{P}_{ei}$ is the total momentum transferred to the electrons per unit volume per unit time by collisions with ions. Schlüter (1950, 1951) has assumed the following form for this quantity,

$$P_{ei} = -N_e N_i \alpha_{ei} (\mathbf{u}_e - \mathbf{u}_i) \tag{2.5}$$

where

$$\alpha_{ei} = \frac{\nu_{ei}}{N_i} \frac{m_e m_i}{m_e + m_i} \tag{2.6}$$

and $\mathbf{u}_i$ is the mean velocity of ions. ν_{ei} is the collision frequency of an electron with ions.

Under the two assumptions concerning the stress tensor ψ_e and the quantity $\mathbf{P}_{ei}$, the equation of motion of the electron gas becomes

$$\rho_e \left(\frac{\partial \mathbf{u}_e}{\partial t} + (\mathbf{u}_e \cdot \nabla) \mathbf{u}_e \right) + N_e N_i \alpha_{ei} (\mathbf{u}_e - \mathbf{u}_i) = -\nabla p_e - e N_e \left(\mathbf{E} + \frac{1}{c} \mathbf{u}_e \wedge \mathbf{H} \right). \tag{2.7}$$

p_e may be considered as the pressure of the electron gas. It is to be noted that this equation is the same as the macroscopic one except for the addition of the term due to the Lorentz force and that due to collisions. The equation of the ion gas is similarly given by

$$\rho_i \left(\frac{\partial \mathbf{u}_i}{\partial t} + (\mathbf{u}_i \cdot \nabla) \mathbf{u}_i \right) + N_i N_e \alpha_{ie} (\mathbf{u}_i - \mathbf{u}_e) = -\nabla p_i + e N_i \left(\mathbf{E} + \frac{1}{c} \mathbf{u}_i \wedge \mathbf{H} \right) \tag{2.8}$$

where

$$\alpha_{ie} = \frac{\nu_{ie}}{N_e} \frac{m_i m_e}{m_i + m_e}. \tag{2.9}$$

Formulation of equations of motion of the electron gas and the ion gas into eqs. (2.7) and (2.8) tells us that the behavior of a fully ionized gas can be pictured as that of two kinds of fluids, electronic and ionic, with a mutual interaction. This "two fluid" model is the standpoint on which Schlüter (1952) developed his theory. Irrespective of its macroscopic appearance, it has microscopic bases except for the assumptions about the stress tensor and the force due to collisions.

In order to consider waves of small amplitude we linearize both the above equations, and then we have

$$\rho_{e0}\frac{\partial \mathbf{u}_e}{\partial t}+N_p^2\alpha_{ei}(\mathbf{u}_e-\mathbf{u}_i) = -\nabla p_e-eN_p\left(\mathbf{E}+\frac{1}{c}\mathbf{u}_e\wedge\mathbf{H}_0\right), \tag{2.10}$$

$$\rho_{i0}\frac{\partial \mathbf{u}_i}{\partial t}+N_p^2\alpha_{ie}(\mathbf{u}_i-\mathbf{u}_e) = -\nabla p_i+eN_p\left(\mathbf{E}+\frac{1}{c}\mathbf{u}_i\wedge\mathbf{H}_0\right). \tag{2.11}$$

ρ_{e0} and ρ_{i0} are the mean densities of the electron gas and the ion gas respectively.

Adding the above two equations, we have the equation of motion of the whole gas:

$$\rho_0\frac{\partial \mathbf{u}_p}{\partial t} = -\nabla p_p+\frac{1}{c}\mathbf{j}\wedge\mathbf{H}_0, \tag{2.12}$$

where it may be noticed that $\nu_{ei}=\nu_{ie}$ and $\alpha_{ei}=\alpha_{ie}$. The meanings of the notations are as follows:

(2.13) $\rho_0=\rho_{e0}+\rho_{i0}\simeq\rho_{i0}$, the total density of the ionized gas,

(2.14) $\mathbf{u}_p=(\rho_{e0}\mathbf{u}_e+\rho_{i0}\mathbf{u}_i)/\rho_0$, the mean velocity of the mass center of a volume element,

(2.15) $p_p=p_e+p_i$, the total pressure of the ionized gas,

(2.16) $\mathbf{j}=eN_p(\mathbf{u}_i-\mathbf{u}_e)$, the density of electric currents,

$\mathbf{H}_0$, the intensity of external magnetic field.

As a result of the above definitions, we have

$$\mathbf{u}_e=\mathbf{u}_p-\frac{1}{eN_p}\frac{\rho_{i0}}{\rho_0}\mathbf{j}, \tag{2.17}$$

$$\mathbf{u}_i=\mathbf{u}_p+\frac{1}{eN_p}\frac{\rho_{e0}}{\rho_0}\mathbf{j}. \tag{2.18}$$

Multiplying eq. (2.10) by $-\rho_{i0}$ and eq. (2.11) by ρ_{e0} and then adding the two equations, we have the following equation after some manipulation:

$$\frac{4\pi}{\omega_p^2}\frac{\partial \mathbf{j}}{\partial t}+\frac{\mathbf{j}}{\sigma} = \mathbf{E}+\frac{1}{c}\mathbf{u}_p\wedge\mathbf{H}_0-\frac{1}{eN_p}\frac{\rho_{i0}-\rho_{e0}}{\rho_0}\mathbf{j}\wedge\mathbf{H}_0 \tag{2.19}$$

$$+\frac{1}{eN_p\rho_0}(\rho_{i0}\nabla p_e-\rho_{e0}\nabla p_i)$$

where ω_p is the electron plasma frequency;

$$\omega_p^2 = 4\pi e^2 \frac{\rho_0}{m_i m_e} \cong \frac{4\pi N_p e^2}{m_e} \tag{2.20}$$

and

$$\frac{1}{\sigma} = \frac{\alpha_{el}}{e^2} \cong \frac{m_e}{N_p e^2} \nu_{el}. \tag{2.21}$$

Equation (2.19) is the generalized ohmic law to be employed instead of (1.1). It is written as follows to a good approximation:

$$\frac{4\pi}{\omega_p^2}\left(\frac{\partial \mathbf{j}}{\partial t}+\nu_{el}\mathbf{j}\right) = \mathbf{E}+\frac{1}{c}\mathbf{u}_p \wedge \mathbf{H}_0-\frac{1}{eN_p c}\mathbf{j} \wedge \mathbf{H}_0+\frac{1}{eN_p c}(\rho_{10}\nabla p_e-\rho_{e0}\nabla p_1). \tag{2.22}$$

This equation, lacking the last term, is used by Schlüter (1952) in his study of waves propagating along an external magnetic field.

In the steady state, eq. (2.22) reduces to

$$\mathbf{j} = \sigma \mathbf{E}'_{\parallel}+\sigma_\perp \mathbf{E}'_\perp+\sigma_H\left(\frac{\mathbf{H}_0}{H_0} \wedge \mathbf{E}'_\perp\right), \tag{2.23}$$

where $\mathbf{E}'$ is the electric field observed from the system moving with the ionized gas:

$$\mathbf{E}' = \mathbf{E}+\frac{1}{c}\mathbf{u}_p \wedge \mathbf{H}_0. \tag{2.24}$$

$\sigma_\perp$ and σ_H are Pedersen and Hall conductivities defined by

$$\sigma_\perp = \sigma \frac{\nu_{el}^2}{\omega_e^2+\nu_{el}^2}, \tag{2.25}$$

$$\sigma_H = \sigma \frac{\omega_e \nu_{el}}{\omega_e^2+\nu_{el}^2}. \tag{2.26}$$

We can easily prove that

$$\sigma = \sigma_\perp+\frac{\sigma_H^2}{\sigma_\perp}, \tag{2.27}$$

where σ, given by eq. (2.21) may be called the total conductivity. Equation (1.1) is the first approximation. Equation (2.23) is the next approximation, extending the ohmic law (1.1) to an anisotropic case, and it has often been used as one of the fundamental equations. However, it is inadequate for the treatment of high-frequency waves since it imposes some drastic restrictions (as seen from the above derivations), which we shall avoid in the following treatment.

The other fundamental equations are the equations of continuity, which can be derived rigorously from the Boltzmann equation,

$$\frac{\partial \rho_e}{\partial t}+\text{div}\,(\rho_e \mathbf{u}_e) = 0, \tag{2.28}$$

$$\frac{\partial \rho_1}{\partial t}+\operatorname{div}(\rho_1 \mathbf{u}_1)=0. \tag{2.29}$$

In linear approximations they can be written as follows:

$$\frac{\partial \rho_e}{\partial t}+\rho_{e0}\operatorname{div}\mathbf{u}_e=0, \tag{2.30}$$

$$\frac{\partial \rho_1}{\partial t}+\rho_{10}\operatorname{div}\mathbf{u}_1=0. \tag{2.31}$$

3. DERIVATION OF DISPERSION RELATION

We shall consider plane waves, in which wave quantities of the first degree may be assumed to depend on time and space through only one factor,

$$e^{i(\omega t+\mathbf{k}\cdot\mathbf{r})}. \tag{3.1}$$

In that case, differential operators for wave quantities of the first degree can be replaced by algebraic operators as follows:

$$\left.\begin{array}{c}\partial/\partial t \rightarrow i\omega \\ \nabla\varphi \rightarrow i\mathbf{k}\varphi \\ \operatorname{div}\mathbf{A} \rightarrow i(\mathbf{k}\cdot\mathbf{A}) \\ \operatorname{rot}\mathbf{A} \rightarrow i(\mathbf{k}\wedge\mathbf{A})\end{array}\right\}. \tag{3.2}$$

The state of the electron gas is assumed to change adiabatically, and thus, we have

$$\nabla p_e = C_e^2 \nabla \rho_e. \tag{3.3}$$

C_e is the sound velocity of the electron gas and is given by

$$C_e^2 = \gamma_e \frac{p_{e0}}{\rho_{e0}} = \gamma_e \frac{\kappa T_e}{m_e}, \tag{3.4}$$

where γ_e, κ, and T_e are the ratio of specific heat capacities, the Boltzmann constant, and the temperature of the electron gas. The similar assumption is made for the ion gas, and thus we have

$$\nabla p_1 = C_1^2 \nabla \rho_1. \tag{3.5}$$

C_1 is the sound velocity of the ion gas;

$$C_1^2 = \gamma_1 \frac{\kappa T_1}{m_1}. \tag{3.6}$$

We assume that the temperatures of both gases are equal to each other and that $\gamma_e = \gamma_1$. Then, we have

$$\frac{C_e^2}{C_1^2} = \frac{m_1}{m_e} = \frac{\rho_{10}}{\rho_{e0}}. \tag{3.7}$$

Making use of the relations (3.3), (3.5), (2.30), (2.31), (2.17), (2.18), (3.7), and (3.2), we have

$$\nabla p = \nabla p_e + \nabla p_1 = -i\frac{\rho_0 C_1^2}{\omega}\left\{2(\mathbf{k}\cdot\mathbf{u}_p)\mathbf{k} - \frac{1}{eN_p}(\mathbf{k}\cdot\mathbf{j})\mathbf{k}\right\}. \tag{3.8}$$

Similarly we have

$$\frac{1}{eN_p}\frac{1}{\rho_0}(\rho_{10}\nabla p_e - \rho_{e0}\nabla p_1) = -i\frac{1}{eN_p}\frac{\rho_0 C_1^2}{\omega}(\mathbf{k}\cdot\mathbf{u}_p)\mathbf{k} + i\frac{1}{(eN_p)^2}\frac{\rho_0 C_1^2}{\omega}(\mathbf{k}\cdot\mathbf{j})\mathbf{k}. \tag{3.9}$$

Therefore, the fundamental equations (2.12) and (2.22) become

$$i\omega\rho_0\mathbf{u}_p = \frac{1}{c}\mathbf{j}\wedge\mathbf{H}_0 + i\frac{C_1^2\rho_0}{\omega}(\mathbf{k}\cdot\mathbf{u}_p)\mathbf{k} - i\frac{C_1^2\rho_0}{\omega}\frac{1}{eN_p}(\mathbf{k}\cdot\mathbf{j})\mathbf{k}, \tag{3.10}$$

$$\frac{4\pi}{\omega_p^2}(i\omega+\nu_{el})\mathbf{j} = \mathbf{E} + \frac{1}{c}\mathbf{u}_p\wedge\mathbf{H}_0 - \frac{4\pi}{\omega_p^2}\omega_e\wedge\frac{\mathbf{H}_0}{H_0} - i\frac{1}{eN_p}\frac{\rho_0 C_1^2}{\omega}(\mathbf{k}\cdot\mathbf{u}_p)\mathbf{k} + i\frac{1}{(eN_p)^2}\frac{\rho_0 C_1^2}{\omega}(\mathbf{k}\cdot\mathbf{j})\mathbf{k}. \tag{3.11}$$

In the following, we shall consider plane waves propagated in the x direction. The gas is assumed so rarefied that collisions are negligible. The external magnetic field is taken along the z-axis:

$$\mathbf{H}_0\colon\ H_x = 0, \qquad H_y = 0, \qquad H_z = H_0 = \text{const.} \tag{3.12}$$

Equations (3.10) and (3.11) tell us that waves of the mode in which the electric field and the currents are parallel to the external magnetic field (z-axis) can be found without any motion of the ionized gas ($u_{pz} = 0$). Waves in this case are electromagnetic waves, for which the dispersion relation is given by

$$\frac{c^2}{V^2} = 1 - \frac{\omega_p^2}{\omega^2}, \tag{3.13}$$

where V, the phase velocity, is, of course, given by

$$V = \omega/k. \tag{3.14}$$

The above dispersion relation is familiar in propagation of electromagnetic waves in the ionosphere.

Taking the x and y components of eq. (3.10), we have

$$u_{px} = -\frac{1}{eN_p}\frac{1}{1-2(C_1^2/V^2)}\left(\frac{C_1^2}{V^2}j_x + i\frac{\omega_1}{\omega}j_y\right), \tag{3.15}$$

$$u_{py} = i\frac{1}{eN_p}\frac{\omega_1}{\omega}j_x, \tag{3.16}$$

where ω_1 is the ion gyro-frequency defined by

$$\omega_1 = \frac{eH_0}{m_1 c}. \tag{3.17}$$

The electron gyro-frequency is given by, of course,

$$\omega_e = \frac{eH_0}{m_e c} \tag{3.18}$$

and thus, we have

$$\frac{\omega_e}{\omega_1} = \frac{m_1}{m_e}. \tag{3.19}$$

On the other hand, eq. (3.11) gives us

$$i\frac{4\pi}{\omega_p^2}\omega j_x = E_x + \frac{H_0}{c}u_{py} - \frac{4\pi}{\omega_p^2}\omega_e j_y - i\frac{1}{eN_p}\frac{\rho_0 C_1^2}{\omega}k^2 u_{px} + i\frac{1}{(eN_p)^2}\frac{\rho_0 C_1^2}{\omega}k^2 j_x, \tag{3.20}$$

$$i\frac{4\pi}{\omega_p^2}\omega j_y = E_y - \frac{H_0}{c}u_{px} + \frac{4\pi}{\omega_p^2}\omega_e j_x. \tag{3.21}$$

From Maxwell's fundamental equations, we can find the electric field **E**, and the perturbed magnetic field, **h**, in this mode as follows:

$$\left.\begin{aligned} E_x &= i\frac{4\pi}{\omega}j_x, \\ E_y &= i\frac{4\pi/\omega}{1-(c^2/V^2)}j_y, \\ E_z &= 0, \end{aligned}\right\} \tag{3.22}$$

$$h_x = h_y = 0, \tag{3.23}$$

$$h_z = -\frac{c}{V}E_y.$$

Substituting eqs. (3.23), (3.24), (3.16), and (3.17) into eqs. (3.21) and (3.22), and then making some rearrangements, we have

$$\left(1+\frac{\omega_1\omega_e}{\omega_p^2}+\frac{\omega^2}{\omega_p^2}\frac{C_e^2}{V^2}\frac{1-(C_1^2/V^2)}{1-2(C_1^2/V^2)}-\frac{\omega^2}{\omega_p^2}\right)j_x + i\frac{\omega_e\omega}{\omega_p^2}\frac{1-(C_1^2/V^2)}{1-2(C_1^2/V^2)}j_y = 0, \tag{3.24}$$

$$\frac{\omega_e\omega}{\omega_p^2}\frac{1-(C_1^2/V^2)}{1-2(C_1^2/V^2)}j_x - i\left(\frac{\omega^2}{\omega_p^2}-\frac{1}{1-(c^2/V^2)}-\frac{\omega_1\omega_e}{\omega_p^2}\frac{1}{1-2(C_1^2/V^2)}\right)j_y = 0. \tag{3.25}$$

The determinant formed from the coefficients of the two equations must be equal to zero, in order that j_x and j_y may not be zero identically:

$$\left(\frac{\omega}{\omega_p}\right)^2\left(\frac{\omega_e}{\omega_p}\right)^2\left(1+\frac{(C_1^2/V^2)}{1-2(C_1^2/V^2)}\right)-\left(\frac{\omega^2}{\omega_p^2}-1-\frac{\omega_1\omega_e}{\omega_p^2}-\frac{\omega^2}{\omega_p^2}\frac{C_e^2}{V^2}\frac{1-(C_1^2/V^2)}{1-2(C_1^2/V^2)}\right)\left(\frac{\omega^2}{\omega_p^2}-\frac{1}{1-(c^2/V^2)}-\frac{\omega_1\omega_e}{\omega_p^2}\frac{1}{1-2(C_1^2/V^2)}\right) = 0, \tag{3.26}$$

which is the dispersion relation.

Put

$$x = \left(\frac{C_1}{V}\right)^2, \qquad \sigma = \left(\frac{\omega}{\omega_p}\right)^2 \tag{3.27}$$

and

$$\lambda = \left(\frac{C_1}{c}\right)^2, \qquad \mu = \frac{m_1}{m_e}, \qquad \rho = \frac{\omega_1\omega_e}{\omega_p^2} = \frac{V_A^2}{c^2}, \qquad \gamma = \frac{\omega_e^2}{\omega_p^2}. \tag{3.28}$$

Then we have

$$\frac{c^2}{V^2} = \frac{C_1^2}{V^2}\frac{1}{\lambda} = \frac{x}{\lambda} \tag{3.29}$$

and

$$\gamma = \rho\mu. \tag{3.30}$$

Using these abbreviations, the dispersion relation is rewritten as follows:

$$F(x) \equiv A_0(\sigma)x^3 - A_1(\sigma)x^2 + A_2(\sigma)x - \lambda A_3(\sigma) = 0, \tag{3.31}$$

where

$$\left.\begin{aligned} A_0(\sigma) &= \mu\sigma^2, \\ A_1(\sigma) &= \sigma[\{(\mu+2)+\lambda\mu\}\sigma - \{(2+\gamma+2\rho)+\lambda\mu\}], \\ A_2(\sigma) &= \{1+\lambda(\mu+2)\}\sigma^2 - \{(1+\gamma+2\rho)+\lambda(\mu+4+\gamma+2\rho)\}\sigma \\ &\qquad + (1+\rho)(\rho+2\lambda), \\ A_3(\sigma) &= \sigma^2 - (2+\gamma+2\rho)\sigma + (1+\rho)^2. \end{aligned}\right\} \tag{3.32}$$

4. WAVES IN THE ABSENCE OF EXTERNAL MAGNETIC FIELD

In this case, the dispersion relation (3.31) is reduced to

$$[\sigma x - \lambda(\sigma-1)][\mu\sigma x^2 - \{(\mu+2)\sigma - 2\}x + (\sigma-1)] = 0. \tag{4.1}$$

The first mode of waves, for which the dispersion relation is given by

$$x = \lambda\left(1 - \frac{1}{\sigma}\right) \tag{4.2}$$

are electromagnetic (EM) waves. One can easily find that eq. (4.2) is identical with eq. (3.9). Two other modes of waves are given by

$$x = \frac{1}{2} + \frac{1}{\mu}\left(1 - \frac{1}{\sigma}\right) \pm \sqrt{\frac{1}{\mu^2}\left(1 - \frac{1}{\sigma}\right)^2 + \frac{1}{4}}. \tag{4.3}$$

The dispersion relations are illustrated in Fig. 1.

Waves of (4.3) with + sign have the following properties: that $x \to \sim 1$, as $\sigma \to \infty$ $(\omega \gg \omega_p)$, that is, waves tend to sound waves in the ion gas in a high-frequency limit, and that $x \to \frac{1}{2}$, as $\sigma \to 0$ $(\omega \ll \omega_p)$, that is, waves in this case are sound waves in the whole ionized gas including electrons and ions. Waves, where $x = \frac{1}{2}$, or

$$V = \sqrt{2}C_1 \tag{4.4}$$

may be considered as sound waves in the whole ionized gas. In a low-frequency limit, the differential velocity between the ions and the electrons may be small, and thus, the pressures of both gases, which are equal to each other under

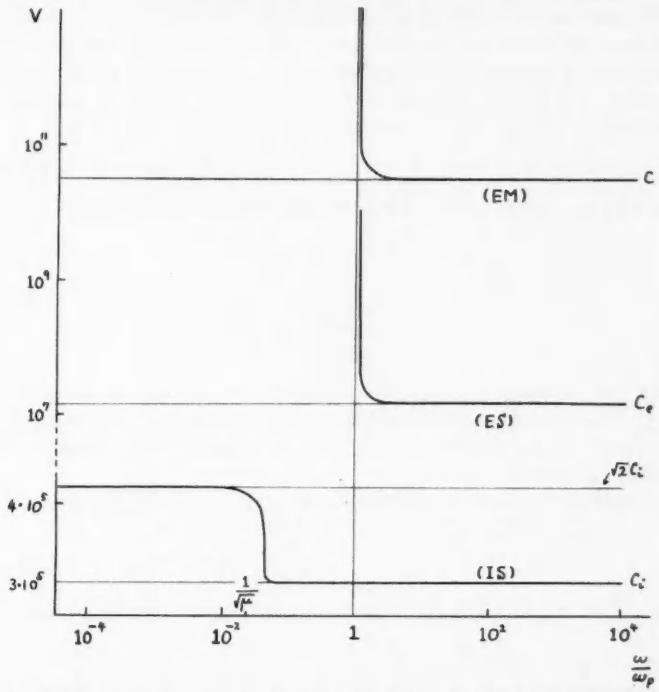

FIG. 1. The dispersion curves of waves propagated in a fully ionized hydrogen gas. Ordinates: propagation velocity in cm/sec. Abscissae: wave frequencies in units of the plasma frequency. No external magnetic field applied. C_i and C_e are the propagation velocities of the sound waves in the ion and electron gases. $C_i = 3.10^6$ cm/sec is taken as an example. The electron temperature is assumed to be equal to the ion temperature. c is the light velocity, equal to 3.10^{10} cm/sec. μ is the ratio of the ion mass to the electron mass. It may be noticed that the propagation velocity of the IS wave changes abruptly at a frequency $\omega = \omega_p/\sqrt{\mu}$.

our assumption, would contribute co-operatively to wave propagation. The mass density of the whole gas is almost equal to that of the ion gas, and thus, the square of the sound velocity of the whole gas becomes twice that of the ion gas. It may be noticed that the propagation velocity falls off rapidly from $\sqrt{2}C_i$ to C_i around $\sigma \sim 1/\mu$, that is, $\omega \sim \omega_p/\sqrt{\mu}$. At high frequencies, the wave velocity tends to that of the ion sound velocity, as stated already. This may be due to the fact that the ions easily move independently of the electrons at high frequencies. One can name this mode of waves ion sound (IS) waves.

Waves of eq. (4.3) with $-$ sign have following properties: $x \to 1/\mu$, as $\sigma \to \infty$, that is, $V \to \sim\sqrt{\mu}C_i = C_e$. Waves in this case may be called electron sound (ES) waves. On the other hand, x becomes negative in the region $\sigma < 1$ ($\omega < \omega_p$). Viewed from the definition of x, there is no wave propagation in this frequency range. In the frequency range $\sigma \geq 1$, the dispersion relation for ES waves is approximated well by

$$\omega^2 = \omega_p^2 + C_e^2 k^2 \tag{4.5}$$

which is a well-known form. If the gas temperature is zero ($C_e = 0$), we have non-propagating oscillations, with frequency equal to the electron plasma frequency. Such oscillations are called plasma oscillations. Even though the temperature is not zero, a similar situation appears when the wavelength is so long that the frequency becomes independent of the wavelength.

5. WAVES IN THE PRESENCE OF AN EXTERNAL MAGNETIC FIELD

In a high-frequency limit, the dispersion relation (3.32) gives us

$$x = \lambda, \tag{5.1}$$

$$x = \frac{(\mu+2) \pm \sqrt{\mu^2+4}}{2\mu} \cong \begin{cases} 1, \\ \dfrac{1}{\mu}. \end{cases} \tag{5.2}$$

The first corresponds to electromagnetic waves propagated with the light velocity. The second means sound waves in the ion gas and the third also sound waves but in the electron gas. The situation is very similar to that in the former section.

In a low-frequency limit, the dispersion relation (3.32) gives us

$$\lambda/x = \frac{\rho+2\lambda}{1+\rho}. \tag{5.3}$$

If $\rho \ll 1$, that is, $V_A^2 \ll c^2$, the above solution approximately equals

$$\lambda/x \cong \rho+2\lambda, \tag{5.4}$$

which is equivalent to (1.3). Note that the appearance of such hydromagnetic waves has been proved with the use of the condition: $V_A^2 \ll c^2$. If $\rho \gg 1$, that is, $V_A^2 \gg c^2$, we have $x \cong 1$; waves are propagated with the light velocity. If the ion sound velocity is much greater than the Alfvén velocity, the propagation velocity is equal not to the Alfvén velocity but to $\sqrt{2}$ times the ion sound velocity.

In order to illustrate the dispersion relation over the whole frequency range, we take an example as follows;

$$V_A = 3\times10^7 \text{ cm/sec}, \qquad C_i = 3\times10^5 \text{ cm/sec}.$$

Accordingly, we have $\rho = (V_A/c)^2 = 10^{-6}$, $\gamma = \rho\mu = 1.836\times10^{-3}$, and $\lambda = (C_i/c)^2 = 10^{-10}$. The results are shown in Fig. 2. As shown by the dispersion relation, the three modes of waves do not appear independently but are coupled with each other through the external magnetic field. However, EM and ES waves are scarcely affected by the magnetic field. As in the case of the absence of the external magnetic field, they cannot be propagated in a frequency range lower than the plasma frequency, or at least, cannot be propagated without attenuation. The phase velocities of EM and ES waves tend to infinity around $\sigma \sim 1+\sqrt{\gamma}$ and $\sigma \sim 1-\sqrt{\gamma}$. IS waves, on the other hand, are greatly modulated in a low-frequency range, where $\sigma \ll \rho$, i.e., $\omega^2 \ll \omega_i\omega_e$; the phase velocity tends to the Alfvén velocity there.

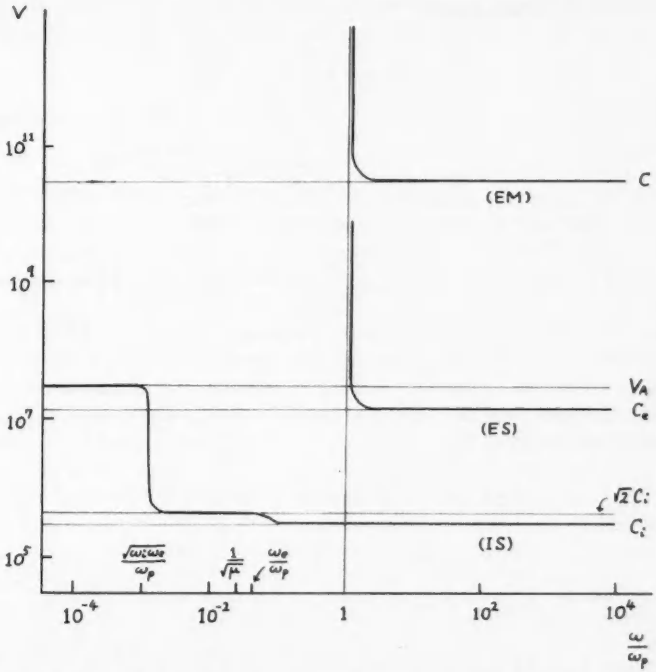

FIG. 2. The dispersion curves of the waves propagated in a fully ionized hydrogen gas and normal to an external magnetic field are shown. Ordinates: propagation velocity in cm/sec. Abscissae: wave frequencies in units of the plasma frequency. C_i and C_e are the propagation velocities of the sound waves in the ion and electron gases in the absence of the external magnetic field. $C_i = 3.10^5$ cm/sec is taken as an example. The electron temperature is assumed to be equal to the ion temperature. V_A, the propagation velocity of the Alfvén waves, is assumed to be 3.10^7 cm/sec. c is the light velocity, equal to 3.10^{10} cm/sec. ω_i and ω_e are the ion and electron gyro-frequencies. μ is the ratio of the ion mass to the electron mass. It may be noticed that the propagation velocity of the IS waves changes abruptly at a frequency $\omega = \sqrt{\omega_i\omega_e}$ and at another frequency $\omega = \omega_e$.

6. ATTENUATION OF HYDROMAGNETIC WAVES DUE TO COLLISIONS

Let us consider the effect of collisions between electrons and ions. Multiplying eqs. (2.10) and (2.11) by $\mathbf{u}_e$ and $\mathbf{u}_i$ respectively, and then adding them, we have

$$(6.1)\qquad \frac{\partial}{\partial t}\left(\tfrac{1}{2}\rho_{e0}u_e^2+\tfrac{1}{2}\rho_{i0}u_i^2\right)+(\mathbf{u}_e\cdot\nabla p_e)+(\mathbf{u}_i\cdot\nabla p_i) = N_p^2\alpha_{ei}(\mathbf{u}_i-\mathbf{u}_e)^2-(\mathbf{j}\cdot\mathbf{E}).$$

The first term of the right-hand side of eq. (6.1) is written as j^2/σ with the definitions of the density of electric currents (eq. (2.16)) and of the electric conductivity σ (eq. (2.21)). The second term of the right-hand side $(\mathbf{j}\cdot\mathbf{E})$ is rewritten as follows, making use of the Maxwell's fundamental equations;

$$(6.2)\qquad (\mathbf{j}\cdot\mathbf{E}) = \operatorname{div}\mathbf{S}+\frac{\partial}{\partial t}\left(\frac{E^2}{8\pi}+\frac{h^2}{8\pi}\right),$$

where **S**, the Poynting's vector, is given by

$$\mathbf{S} = \frac{c}{4\pi}\mathbf{E} \wedge \mathbf{h}. \tag{6.3}$$

One can write

$$(\mathbf{u}_e \cdot \nabla p_e) = \frac{\partial}{\partial t}\left(\frac{1}{2} C_e^2 \frac{\rho_e^2}{\rho_{e0}}\right) \tag{6.4}$$

making use of eqs. (3.3) and (2.31). Finally, we have

$$-\frac{\partial}{\partial t}\left\{(\tfrac{1}{2}\rho_{e0}u_e^2 + \tfrac{1}{2}\rho_{10}u_1^2) + \left(\tfrac{1}{2}C_e^2\frac{\rho_e^2}{\rho_{e0}} + \tfrac{1}{2}C_1^2\frac{\rho_1^2}{\rho_{10}}\right) + \left(\frac{E^2}{8\pi} + \frac{h^2}{8\pi}\right)\right\} = \operatorname{div}\mathbf{S} + \frac{j^2}{\sigma}. \tag{6.5}$$

This is an extended Poynting's theorem. The three terms in the curly bracket represent the kinetic energy of the gas, the potential energy of the gas, and the energy of the electromagnetic field. The first term of the right-hand side represents the source of the electromagnetic energy which is available for propagation and is given by

$$\operatorname{div}\mathbf{S} = i\frac{c}{2\pi}\mathbf{k}\cdot(\mathbf{E} \wedge \mathbf{h}) \tag{6.6}$$

$$= i\frac{2\pi}{\omega}\frac{V^2/c^2}{(1-c^2/V^2)^2} j_y^2.$$

This relation is derived from Maxwell's fundamental equations. The second term, the Joule's heat loss, represents the dissipation of energy due to collisions between electrons and ions. It may be noticed that $1/\sigma$ is proportional to the collision frequency, ν_{ei} (eq. (2.21)).

In hydromagnetic waves, $C_1 \ll V = V_A \ll c$, we have

$$|\operatorname{div}\mathbf{S}| \cong \frac{2\pi}{\omega}\frac{V_A^2}{c^2} j_y^2 \tag{6.7}$$

and this quantity should be greater than the Joule's heat loss in order that hydromagnetic waves may be propagated without severe damping. Equation (3.26) tells us that

$$|j_x| \cong \frac{\omega}{\omega_e}|j_y| \tag{6.8}$$

and thus, $|j_x|$ is much smaller than $|j_y|$, since hydromagnetic waves can exist only in the frequency range, $\omega \ll \sqrt{\omega_1\omega_e} < \omega_e$. Therefore, j^2/σ is almost equal to j_y^2/σ, and the condition of slight attenuation is given by

$$\frac{2\pi}{\omega}\frac{V_A^2}{c^2} \gg \frac{1}{\sigma} \tag{6.9}$$

or

$$\omega\nu_{ei} \ll \tfrac{1}{2}\omega_1\omega_e. \tag{6.10}$$

It may be noticed that the condition is not governed by Pedersen or Hall conductivities, but by the total conductivity. In the inverse case of

$$\omega\nu_{el} \gg \tfrac{1}{2}\omega_1\omega_e$$

hydromagnetic waves are heavily attenuated.

7. CONCLUSIONS

Three modes of plane waves, in which the perturbed magnetic field is parallel to the external magnetic field, can be propagated in a collision-free and fully ionized gas and transverse to the external magnetic field. They are coupled to each other through the magnetic field. In a high-frequency limit, the couplings are loosened, and the three modes of waves behave as electromagnetic (EM) waves, electron sound (ES) waves, and ion sound (IS) waves. In the condition that the Alfvén velocity is sufficiently smaller than the light velocity and sufficiently greater than the ion sound velocity, the first two modes of waves are scarcely influenced by the magnetic field. Their phase velocities tend to infinity around the plasma frequency, and they cannot be propagated at all, or, at best, they propagate with attenuation in frequencies lower than the plasma frequency. The last mode of waves, however, can be propagated without attenuation over the whole frequency range, and are greatly modulated by the magnetic field at frequencies sufficiently lower than a critical frequency, which is given by the geometrical mean of the ion and electron gyro-frequencies. In that frequency range, they become hydromagnetic waves; they are propagated not with the ion sound velocity but with the Alfvén velocity. The hydromagnetic waves are heavily attenuated if the collision frequency between ions and electrons is so large that the product of the collision frequency and the wave frequency is much greater than the product of the ion and electron gyro-frequencies.

Waves in which the electric field and the currents are parallel to the external magnetic field are neither influenced by the magnetic field nor coupled with any other wave of the above modes. They can be propagated as electromagnetic waves at frequencies greater than the plasma frequency.

REFERENCES

ALFVÉN, H. 1950. Cosmical electrodynamics (Clarendon Press, Oxford).
ASTRÖM, E. 1951. Arkiv Fysik, **2**, 443.
FERRARO, V. C. A. 1955. Proc. Roy. Soc. (London), A, **233**, 310.
VAN DE HULST, H. C. 1951. Proc. Symposium on Motion of Gaseous Masses of Cosmical Dimensions, Paris, 1949 (Central Air Documents Office).
LANDAU, L. 1946. J. Phys. U.S.S.R. **10**, 25.
PIDDINGTON, J. H. 1955. Phil. Mag. Ser. 7, **46**, 1037.
SCHLÜTER, A. 1950. Z. Naturforsch. **59**, 72.
——— 1951. Z. Naturforsch. **69**, 73.
——— 1952. Ann. Physik. 6, **10**, 418.
SPITZER, L., JR. 1956. Physics of fully ionized gases (Interscience Publishers, Inc., New York).

THE *K–LL* AUGER SPECTRUM OF $_{66}Dy^{161}$ [1]

ROBERT L. GRAHAM AND JANET S. MERRITT

ABSTRACT

The *K–LL* Auger spectrum of $_{66}Dy^{161}$ has been studied using the Chalk River iron-free β-ray spectrometer at an instrumental resolution of ~0.07%. After correcting for the estimated intensity of the L_3 43.81-kev conversion line (96% $M1+4\%$ $E2$), which coincides with the second ($K–L_1L_2$) Auger line, the following energies and intensities are obtained for the seven Auger lines:

Energy (kev)	35.492 ±0.006	35.963 ±0.007	36.369 ±0.007	36.732 ±0.007	36.806 ±0.010	37.195 ±0.006	38.002 ±0.009
Relative intensity	1.00 ±0.03	1.31 ±0.05	0.22 ±0.05	0.83 ±0.05	0.28 ±0.03	2.39 ±0.05	1.07 ±0.08

The energies are from 20 to 50 ev higher than the non-relativistic predictions. The relative intensities are consistent with experimental results at other atomic numbers.

INTRODUCTION

In previous papers (Ewan *et al.* 1959, 1960; Ewan and Merritt 1960) measurements of the *K–LL* Auger spectra in this laboratory at $Z = 62$, 64, and 94 have been reported. The results confirm, qualitatively, the theoretical predictions of Asaad and Burhop (1958), but are not in quantitative agreement either as to energies or relative intensities. However, the experiments have confirmed one important feature predicted by their theory, namely, the existence of the $L_1L_3(^3P_1)$ satellite line. This supports their assumption that the coupling between electron-shell vacancies is neither pure *j–j* nor pure *L–S* since more than six lines are observed. On the assumption that the coupling is intermediate between *L–S* and *j–j*, they predict that the *K–LL* Auger spectrum should have nine lines, i.e., six main lines plus three satellite lines of low intensity. The predicted intensities and energies of the latter are such that only the $L_1L_3(^3P_1)$ satellite should be easily detected experimentally. The other two are predicted to be less intense and closer to their partners, hence much more difficult to observe.

In this paper we report measurements of the *K–LL* Auger lines in $_{66}Dy^{161}$. These results were obtained during a detailed study of the internal conversion spectrum following $_{65}Tb^{161}$ beta decay (Graham *et al.* 1961), which will be described fully elsewhere. The results again confirm the existence of a $L_1L_3(^3P_1)$ satellite line observed in earlier experiments. The relative intensities at $Z = 66$ are consistent with those at neighboring values of Z. The systematic variation with Z, indicated by other measurements, is in reasonable agreement with the theoretical relativistic intensity ratios at $Z = 80$ (Asaad 195J).

EXPERIMENTAL PROCEDURE AND RESULTS

Tb^{161} was produced according to the sequence $Gd^{160}(n,\gamma)Gd^{161}\beta^- \rightarrow Tb^{161}$. Enriched Gd^{160} was irradiated in the NRX reactor at a flux of 6×10^{13} n/sq cm/

[1]Manuscript received April 13, 1961.
Contribution from General Physics Branch, Atomic Energy of Canada Limited, Chalk River, Ontario.
Issued as A.E.C.L. No. 1263.

sec for 30 days. Following irradiation the two elements were separated by elution from an ion exchange column with ammonium α-hydroxy-isobutyrate (Smith and Hoffman 1956). To purify the product from the eluting agent the Tb^{161} fraction was acidified and absorbed on a very small Dowex-50 column (0.03 $cm^2 \times 5$ cm); the bed was washed with 30 column volumes of 0.2 *N* HCl, and the Tb^{161} was eluted with 6 *N* HCl. Polythene ware was used throughout the procedure to minimize contamination by material from container walls. The final product was sublimed from a boat-shaped tantalum filament through a slit 0.030 in. wide onto 800 $\mu g/cm^2$ thick aluminum foil. Several different sources were prepared in this way; the results reported here were obtained from one having an initial strength of $\sim 100\ \mu c$ and an estimated surface density of $\lesssim 50\ \mu g/cm^2$.

The Auger spectrum was studied in the Chalk River double-focusing β-ray spectrometer (Graham *et al.* 1960) at a resolution setting of $\sim 0.07\%$. The focused electrons were detected in a side-window continuous-flow proportional counter having a thin ($\lesssim 100\ \mu g/cm^2$) VYNS plastic film window. The window was supported by a fine mesh metallic grid ($\sim 90\%$ open area) and the methane filling was maintained at a pressure of ~8 cm Hg absolute. The detector efficiency under these conditions is essentially constant, and equal to the open area of the window grid, for the electron energy region of interest here.

The *K–LL* Auger spectrum is shown in Fig. 1, plotted on a linear scale. The data were taken automatically and recorded both by an electric typewriter and on punched tape. Six successive sweeps were made of this region of the Tb^{161} spectrum using 40-second counting intervals. The six runs were added

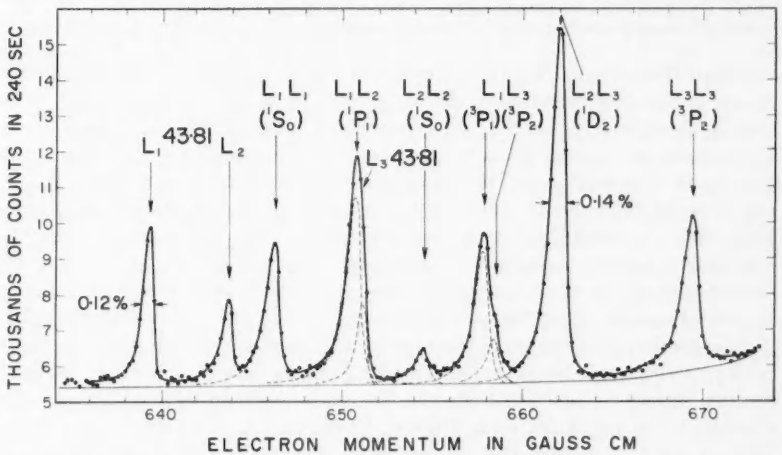

FIG. 1. The *K–LL* Auger spectrum in $_{66}Dy^{161}$ following β-decay from $_{65}Tb^{161}$. The shape of the background from the β-continuum and tails of higher-energy intense conversion lines is shown by the thin solid line. The components of the complex lines are shown by broken lines and discussed in the text. The $L_1L_2(^3P_2)$ satellite line is predicted theoretically by Asaad and Burhop.

and corrected for variations in counter background rate (air-borne A^{41} activity discussed by Graham *et al.* 1960) directly from the punched tape record using IBM accounting equipment. The Auger peaks are all wider than the instrumental peak shape for two reasons, i.e., natural width and source thickness. The former effect accounts for the difference in width between the L conversion lines of γ 43.81 and the Auger lines; the latter is indicated by the pronounced asymmetric low-energy tail on all lines.

The measured energies and relative intensities of the Auger lines are summarized in Table I. The energy uncertainties listed are intended to represent

TABLE I

Comparison of experimental and theoretical energies and relative intensities of the K–LL Auger lines in $_{66}Dy^{161}$

Transition	Energy in kev		Relative intensities		
			Non-rel. theor.[b]	Experimental	
	Exptl.	Non-rel. theor.[a]	$Z = 66$	$_{66}Dy^{166}$	$_{62}Sm^{152}$[c]
$L_1L_1(^1S_0)$	35.492±0.006	35.455	1.00	1.00±0.03	1.00±0.05
$L_1L_2(^1P_1)$	35.963±0.007	35.938	1.27	1.31±0.05[d]	1.39±0.06
$L_1L_2(^3P_0)$		35.972	0.047		
$L_2L_2(^1S_0)$	36.369±0.007	36.350	0.17	0.22±0.05	0.26±0.06
$L_1L_3(^3P_1)$	36.732±0.007	36.698	1.90	0.83±0.05[e]	1.18±0.06
$L_1L_3(^3P_2)$	36.806±0.010	36.763	0.24	0.28±0.03[e]	0.29±0.09
$L_2L_3(^1D_2)$	37.195±0.006	37.148	4.43	2.39±0.05	3.14±0.13
$L_2L_3(^3P_0)$		37.904	0.25		
$L_3L_3(^3P_2)$	38.002±0.009	37.950	2.03	1.07±0.08	1.39±0.06

[a]Using the binding energies of Bergvall and Hagstrom (1960).
[b]Asaad and Burhop (1958).
[c]Ewan *et al.* (1960).
[d]After subtraction of the L_3 conversion line of the 43.81-kev γ-transition as shown in Fig. 1.
[e]The total intensity of this partially resolved doublet is 1.11 ±0.04.

standard deviations. They are a combination in quadrature of the possible errors in absolute calibration and those due to statistical fluctuations. The spectrometer was calibrated using sources of Bi^{212} (ThB), Au^{198}, and Cs^{137}. Corrections were made for a small asymmetry in source position relative to the dowel mounting pins. This was determined by rotating the source mount ring through 180° and remeasuring the positions of several intense conversion lines with the source in the inverted position. Throughout these runs the degaussing system currents were adjusted automatically to compensate for fluctuations in the earth's magnetic field, using the electrical signals from an improved version of the Serson three-component magnetometer (Serson 1957). This control system now maintains the mean value of the vertical field component at the spectrometer to $\lesssim \pm 1 \times 10^{-4}$ gauss even during severe magnetic storms. Errors in line positions due to uncertainty in degaussing are now thought to be negligible, i.e., $\lesssim \pm 0.01$ gauss cm or $\simeq \pm 1$ ev for the Auger lines in question. Errors due to lack of reproducibility in source positioning are also negligible since the source rings are machined accurately to fit snugly on a pair of locating dowels; the position is reproducible within ~ 0.003 cm (Graham *et al.* 1960), which corresponds to an error in Auger-line energy of

$\lesssim$0.6 ev. Using the K line of the 411.770-kev transition in Hg^{198} as our basic standard (momentum = 2222.39±0.14 gauss cm) the more intense conversion lines in Dy^{161} show an internal consistency of $\lesssim$2 ev if we employ the binding energies of Bergvall and Hagstrom (1960) including the work function, ϕ_{sp}. The consistency expected for the Auger lines is somewhat poorer for two reasons: (*a*) the statistical accuracy is poorer, and (*b*) there were small drifts in current settings during the long automatic run. The current settings were measured before and after the six sweeps and showed a drift of ~2 parts in 10^5. The positions of the L_1 and L_2 43.81-kev lines were measured during subsequent calibration runs and hence provide a secondary calibration for the K–LL Auger lines. Their energies agree with the later measurements to within ±4 ev. The relative energies are more accurate than the errors indicated in Table I by perhaps a factor of 2.

The intensities of the various peaks have been deduced from the line areas. In order to calculate areas it is necessary to know the shape of the spectrum under each line including the magnitude and shape of the tails of the lines at higher energy. For purposes of analysis it was assumed that all Auger lines had a shape the same as that of the prominent K–L_2L_3 line. The height and slope of the background line shown in Fig. 1 is that found empirically which satisfies this criterion. The increasing slope at high momentum is due to the tail of the very intense L_1 48.91-kev conversion line at ~686 gauss cm. The matching of line shapes was carried out graphically using semilogarithmic plots as described in earlier papers (Ewan *et al.* 1959; Graham *et al.* 1960). The intensity errors listed in Table I are intended to represent standard deviations although the method of analysis is somewhat subjective, i.e., the results depend upon the shape of the tails and the choice of the background shape which is subtracted. The errors quoted are those from counting statistics combined in quadrature with an arbitrary 10% error assigned to all estimated tail areas and an error ranging from ±30 counts to ±100 counts per 240 seconds for the background line.

The energy and intensity one deduces for the K–L_1L_2 Auger line depend upon the contribution assumed for the unresolved L_3 43.81-kev component. The 43.81-kev transition has been assigned as 96% $M1$+4% $E2$ and is identified as a transition de-exciting the first rotational state based on the 5/2+ ground state of Dy^{161} (Graham *et al.* 1961). On this basis the intensity of the L_3 line should be equal to that of the L_2 43.81-kev line as shown by the broken line in Fig. 1. The K–L_1L_2 line intensity error quoted in Table I includes allowance for a ±20% uncertainty in the intensity of the L_3 43.81-kev line; the error quoted for its energy includes an allowance for uncertainties in both the position and the intensity of the L_3 43.81-kev line.

DISCUSSION OF RESULTS

(a) Line Energies

In column 3 of Table I are listed the energies predicted theoretically for $Z = 66$ by the formulae of Asaad and Burhop after insertion of the binding energies of Bergvall and Hagstrom (1960). The measured energies are from

19 to 49 ev higher, i.e. by amounts too large to be ascribed to experimental errors. The discrepancies are comparable to those found previously for $Z = 62$, 64, and 94 (Ewan *et al.* 1959, 1960; Ewan and Merritt 1960) and are here mainly attributable to the inadequacy of the non-relativistic energy formulae of Asaad and Burhop (1958), which includes semiempirical correction factors based on the measured K–LL energies at $Z = 83$ (Mladjenovic and Slätis 1954). Relativistic energy predictions are not available for $Z = 66$. In his recent paper, Asaad (1959) does, however, make relativistic energy predictions at $Z = 80$. The discrepancies between these and the measured energies of Bergstrom and Hill (1954) at $Z = 80$ are as large as 200 ev, which suggests that the present theoretical techniques are not capable of predicting Auger-line energies with the precision now obtainable experimentally.

(b) Relative Intensities

As was discussed in an earlier paper (Ewan *et al.* 1960) there is always the possibility that the apparent Auger-line intensities may be altered by low-intensity conversion lines close to or coincident with the lines in question. The $L_1L_2(^1P_1)+L_3$ 43.81 unresolved doublet is a good example. The presence of the 43.81-kev transition in Tb^{161} decay became certain only after a detailed study of the entire conversion electron spectrum had been made and the Dy^{161} level scheme was firmly established. Even after substracting the predicted L_3 43.81-kev contribution, the remaining intensity assigned to the K–L_1L_2 Auger line is significantly higher than for $Z = 62$, as is also the K–L_1L_1 line. The other Auger-line intensities are, however, in acceptable agreement with the $Z = 62$ values.

In Fig. 2 we compare the relative intensities reported here with the theoretical predictions and experimental values at other values of Z. The intense K–$L_2L_3(^1D_2)$ line has been selected as the reference rather than the less intense K–$L_1L_1(^1S_0)$ line. The solid lines are the non-relativistic predictions of Asaad and Burhop. The relativistic predictions at $Z = 80$ are indicated by the arrows. The broken lines show the trends of the experimental intensity ratios with Z and agree well with the relativistic predictions at $Z = 80$ except for the weak K–$L_2L_2(^1S_0)$ line where the prediction is too low. The new results are consistent with the trend indicated by the other experimental results within errors. This comparison again points up the inadequacy of the non-relativistic theory. The latter does, however, predict with reasonable accuracy intensity ratios of the three lines involving the L_3 shell and also those for the three lines not involving the L_3 shell but, at high Z, is in error by a factor of 3 to 4 for the ratio between these two groups.

The present results at $Z = 66$ once again provide convincing evidence for the K–$L_1L_3(^3P_2)$ satellite line and confirm the previously reported evidence for it at $Z = 62$, 64, and 94. The statistical accuracy of the present results permits a more accurate estimate of the intensity of this line than was possible in the earlier work at this laboratory although it is not fully resolved. Its intensity is consistent with the earlier results at $Z = 62$ and 64 but the experimental ratio for $^3P_2$ to $^3P_1$ is about a factor of 2 larger than predicted in the non-relativistic theory. The corresponding ratio is not explicitly available from Asaad's relativistic calculations at $Z = 80$.

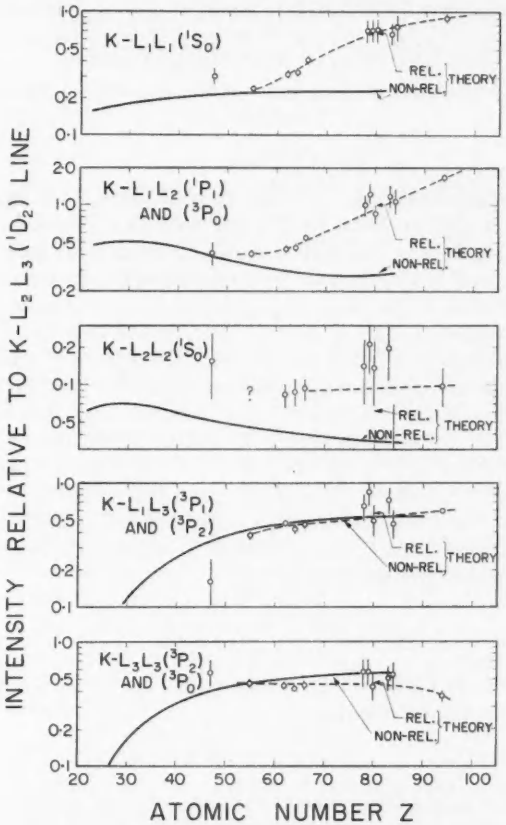

FIG. 2. Comparison of *K–LL* Auger-line intensities relative to the intense K–$L_2L_3(^1D_2)$ line. The non-relativistic predictions of Asaad and Burhop (1958) are shown by the solid lines. The broken lines are guides to the eye through the experimental points. The relativistic predictions of Asaad (1959) at $Z = 80$ are shown by the arrows. The experimental points are from the following sources: $Z = 47$, Johnson and Foster (1953); $Z = 55$, Graham *et al.* (1961*b*); $Z = 62$, Ewan, Graham, and Grodzins (1960); $Z = 64$, Ewan and Merritt (1960); $Z = 66$, present work; $Z = 78$, Ewan (1957); $Z = 79$, Hill (1953); $Z = 80$, Bergstrom and Hill (1954); $Z = 83$, Slätis (1955); $Z = 84$, Gray (1956); $Z = 94$, Ewan *et al.* (1959). The error bars for the $Z = 55$, 62, 64, 66, and 94 results indicate standard deviations; the results at other Z values are from photographic intensities and have been assigned errors similar to those estimated by Ewan (1957) for his photographic results. A value of $(K\text{–}L_2L_2)/(K\text{–}L_1L_3) \simeq 0.08$ has been assumed for the purposes of plotting the $Z = 55$ results.

(c) Absolute Intensities and Fluorescent Yield

The sum of the intensities of the *K–LL* Auger lines relative to that for *K* conversion lines in Dy^{161} is 0.0375 ± 0.004. An accurate measurement of the intensity of the *K–LM*, *K–MM*, etc. lines has not been attempted in this work since these spectra are much more complex and difficult to interpret. Moreover, they are partially masked by conversion lines. However, the intensity ratio $[(K\text{–}LY)+(K\text{–}XY)]/[K\text{–}LL]$ is a slowly varying function of

Z (see, for example, Gray 1956 and Wapstra *et al.* 1959). Taking 0.6 ± 0.1 as the value for this ratio at $Z = 66$ one deduces that the fluorescent yield at $Z = 66$ is $\omega_k = 0.943 \pm 0.007$. This is to be compared with the value of $\omega_k = 0.926$ for $Z = 66$ computed from the semiempirical formula quoted by Wapstra *et al.* (1959).

CONCLUSIONS

The present experimental results again provide convincing evidence for the most prominent satellite K–$L_1L_3(^3P_2)$ line predicted by the non-relativistic theory of Asaad and Burhop and confirm earlier evidence from this laboratory of its occurrence at $Z = 62$, 64, and 94. It is therefore clear that the final electronic configuration of the atom must be described in terms of a coupling between the two L-shell vacancies which is intermediate between j–j and L–S even at the highest atomic numbers. The six-line spectrum predicted for extreme j–j (or L–S) coupling is not consistent with our experiments.

The relative intensities of the K–LL Auger lines are shown to be consistent with five of the six intensities predicted by Asaad (1959) from his detailed relativistic calculations at $Z = 80$. The K–$L_2L_2(^1S_0)$ lines observed experimentally are, however, appreciably stronger than this theoretical prediction. A fully relativistic calculation at lower Z values, taking intermediate coupling into account, would provide a more rigid test of the validity of Asaad's assumptions than is presently possible.

ACKNOWLEDGMENTS

The authors would like to thank Miss Helen Howard for numerical computations, Messrs. R. B. Walker and W. Perry for technical assistance, and Dr. G. T. Ewan for helpful discussions.

REFERENCES

Asaad, W. N. 1959. Proc. Roy. Soc. A, **249**, 555.
Asaad, W. N. and Burhop, E. H. S. 1958. Proc. Phys. Soc. **71**, 369.
Bergstrom, I. and Hill, R. D. 1954. Arkiv Fysik, **8**, 21.
Bergvall, P. and Hagstrom, S. 1960. Arkiv Fysik, **17**, 61.
Ewan, G. T. 1957. Can. J. Phys. **35**, 672, and private communication.
Ewan, G. T., Geiger, J. S., Graham, R. L., and MacKenzie, D. R. 1959. Can. J. Phys. **37**, 174.
Ewan, G. T., Graham, R. L., and Grodzins, L. 1960. Can. J. Phys. **38**, 163.
Ewan, G. T. and Merritt, J. S. 1960. Can. J. Phys. **38**, 324.
Graham, R. L., Ewan, G. T., and Geiger, J. S. 1960. Nucl. Instr. and Methods, **9**, 245.
Graham, R. L., Geiger, J. S., and Ewan, G. T. 1961*a*. Bull. Am. Phys. Soc. Ser. II, **6**, 72.
Graham, R. L., Brown, F., Ewan, G. T., and Uhler, J. 1961*b*. Can. J. Phys. **39**. This issue.
Gray, P. R. 1956. Phys. Rev. **101**, 1306.
Hill, R. D. 1953. Phys. Rev. **91**, 770.
Johnson, F. A. and Foster, J. S. 1953. Can. J. Phys. **31**, 469.
Mladjenovic, M. and Slätis, H. 1954. Arkiv Fysik, **9**, 41.
Serson, P. 1957. Can. J. Phys. **35**, 1387.
Slätis, H. 1955. *Quoted in* Beta- and gamma-ray spectroscopy, *edited by* K. Siegbahn (North-Holland Pub. Co.), p. 631.
Smith, H. L. and Hoffman, D. C. 1956. J. Inorg. & Nuclear Chem. **3**, 243.
Wapstra, A. H., Nijgh, G. J., and van Lieshout, R. 1959. Nuclear spectroscopy tables (North-Holland Pub. Co.), pp. 81 and 84.

A NOTE ON THE DIFFRACTION OF A SCALAR WAVE BY A SMALL CIRCULAR APERTURE[1]

R. A. HURD

ABSTRACT

The power series solution for the diffraction of a scalar plane wave incident normally on a small circular aperture in a hard screen is extended to include terms of order α^{12} in the aperture field, and to terms of order α^{10} in the transmission coefficient ($\alpha = 2\pi \times$ radius of aperture/wavelength). To do this, a set of recurrence relations is developed, and a relatively simple method of obtaining the transmission coefficient is devised.

INTRODUCTION

In the course of some recent work on diffraction theory, a power series solution was obtained for the diffraction problem of a plane wave normally incident upon a small circular aperture in a hard screen. It is believed that the power series (in $\alpha = 2\pi a/\lambda$, where a is the radius of the aperture) has been carried somewhat further than formerly. Thus the series for the aperture distribution function includes terms of $O(\alpha^{12})$ while the transmission coefficient τ contains terms of $O(\alpha^{10})$. In addition, recurrence formulae have been developed which allow (in principle) the calculation of the aperture field to any order in α. Also, a relatively simple expression for the transmission coefficient of the aperture has been found.

FORMULAE AND RESULTS

An integral equation derived by Bazer and Brown (1959) forms the starting point of the analysis:

$$h(x) = \cosh \alpha x + \beta \int_{-1}^{1} \frac{\sinh \alpha(x-y)}{x-y} h(y)\, dy, \tag{1}$$

where $\beta = -i/\pi$. The (suppressed) time dependence is $e^{-i\omega t}$. The function $h(x)$ in equation (1) is essentially an aperture distribution function and is related to Bazer and Brown's function $f_2(x)$ by $h(x) = (\pi/a)f_2(x)$.

A solution to equation (1) was found by assuming an expansion of $h(x)$ of the form

$$h(x) = \sum_{n=0}^{\infty} \alpha^n h_n(x), \tag{2}$$

where

$$h_n(x) = \sum_{m=0}^{[n/2]} \zeta_{2m}^{n} x^{2m}. \tag{3}$$

The notation $[p]$ in equation (3) means the greatest integer $\leqslant p$.

[1]Manuscript received April 5, 1961.
Contribution from the Division of Radio and Electrical Engineering, National Research Council, Ottawa, Canada.
Issued as N.R.C. No. 6367.

TABLE I

The coefficients ζ^n_{2m}

$\zeta^0_0 = 1.$

$\zeta^1_0 = 2\beta.$

$\zeta^2_0 = 4\beta^2, \quad \zeta^2_2 = \frac{1}{2}.$

$\zeta^3_0 = \frac{4}{9}\beta + 8\beta^3, \quad \zeta^3_2 = \frac{1}{3}\beta.$

$\zeta^4_0 = \frac{4}{3}\beta^2 + 16\beta^4, \quad \zeta^4_2 = \frac{2}{3}\beta^2, \quad \zeta^4_4 = \frac{1}{24}.$

$\zeta^5_0 = \frac{4}{75}\beta + \frac{32}{9}\beta^3 + 32\beta^5, \quad \zeta^5_2 = \frac{4}{45}\beta + \frac{4}{3}\beta^3, \quad \zeta^5_4 = \frac{1}{60}\beta.$

$\zeta^6_0 = \frac{508}{2025}\beta^2 + \frac{80}{9}\beta^4 + 64\beta^6, \quad \zeta^6_2 = \frac{34}{135}\beta^2 + \frac{8}{3}\beta^4, \quad \zeta^6_4 = \frac{1}{30}\beta^2, \quad \zeta^6_6 = \frac{1}{720}.$

$\zeta^7_0 = \frac{8}{2205}\beta + \frac{8}{9}\beta^3 + \frac{64}{3}\beta^5 + 128\beta^7, \quad \zeta^7_2 = \frac{22}{1575}\beta + \frac{88}{135}\beta^3 + \frac{16}{3}\beta^5,$

$\zeta^7_4 = \frac{1}{210}\beta + \frac{1}{15}\beta^3, \quad \zeta^7_6 = \frac{1}{2520}\beta.$

$\zeta^8_0 = \frac{1112}{33,075}\beta^2 + \frac{1856}{675}\beta^4 + \frac{448}{9}\beta^6 + 256\beta^8, \quad \zeta^8_2 = \frac{746}{14,175}\beta^2 + \frac{8}{5}\beta^4 + \frac{32}{3}\beta^6,$

$\zeta^8_4 = \frac{5}{378}\beta^2 + \frac{2}{15}\beta^4, \quad \zeta^8_6 = \frac{1}{1260}\beta^2, \quad \zeta^8_8 = \frac{1}{40,320}.$

$\zeta^9_0 = \frac{4}{25,515}\beta + \frac{5728}{35,721}\beta^3 + \frac{15,872}{2025}\beta^5 + \frac{1024}{9}\beta^7 + 512\beta^9, \quad \zeta^9_2 = \frac{22}{19,845}\beta + \frac{100}{567}\beta^3 + \frac{512}{135}\beta^5 + \frac{64}{3}\beta^7,$

$\zeta^9_4 = \frac{23}{28,350}\beta + \frac{32}{945}\beta^3 + \frac{4}{15}\beta^5, \quad \zeta^9_6 = \frac{1}{8505}\beta + \frac{1}{630}\beta^3, \quad \zeta^9_8 = \frac{1}{181,440}\beta.$

$\zeta^{10}_0 = \frac{2852}{826,875}\beta^2 + \frac{78,224}{127,575}\beta^4 + \frac{14,272}{675}\beta^6 + 256\beta^8 + 1024\beta^{10},$

$\zeta^{10}_2 = \frac{3844}{496,125}\beta^2 + \frac{22,448}{42,525}\beta^4 + \frac{1184}{135}\beta^6 + \frac{128}{3}\beta^8, \quad \zeta^{10}_4 = \frac{407}{141,750}\beta^2 + \frac{26}{315}\beta^4 + \frac{8}{15}\beta^6,$

$\zeta^{10}_6 = \frac{11}{34,020}\beta^2 + \frac{1}{315}\beta^4, \quad \zeta^{10}_8 = \frac{1}{90,720}\beta^2, \quad \zeta^{10}_{10} = \frac{1}{3,628,800}.$

$\zeta^{11}_0 = \frac{8}{1,715,175}\beta + \frac{509,368}{22,325,625}\beta^3 + \frac{73,856}{35,721}\beta^5 + \frac{36,992}{675}\beta^7 + \frac{5120}{9}\beta^9 + 2048\beta^{11},$

$\zeta^{11}_2 = \frac{74}{1,403,325}\beta + \frac{152,224}{4,465,125}\beta^3 + \frac{20,864}{14,175}\beta^5 + \frac{896}{45}\beta^7 + \frac{256}{3}\beta^9,$

$\zeta^{11}_4 = \frac{74}{1,091,475}\beta + \frac{223}{23,625}\beta^3 + \frac{184}{945}\beta^5 + \frac{16}{15}\beta^7,$

$\zeta^{11}_6 = \frac{13}{623,700}\beta + \frac{1}{1215}\beta^3 + \frac{2}{315}\beta^5, \quad \zeta^{11}_8 = \frac{1}{598,752}\beta + \frac{1}{45,360}\beta^3, \quad \zeta^{11}_{10} = \frac{1}{19,958,400}\beta.$

$\zeta^{12}_0 = \frac{446,024}{1,620,840,375}\beta^2 + \frac{623,024}{5,740,875}\beta^4 + \frac{1,910,528}{297,675}\beta^6 + \frac{55,808}{405}\beta^8 + \frac{11,264}{9}\beta^{10} + 4096\beta^{12},$

$\zeta^{12}_2 = \frac{214,682}{245,581,875}\beta^2 + \frac{238,328}{1,913,625}\beta^4 + \frac{18,464}{4,725}\beta^6 + \frac{6016}{135}\beta^8 + \frac{512}{3}\beta^{10},$

$\zeta^{12}_4 = \frac{21,433}{49,116,375}\beta^2 + \frac{848}{30,375}\beta^4 + \frac{424}{945}\beta^6 + \frac{32}{15}\beta^8, \quad \zeta^{12}_6 = \frac{6029}{84,199,500}\beta^2 + \frac{17}{8,505}\beta^4 + \frac{4}{315}\beta^6,$

$\zeta^{12}_8 = \frac{41}{8,981,280}\beta^2 + \frac{1}{22,680}\beta^4, \quad \zeta^{12}_{10} = \frac{1}{9,979,200}\beta^2, \quad \zeta^{12}_{12} = \frac{1}{479,001,600}.$

TABLE II

The coefficients ρ_t^r

$$\rho_0^0 = \frac{1}{n}.$$

$$\rho_0^1 = \frac{2\beta}{n}.$$

$$\rho_1^2 = \frac{1}{6}+4\beta^2, \quad \rho_3^2 = \frac{1}{10}+\frac{4}{3}\beta^2, \quad \rho_5^2 = \frac{1}{14}+\frac{4}{5}\beta^2, \quad \rho_7^2 = \frac{1}{18}+\frac{4}{7}\beta^2, \quad \rho_9^2 = \frac{1}{22}+\frac{4}{9}\beta^2.$$

$$\rho_1^3 = \frac{5}{9}\beta+8\beta^3, \quad \rho_3^3 = \frac{29}{135}\beta+\frac{8}{3}\beta^3, \quad \rho_5^3 = \frac{43}{315}\beta+\frac{8}{5}\beta^3,$$

$$\rho_7^3 = \frac{19}{189}\beta+\frac{8}{7}\beta^3, \quad \rho_9^3 = \frac{71}{891}\beta+\frac{8}{9}\beta^3.$$

$$\rho_1^4 = \frac{1}{120}+\frac{14}{9}\beta^2+16\beta^4, \quad \rho_3^4 = \frac{1}{168}+\frac{26}{45}\beta^2+\frac{16}{3}\beta^4,$$

$$\rho_5^4 = \frac{1}{216}+\frac{38}{105}\beta^2+\frac{16}{5}\beta^4, \quad \rho_7^4 = \frac{1}{264}+\frac{50}{189}\beta^2+\frac{16}{7}\beta^4.$$

$$\rho_1^5 = \frac{233}{2700}\beta+4\beta^3+32\beta^5, \quad \rho_3^5 = \frac{239}{6300}\beta+\frac{196}{135}\beta^3+\frac{32}{3}\beta^5,$$

$$\rho_5^5 = \frac{2383}{94,500}\beta+\frac{284}{315}\beta^3+\frac{32}{5}\beta^5, \quad \rho_7^5 = \frac{11,857}{623,700}\beta+\frac{124}{189}\beta^3+\frac{32}{7}\beta^5.$$

$$\rho_1^6 = \frac{1}{5040}+\frac{461}{1350}\beta^2+\frac{88}{9}\beta^4+64\beta^6, \quad \rho_3^6 = \frac{1}{6480}+\frac{11,801}{85,050}\beta^2+\frac{472}{135}\beta^4+\frac{64}{3}\beta^6,$$

$$\rho_5^6 = \frac{1}{7920}+\frac{12,737}{141,750}\beta^2+\frac{136}{63}\beta^4+\frac{64}{5}\beta^6.$$

$$\rho_1^7 = \frac{2459}{264,600}\beta+\frac{2267}{2025}\beta^3+\frac{208}{9}\beta^5+128\beta^7, \quad \rho_3^7 = \frac{18,763}{3,969,000}\beta+\frac{229}{525}\beta^3+\frac{368}{45}\beta^5+\frac{128}{3}\beta^7,$$

$$\rho_5^7 = \frac{1913}{582,120}\beta+\frac{263}{945}\beta^3+\frac{176}{35}\beta^5+\frac{128}{5}\beta^7.$$

$$\rho_1^8 = \frac{1}{362,880}+\frac{12,841}{238,140}\beta^2+\frac{2234}{675}\beta^4+\frac{160}{3}\beta^6+256\beta^8,$$

$$\rho_3^8 = \frac{1}{443,520}+\frac{47,053}{1,984,500}\beta^2+\frac{17,798}{14,175}\beta^4+\frac{2528}{135}\beta^6+\frac{256}{3}\beta^8.$$

$$\rho_1^9 = \frac{201,743}{285,768,000}\beta+\frac{403,901}{1,786,050}\beta^3+\frac{412}{45}\beta^5+\frac{1088}{9}\beta^7+512\beta^9,$$

$$\rho_3^9 = \frac{760,913}{1,886,068,800}\beta+\frac{100,453}{1,071,630}\beta^3+\frac{28,996}{8,505}\beta^5+\frac{5696}{135}\beta^7+\frac{512}{3}\beta^9.$$

$$\rho_1^{10} = \frac{1}{39,916,800}+\frac{4,753,379}{714,420,000}\beta^2+\frac{719,851}{893,025}\beta^4+\frac{48,952}{2025}\beta^6+\frac{2432}{9}\beta^8+1024\beta^{10}.$$

$$\rho_1^{11} = \frac{8,084,789}{207,467,568,000}\beta+\frac{1,107,979}{30,618,000}\beta^3+\frac{464,026}{178,605}\beta^5+\frac{4624}{75}\beta^7+\frac{1792}{3}\beta^9+2048\beta^{11}.$$

When equations (2) and (3) were substituted in the integral equation it was found that the ζ_{2m}^n satisfied the following relation:

$$\zeta_{2m}^n = 2\beta \sum_{r=m}^{[(n-1)/2]} \binom{2r}{2m} \frac{1}{(2r+1)!} \rho_{2r-2m+1}^{n-2r-1} + \delta_{2m,n}\, x^n/n!, \tag{4}$$

in which

TABLE III

The coefficients τ_{2n}.

$$\frac{\pi^2}{4}\tau_0 = 2.$$

$$\frac{\pi^2}{4}\tau_2 = \frac{8}{9}+8\beta^2.$$

$$\frac{\pi^2}{4}\tau_4 = \frac{142}{675}+\frac{16}{3}\beta^2+32\beta^4.$$

$$\frac{\pi^2}{4}\tau_6 = \frac{1136}{33{,}075}+\frac{3872}{2025}\beta^2+\frac{256}{9}\beta^4+128\beta^6.$$

$$\frac{\pi^2}{4}\tau_8 = \frac{19{,}046}{4{,}465{,}125}+\frac{86{,}336}{178{,}605}\beta^2+\frac{608}{45}\beta^4+\frac{1280}{9}\beta^6+512\beta^8.$$

$$\frac{\pi^2}{4}\tau_{10} = \frac{658{,}136}{1{,}620{,}840{,}375}+\frac{1{,}280{,}408}{13{,}395{,}375}\beta^2+\frac{161{,}408}{35{,}721}\beta^4+\frac{56{,}576}{675}\beta^6+\frac{2048}{3}\beta^8+2048\beta^{10}.$$

$$\rho_t^s = \sum_{m=0}^{[s/2]} \frac{1}{t+2m}\zeta_{2m}^s, \tag{5}$$

and where $\delta_{2m,n} = 1$ if $n = 2m$ and $\delta_{2m,n} = 0$ otherwise. A derivation of these equations is given in Appendix A.

Equations (4) and (5) constitute a set of recurrence relations from which the solutions to the integral equation (1) may be built up. Table I shows values of the coefficients ζ_{2m}^n up to and including $n = 12$. It will be observed that the results agree with the values given by Bazer and Brown (1959), who give the expansion of $f_2(x)$ up to and including α^6. In Table II the coefficients ρ_t^s are given. As is shown in Appendix B, the ρ_t^s are useful in the computation of the transmission coefficient τ, the relations being:

$$\tau = \sum_{n=0}^{\infty} \alpha^{2n}\tau_{2n}, \tag{6}$$

$$\tau_{2n} = -4\beta \sum_{m=0}^{n} \frac{1}{(2m)!}\rho_{2m+1}^{2n-2m+1}. \tag{7}$$

The coefficients τ_{2n} were calculated up to and including $2n = 10$, and the values are shown in Table III. These results agree with Bazer and Brown, who give terms including τ_6.

TABLE IV

Comparison of the exact and power series values of τ

α	Exact	Power series	α	Exact	Power series
0	.8106	.81057	1.6	.883	.88480
0.2	.8118	.81184	1.8	.900	.90122
0.4	.8156	.81563	2.0	.917	.91777
0.6	.8219	.82191	2.2	.932	.93413
0.8	.8306	.83058	2.4	.945	.95066
1.0	.8415	.84150	2.6	.958	.96895
1.2	.854	.85442	2.8	.968	.99297
1.4	.868	.86905	3.0	.976	1.03061

A comparison of the power series with the exact results is given in Table IV. The exact values were taken from Bouwkamp (1954, p. 84). It will be observed that 1% accuracy is attained up to $\alpha \simeq 2.5$.

ACKNOWLEDGMENTS

I wish to express my thanks to Peggy Steen for carefully checking the calculations in the paper, and to Dr. G. C. McCormick for reading the manuscript.

REFERENCES

BAZER, J. and BROWN, A. 1959. IRE Trans. on Antennas and Propagation, **AP-7**, S12.
BOUWKAMP, C. J. 1954. Repts. Progr. in Phys. **17**, 35.

APPENDIX A

DERIVATION OF THE RECURRENCE RELATIONS

If the power series representations of $\cosh \alpha x$, $\sinh \alpha(x-y)$, and $h(x)$ are employed in equation (1), one obtains

$$\text{(A.1)} \quad \sum_{n=0}^{\infty} \alpha^n h_n(x) = \sum_{n=0}^{\infty} \frac{(\alpha x)^{2n}}{(2n)!} + \beta \int_{-1}^{1} dy \sum_{m=0}^{\infty} \frac{\alpha^{2m+1}(x-y)^{2m}}{(2m+1)!} \sum_{p=0}^{\infty} \alpha^p h_p(y).$$

After rearrangement of the power series in (A.1), the powers of α may be equated throughout to give

$$\text{(A.2)} \quad h_n(x) = \gamma_n \frac{x^n}{n!} + \beta \int_{-1}^{1} dy \sum_{m=0}^{[(n-1)/2]} \frac{(x-y)^{2m} h_{n-2m-1}(y)}{(2m+1)!},$$

where $\gamma_n = 1$ if n is even, $\gamma_n = 0$ if n is odd. The binomial expansion

$$\text{(A.3)} \quad (x-y)^p = (-)^p \sum_{q=0}^{p} (-x)^{p-q} y^q \binom{p}{q},$$

along with equation (3), is introduced into equation (A.2):

$$\text{(A.4)} \quad \sum_{m=0}^{[n/2]} \zeta_{2m}^n x^{2m} = \frac{\gamma_n x^n}{n!} + \beta \sum_{m=0}^{[(n-1)/2]} \frac{1}{(2m+1)!} \sum_{p=0}^{[(n-2m-1)/2]} \zeta_{2p}^{n-2m-1} \int_{-1}^{1} dy \sum_{q=0}^{2m} \binom{2m}{q} y^{2p+q} (-x)^{2m-q}.$$

The integration with respect to y is now carried out. Note that odd powers of y vanish upon integration. The result is

$$\text{(A.5)} \quad \sum_{m=0}^{[n/2]} \zeta_{2m}^n x^{2m} = \frac{\gamma_n x^n}{n!} + 2\beta \sum_{m=0}^{[(n-1)/2]} \frac{1}{(2m+1)!} \sum_{p=0}^{[(n-2m-1)/2]} \zeta_{2p}^{n-2m-1} \sum_{q=0}^{m} \binom{2m}{2q} \frac{x^{2m-2q}}{2p+2q+1}.$$

The abbreviation

$$\text{(A.6)} \quad \rho_t^s = \sum_{n=0}^{[s/2]} \frac{1}{t+2n} \zeta_{2n}^s$$

is put into equation (A.5), with the result

$$\text{(A.7)}\quad \sum_{m=0}^{[n/2]} \zeta_{2m}^{n} x^{2m} = \frac{\gamma_n x^n}{n!} + 2\beta \sum_{m=0}^{[(n-1)/2]} \frac{1}{(2m+1)!} \sum_{q=0}^{m} \binom{2m}{2q} \rho_{2q+1}^{n-2m-1} x^{2m-2q}.$$

The substitution $p = m-q$ reduces the above equation to

$$\text{(A.8)}\quad \sum_{m=0}^{[n/2]} \zeta_{2m}^{n} x^{2m} = \frac{\gamma_n x^n}{n!} + 2\beta \sum_{m=0}^{[(n-1)/2]} \frac{1}{(2m+1)!} \sum_{p=0}^{m} \binom{2m}{2p} \rho_{2m-2p+1}^{n-2m-1} x^{2p}.$$

If like powers of x are equated, one finds

$$\text{(A.9)}\quad \zeta_{2p}^{n} = \frac{x^n \delta_{2p,n}}{n!} + 2\beta \sum_{m=p}^{[(n-1)/2]} \binom{2m}{2p} \frac{1}{(2m+1)!} \rho_{2m-2p+1}^{n-2m-1}.$$

This is the desired formula.

APPENDIX B

The Formula for τ_{2n}

The transmission coefficient τ is defined by

$$\text{(B.1)}\quad \tau = -(2/a\alpha)\,\mathrm{Im}[A(0)],$$

where $A(0)$ is the amplitude of the far field,

$$\text{(B.2)}\quad A(0) = \frac{a}{\pi} \int_{-1}^{1} \cosh \alpha x\, h(x)\, dx.$$

Thus, from equation (6) one has

$$\text{(B.3)}\quad \sum_{n=0}^{\infty} \alpha^{2n} \tau_{2n} = -\frac{2}{\pi\alpha} \int_{-1}^{1} \cosh \alpha x\, \mathrm{Im}[h(x)]\, dx.$$

Since $h_0(x) = 1$ it is easy to see from equation (A.2) that $h_n(x)$ is imaginary only when n is odd. This being the case, one has

$$\text{(B.4)}\quad \sum_{n=0}^{\infty} \alpha^{2n} \tau_{2n} = -\frac{2}{\pi} \int_{-1}^{1} dx \sum_{m=0}^{\infty} \frac{(\alpha x)^{2m}}{(2m)!} \sum_{p=0}^{\infty} \alpha^{2p}\, \mathrm{Im}[h_{2p+1}(x)].$$

When the sums in (B.4) are rearranged, and like powers of α are equated, it is found that

$$\text{(B.5)}\quad \tau_{2n} = -\frac{2}{\pi} \int_{-1}^{1} dx \sum_{p=0}^{n} \frac{x^{2n-2p}}{(2n-2p)!}\, \mathrm{Im}[h_{2p+1}(x)].$$

But

$$\text{(B.6)}\quad \mathrm{Im}[h_{2p+1}(x)] = -i \sum_{q=0}^{p} \zeta_{2q}^{2p+1} x^{2q}.$$

Putting (B.6) into equation (B.5), rearranging the series, and integrating gives the result

$$\text{(B.7)}\quad \tau_{2n} = \frac{4i}{\pi} \sum_{p=0}^{n} \frac{1}{(2n-2p)!}\, \rho_{2n-2p+1}^{2p+1}.$$

With the substitution $m = n-p$, one now obtains the desired formula equation (7).

ESTIMATION OF THE EFFECT OF SURFACE ON THE DIPOLAR BROADENING OF MAGNETIC RESONANCE LINES IN CRYSTALS*

G. C. BENSON AND P. BALK†

The broadening of the nuclear magnetic absorption lines of a crystalline powder by dipolar interaction should depend on the state of subdivision of the material since the interactions of nuclei in surface regions differ from those of nuclei far removed from the surface. The present note provides a simple method of estimating the order of magnitude of this surface effect.

In the following consideration, it is assumed that the crystalline powder is an ionic solid having a NaCl structure in which the distance between nearest neighbors is equal to a. The sample contains N positive ions and the same number of negative ions; n pairs of these ions lie in the crystal faces which are assumed to be of the {100} type. It is further assumed that the lattice structure is rigid and perfect throughout the individual particles of the powder and that although (n/N), the fraction of the ions located in surfaces, may be significant, the crystals are not small enough for other structural features (edges etc.) to be important. If the powder has a specific surface, $A(\mathrm{m^2\,g^{-1}})$, it can be shown that

$$n = 10^4\, a\, \rho\, AN \tag{1}$$

where ρ (g cm^{-3}) is the density of the crystalline material.

The second moment, S_2, of the line associated with transitions between states of the positive ion with different nuclear spin is given by van Vleck's formula (van Vleck 1948), which in the present case can be written

$$S_2 = N^{-1}\mu_0^2\left[\frac{6}{5}\, I_+(I_++1)g_+^2\sum_{++} r_{ij}^{-6}+\frac{4}{15}\, I_-(I_-+1)g_-^2\sum_{+-} r_{ij}^{-6}\right]. \tag{2}$$

In this equation μ_0 is the value of the nuclear magneton; I and g denote, respectively, the nuclear spin number and gyromagnetic ratio of the ionic species indicated by the subscript + or −. The distance between two nuclei i and j is r_{ij}. The first sum in equation (2) is taken over all possible pairs of positive ions; the second sum is over all pairs of unlike ions. These sums are closely related to other sums occurring in calculations of the cohesive energy and the surface energy of the crystal, thus

$$\sum_{++} r_{ij}^{-6} = a^{-6}\tfrac{1}{2}[NA_6''-nB_6''] \tag{3}$$

*Issued as N.R.C. No. 6329.

†National Research Council of Canada Postdoctorate Fellow 1956–58. Present address: International Business Machines Corporation, Research Center, Yorktown, New York.

and

$$\sum_{+-} r_{ij}^{-6} = a^{-6}[NA_6' - nB_6'] \tag{4}$$

where A_6' and A_6'' have been evaluated by Jones and Ingham (1925) and B_6' and B_6'' by van Zeggeren and Benson (1957).

Combining equations (1) to (4), the second moment can be written in the form

$$S_2 = S_2^0 + \Delta S_2 \tag{5}$$

where

$$S_2^0 = a^{-6}\mu_0^2\left[\frac{3}{5} I_+(I_+ + 1)g_+^2 A_6'' + \frac{4}{15} I_-(I_- + 1)g_-^2 A_6'\right] \tag{6}$$

and

$$\Delta S_2 = -10^4 a^{-5}\mu_0^2 \rho A\left[\frac{3}{5} I_+(I_+ + 1)g_+^2 B_6'' + \frac{4}{15} I_-(I_- + 1)g_-^2 B_6'\right]. \tag{7}$$

The negative sign in equation (7) indicates that the line is narrowed by increasing the specific surface of the sample.

In the case of NaCl itself $a = 2.820 \times 10^{-8}$ cm and taking the other necessary data from a review article by Pake (1956) it follows that

$$S_2(\text{NaCl}) = 0.542 - 1.17 \times 10^{-4} A \text{ gauss}^2. \tag{8}$$

The value of S_2^0 in this equation is very close to the experimental results obtained by Otsuka, Oshio, Kobayashi, and Kawamura (1959) with a single crystal of NaCl oriented in two different ways in the external magnetic field. For a powder with a specific surface of 100 $m^2\ g^{-1}$, the present theory predicts a decrease in the second moment of about 2%. This change is of the same order as the experimental error in current line width determinations. Hence it appears that such a surface effect would not be detectable until the specific surface of the sample exceeded 100 $m^2\ g^{-1}$; this means that individual particles would contain less than 10^5 molecules.

Recent theoretical studies of the configuration in the surface region of an ionic crystal have shown that the equilibrium positions of the ions in this region differ slightly from the regular lattice sites. Thus a refinement of the present treatment is to correct ΔS_2 for this lattice distortion. Adopting the one-layer model examined by Benson, Balk, and White (1959) and using the same notation as these authors, the effect of surface distortion is to add a correction

$$\Delta S_2' = 10^4 a^{-5}\mu_0^2 \rho A\left[\frac{6}{5} I_+(I_+ + 1)g_+^2\left\{\sum_p^4 G_p[6]z_+^p\right\} + \frac{4}{15} I_-(I_- + 1)g_-^2\left\{\sum_p^4 U_p[6](z_+^p + z_-^p) + \sum_p^2 u_{2p}[6](z_- - z_+)^p\right\}\right] \tag{9}$$

to ΔS_2. After substituting numerical values for NaCl, taken from the preceding reference, equation (9) gives

$$\Delta S_2' = 0.447 \times 10^{-4} A \text{ gauss}^2. \tag{10}$$

This correction tends to decrease the surface effect estimated previously. It may be concluded that if any surface effect is observed in cubic crystals it must be due to interactions of other than a dipolar nature.

All the calculations in this note have been described with specific reference to the NaCl structure but other crystal types could be treated in a similar way. There is, however, no reason to expect that the dipolar surface effect would be appreciably different in magnitude for other structures.

BENSON, G. C., BALK, P., and WHITE, P. 1959. J. Chem. Phys. **31**, 109.
JONES, J. E. and INGHAM, A. E. 1925. Proc. Roy. Soc. (London), A, **107**, 636.
OTSUKA, E., OSHIO, Y., KOBAYASHI, T., and KAWAMURA, H. 1959. J. Phys. Soc. Japan, **14**, 1454.
PAKE, G. E. 1956. Solid State Phys. **2**, 1.
VAN VLECK, J. H. 1948. Phys. Rev. **74**, 1168.
VAN ZEGGEREN, F. and BENSON, G. C. 1957. J. Chem. Phys. **26**, 1077.

RECEIVED MARCH 8, 1961.
DIVISION OF PURE CHEMISTRY,
NATIONAL RESEARCH COUNCIL,
OTTAWA, CANADA.

ANGULAR VARIATION OF AXIAL SPIN-HAMILTONIAN EIGENVALUES IN STRONG MAGNETIC FIELD

H. A. BUCKMASTER

Tables of eigenvalues and matrix elements of transition probabilities are required in the design of those solid-state masers which are based on the three-energy-level scheme proposed by Bloembergen (1956). Chromium-doped ruby has been widely exploited as the active material in masers because of the simplicity of its energy level scheme, its chemical stability, its high thermal conductivity, and the ease with which it may be machined. It is not surprising that the above-mentioned tables have been calculated for chromium in ruby, i.e., for $S = 3/2$ in an axial crystalline electric field by Weber (1959), Schulz-Du Bois (1959), and Stahl-Brada and Low (1960). More extensive tables will be required when other satisfactory active materials for masers are found. Such tables are also useful whenever it is necessary to locate magnetic-resonance fine-structure transitions corresponding to $\Delta M = \pm 1, \pm 2, \pm 3$, etc. where M is the strong magnetic field quantum number. This is particularly true when the applied external magnetic field **B** is at an arbitrary orientation to the symmetry axis of the crystalline electric field. It is convenient to describe the orientation of **B** with respect to the symmetry axis (z-axis) by the spherical

co-ordinates (θ, ϕ). The eigenvalues of an axial spin-Hamiltonian for arbitrary spin with the external magnetic field at an arbitrary orientation with respect to the symmetry axis can be expressed in a closed form when the external magnetic field is large compared to the splittings due to the crystalline electric field. The terms in these expressions, involving the spin S and the components of S_z, can be tabulated for the commonest values of S facilitating the calculation of the eigenvalues.

The axial spin-Hamiltonian has the form

$$(1) \qquad \mathscr{H} = g_{\parallel}\beta B_z S_z + g_{\perp}\beta(B_x S_x + B_y S_y) + D[S_z^2 - \tfrac{1}{3}S(S+1)]$$

where the symbols are in accordance with convention. It is convenient, in strong magnetic fields, to choose a new set of axes such that the Zeeman splitting term is diagonalized. This is equivalent to defining a new term in g oriented at an angle ψ to the z-axis and defined by

$$\cos\psi = (g_{\parallel}/g)\cos\theta \qquad \sin\psi = (g_{\perp}/g)\sin\theta$$

when the external magnetic field $\mathbf{B}$ is oriented in the xz plane ($\phi = 0°$) at an angle θ to the z-axis, and by

$$\cos\psi = (g_{\parallel}/g)\cos\theta \qquad \sin\psi = -(g_{\perp}/g)\sin\theta$$

when $\mathbf{B}$ is oriented in the yz plane ($\phi = \pi/2$) at an angle θ to the z-axis where

$$g^2 = g_{\parallel}^2\cos^2\theta + g_{\perp}^2\sin^2\theta.$$

Right-handed rotation transforms (1) into

$$(2) \qquad \mathscr{H} = g\beta B S_w + D\left[S_w^2\left(\frac{g_{\parallel}}{g}\right)^2\cos^2\theta + S_u^2\left(\frac{g_{\perp}}{g}\right)^2\sin^2\theta - \left(\frac{g_{\parallel}g_{\perp}}{g^2}\right)^2\sin\theta\cos\theta(S_u S_w + S_w S_u) - \tfrac{1}{3}S(S+1)\right]$$

in the xz plane where $(S_x, S_z) \rightarrow (S_u, S_w)$ and

$$(3) \qquad \mathscr{H} = g\beta B S_w + D\left[S_w^2\left(\frac{g_{\parallel}}{g}\right)^2\cos^2\theta + S_v^2\left(\frac{g_{\perp}}{g}\right)^2\sin^2\theta - \left(\frac{g_{\parallel}g_{\perp}}{g^2}\right)^2\sin\theta\cos\theta(S_v S_w + S_w S_v) - \tfrac{1}{3}S(S+1)\right]$$

in the yz plane where $(S_y, S_z) \rightarrow (S_v, S_w)$. It is then found by second-order perturbation calculations that both spin-Hamiltonians yield

$$(4) \quad E_M = g\beta B M + \frac{D}{2}\left[3\left(\frac{g_{\parallel}}{g}\right)^2\cos^2\theta - 1\right]\cdot[M^2 - \tfrac{1}{3}S(S+1)] - D^2\cdot\left(\frac{g_{\parallel}g_{\perp}}{g^2}\right)^2\cdot\sin^2\theta\cos^2\theta\left(\frac{M}{2G}\right)\cdot[4S(S+1) - 8M^2 - 1] + D^2\cdot\left(\frac{g_{\perp}}{g}\right)^4\cdot\sin^4\theta\left(\frac{M}{8G}\right)\cdot[2S(S+1) - 2M^2 - 1]^*$$

if $G \gg D$, where $S_w = M, M-1, \ldots, -M+1, -M$ and $G = g\beta B_0 = h\nu$ is the energy of the Zeeman splitting of the ground state in the absence of a crystalline electric field.

The general expression for the energies of transitions between levels with strong field quantum number M and $M-m$, i.e., $\Delta M = \pm m$ is

$$(5)\quad E_M - E_{M-m} = g\beta Bm + \frac{D}{2}\cdot\left[3\left(\frac{g_\parallel}{g}\right)^2\cos^2\theta - 1\right][m(2M-m)]$$

$$-D^2\cdot\left(\frac{g_\parallel g_\perp}{g^2}\right)^2\cdot\sin^2\theta\cos^2\theta\cdot\left(\frac{m}{2G}\right)\cdot[4S(S+1)-24M(M-m)-8m^2-1]$$

$$+D^2\cdot\left(\frac{g_\perp}{g}\right)^4\cdot\sin^4\theta\cdot\left(\frac{m}{8G}\right)\cdot[2S(S+1)-6M(M-m)-2m^2-1]$$

which becomes for

(*a*) $M \leftrightarrow M-1$, i.e. $\Delta M = \pm 1$

$$(6)\quad E_M - E_{M-1} = g\beta B + D(M-1/2)\cdot\left[3\left(\frac{g_\parallel}{g}\right)^2\cos^2\theta - 1\right]$$

$$-D^2\cdot\left(\frac{g_\parallel g_\perp}{g^2}\right)^2\cdot\sin^2\theta\cos^2\theta\cdot\left(\frac{1}{2G}\right)\cdot[4S(S+1)-24M(M-1)-9]$$

$$+D^2\cdot\left(\frac{g_\perp}{g}\right)^4\cdot\sin^4\theta\cdot\left(\frac{1}{8G}\right)\cdot[2S(S+1)-6M(M-1)-3].$$

(*b*) $M \leftrightarrow M-2$, i.e. $\Delta M = \pm 2$

$$(7)\quad E_M - E_{M-2} = 2g\beta B + 2D(M-1)\cdot\left[3\left(\frac{g_\parallel}{g}\right)^2\cos^2\theta - 1\right]$$

$$-D^2\cdot\left(\frac{g_\parallel g_\perp}{g^2}\right)^2\cdot\sin^2\theta\cos^2\theta\cdot\left(\frac{2}{2G}\right)\cdot[4S(S+1)-24M(M-2)-33]$$

$$+D^2\cdot\left(\frac{g_\perp}{g}\right)^4\cdot\sin^4\theta\cdot\left(\frac{2}{8G}\right)\cdot[2S(S+1)-6M(M-2)-9].*$$

(*c*) $M \leftrightarrow M-3$, i.e. $\Delta M = \pm 3$

$$(8)\quad E_M - E_{M-3} = 3g\beta B + 3D(M-3/2)\cdot\left[3\left(\frac{g_\parallel}{g}\right)^2\cos^2\theta - 1\right]$$

$$-D^2\cdot\left(\frac{g_\parallel g_\perp}{g^2}\right)^2\cdot\sin^2\theta\cos^2\theta\cdot\left(\frac{3}{2G}\right)\cdot[4S(S+1)-24M(M-3)-73]$$

$$+D^2\cdot\left(\frac{g_\perp}{g}\right)^4\cdot\sin^4\theta\cdot\left(\frac{3}{8G}\right)\cdot[2S(S+1)-6M(M-3)-19].$$

*These expressions are the corrected forms of equation (9.7) of Low (1960) and equation (5) of Bleaney (1951).

If the spin-Hamiltonian contains a term corresponding to the angular momentum operator $O_6^6 \equiv (S_+^6 + S_-^6)$, which has the same transformation properties as the spherical harmonic Y_{60}, then, if $S \geq 3$, transitions corresponding to $\Delta M = \pm 6$ are allowed.

TABLE I*a*

$[4S(S+1)-24M(M-1)-9]$

		S							
M		1/2	3/2	5/2	7/2	9/2	11/2	13/2	15/2
+15/2,	−13/2								−924
+13/2,	−11/2							−672	−612
+11/2,	−9/2						−460	−408	−348
+9/2,	−7/2					−288	−244	−192	−132
+7/2,	−5/2				−156	−120	−76	−24	+36
+5/2,	−3/2			−64	−36	0	+44	+96	+156
+3/2,	−1/2		−12	+8	+36	+72	+116	+168	+228
+1/2,	+1/2	0	+12	+32	+60	+96	+140	+192	+252
		1	2	3	4	5	6	7	8
+8,	−7								−1065
+7,	−6							−793	−729
+6,	−5						−561	−505	−441
+5,	−4					−369	−321	−265	−201
+4,	−3				−217	−177	−129	−73	−9
+3,	−2			−105	−73	−33	+15	+71	+135
+2,	−1		−33	−9	+23	+63	+111	+167	+231
+1,	0	−1	+15	+39	+71	+111	+159	+215	+279

TABLE I*b*

$[2S(S+1)-6M(M-1)-3]$

		S							
M		1/2	3/2	5/2	7/2	9/2	11/2	13/2	15/2
+15/2,	−13/2								−168
+13/2,	−11/2							−120	−90
+11/2,	−9/2						−80	−54	−24
+9/2,	−7/2					−48	−26	0	+30
+7/2,	−5/2				−24	−6	+16	+42	+72
+5/2,	−3/2			−8	+6	+24	+46	+72	+102
+3/2,	−1/2		0	+10	+24	+42	+64	+90	+120
+1/2,	+1/2	0	+6	+16	+30	+48	+70	+96	+126
		1	2	3	4	5	6	7	8
+8,	−7								−195
+7,	−6							−143	−111
+6,	−5						−99	−71	−39
+5,	−4					−63	−39	−11	+21
+4,	−3				−35	−15	+9	+37	+69
+3,	−2			−15	+1	+21	+45	+73	+105
+2,	−1		−3	+9	+25	+45	+69	+97	+129
+1,	0	+1	+9	+21	+37	+57	+81	+109	+141

$$(9)\quad E_M - E_{M-6} = 6g\beta B + 6D(M-3)\left[3\left(\frac{g_\parallel}{g}\right)^2\cos^2\theta - 1\right]$$

$$-D^2\left(\frac{g_\parallel g_\perp}{g^2}\right)^2\sin^2\theta\cos^2\theta\left(\frac{6}{2G}\right)[4S(S+1)-24M(M-6)-289]$$

$$+D^2\left(\frac{g_\perp}{g}\right)^4\sin^4\theta\left(\frac{6}{8G}\right)[2S(S+1)-6M(M-6)-73].$$

TABLE II*a*

$[4S(S+1)-24M(M-2)-33]$

		S							
M		1/2	3/2	5/2	7/2	9/2	11/2	13/2	15/2
+15/2,	−11/2								−768
+13/2,	−9/2							−540	−480
+11/2,	−7/2						−352	−300	−240
+9/2,	−5/2					−204	−160	−108	−48
+7/2,	−3/2				−96	−60	−16	+36	+96
+5/2,	−1/2			−28	0	+36	+80	+132	+192
+3/2,	+1/2		0	+20	+48	+84	+128	+180	+240
		1	2	3	4	5	6	7	8
+8,	−6								−897
+7,	−5							−649	−585
+6,	−4						−441	−385	−321
+5,	−3					−273	−225	−169	−105
+4,	−2				−145	−105	−57	−1	+63
+3,	−1			−57	−25	+15	+63	+119	+183
+2,	0		−9	+15	+47	+87	+135	+191	+255
+1,	+1	−1	+15	+39	+71	+111	+159	+215	+279

TABLE II*b*

$[2S(S+1)-6M(M-2)-9]$

		S							
M		1/2	3/2	5/2	7/2	9/2	11/2	13/2	15/2
+15/2,	−11/2								−129
+13/2,	−9/2							−87	−57
+11/2,	−7/2						−53	−27	+3
+9/2,	−5/2					−27	−5	+21	+51
+7/2,	−3/2				−9	+9	+31	+57	+87
+5/2,	−1/2			+1	+15	+33	+55	+81	+111
+3/2,	+1/2		+3	+13	+27	+45	+67	+93	+123
		1	2	3	4	5	6	7	8
+8,	−6								−153
+7,	−5							−107	−75
+6,	−4						−69	−41	−9
+5,	−3					−39	−15	+13	+45
+4,	−2				−17	+3	+27	+55	+87
+3,	−1			−3	+13	+33	+57	+85	+117
+2,	0		+3	+15	+31	+51	+75	+103	+135
+1,	+1	+1	+9	+21	+37	+57	+81	+109	+141

Equations (7), (8), and (9) are useful expressions in the approximate analysis of the data for the angular spectrum of the $\Delta M = \pm 2$, ± 3, and ± 6 transitions observed in dilute gadolinium ethyl sulphate by Buckmaster (1956*a*, *b*). No attempt has been made to find expressions in closed form for the transition probabilities when the magnetic field is arbitrarily oriented with respect to the crystal axis. In general, the intensity of the $\Delta M = \pm 2$ and ± 3 transitions are weaker than that of the $\Delta M = \pm 1$ transitions by a factor of $(D/B)^2$ and $(D/B)^4$ respectively and vanish only if the external magnetic field is parallel to the crystal axis.

Tables I to IV give the values of the terms involving only S and M that appear in equations (6), (7), (8), and (9) for the commonest values of S.

TABLE III*a*

$[4S(S+1)-24M(M-3)-73]$

		S							
M		1/2	3/2	5/2	7/2	9/2	11/2	13/2	15/2
+15/2,	−9/2								−628
+13/2,	−7/2							−424	−364
+11/2,	−5/2						−260	−208	−148
+9/2,	−3/2					−136	−92	−40	+20
+7/2,	−1/2				−52	−16	+28	+80	+140
+5/2,	+1/2			−8	+20	+56	+100	+152	+212
+3/2,	+3/2		−4	+16	+44	+80	+124	+176	+236
		1	2	3	4	5	6	7	8
+8,	−5								−745
+7,	−4							−521	−457
+6,	−3						−337	−281	−217
+5,	−2					−193	−145	−89	−25
+4,	−1				−89	−49	−1	+55	+119
+3,	0			−25	+7	+47	+95	+151	+215
+2,	+1		−1	+23	+55	+95	+143	+199	+263

TABLE III*b*

$[2S(S+1)-6M(M-3)-19]$

		S							
M		1/2	3/2	5/2	7/2	9/2	11/2	13/2	15/2
+15/2,	−9/2								−94
+13/2,	−7/2							−58	−28
+11/2,	−5/2						−30	−4	+26
+9/2,	−3/2					−10	+12	+38	+68
+7/2,	−1/2				+2	+20	+42	+68	+98
+5/2,	+1/2			+6	+20	+38	+60	+86	+116
+3/2,	+3/2		+2	+12	+26	+44	+66	+92	+122
		1	2	3	4	5	6	7	8
+8,	−5								−115
+7,	−4							−75	−43
+6,	−3						−43	−15	+17
+5,	−2					−19	+5	+33	+65
+4,	−1				−3	+17	+41	+69	+101
+3,	0			+5	+21	+41	+65	+93	+125
+2,	+1		+5	+17	+33	+53	+77	+105	+137

TABLE IV*a*

$[4S(S+1)-24M(M-6)-289]$

		S							
M		1/2	3/2	5/2	7/2	9/2	11/2	13/2	15/2
+15/2,	−3/2								−304
+13/2,	−1/2							−172	−112
+11/2,	+1/2						−80	−28	+32
+9/2,	+3/2					−28	+16	+68	+128
+7/2,	+5/2				−16	+20	+64	+116	+176
		1	2	3	4	5	6	7	8
+8,	−2								−385
+7,	−1							−233	−169
+6,	0						−121	−65	−1
+5,	+1					−49	−1	+55	+119
+4,	+2				−17	+23	+71	+127	+191
+3,	+3			−25	+7	+47	+95	+151	+215

TABLE IV*b*

$[2S(S+1)-6M(M-6)-73]$

		S							
M		1/2	3/2	5/2	7/2	9/2	11/2	13/2	15/2
+15/2,	−3/2								−13
+13/2,	−1/2							+5	+35
+11/2,	+1/2						+15	+41	+71
+9/2,	+3/2					+17	+39	+65	+95
+7/2,	+5/2				+11	+29	+51	+77	+107
		1	2	3	4	5	6	7	8
+8,	−2								−25
+7,	−1							−3	+29
+6,	0						+11	+39	+71
+5,	+1					+17	+41	+69	+101
+4,	+2				+15	+35	+59	+87	+119
+3,	+3			+5	+21	+41	+65	+93	+125

The author wishes to acknowledge the financial support of the National Research Council of Canada and the University of Alberta.

BLEANEY, B. 1951. Phil. Mag. Ser. 7, **42**, 441.
BLOEMBERGEN, N. 1956. Phys. Rev. **104**, 324.
BUCKMASTER, H. A. 1956*a*. Can. J. Phys. **34**, 150.
——— 1956*b*. Can. J. Phys. **34**, 341.
LOW, W. 1960. Paramagnetic resonance in solids, Suppl. 2, Advances in solid state physics, (Academic Press, N.Y.).
SCHULZ-DU BOIS, E. O. 1959. Bell System Tech. J. **33**, 271.
STAHL-BRADA, R. and LOW, W. 1960. Nuovo Cimento (10), **15**, Suppl. No. 3, 290.
WEBER, J. 1959. Revs. Modern Phys. **31**, 681.

RECEIVED JANUARY 5, 1961.
DEPARTMENT OF PHYSICS,
UNIVERSITY OF ALBERTA, CALGARY,
CALGARY, ALBERTA.

THE 1.2-MEV BETA DECAY OF I^{128}

K. G. McNeill and J. D. Prentice

The decay scheme of I^{128} has been extensively studied by both beta- and gamma-ray spectroscopy (for example, Benczer *et al.* 1956; Gupta and Jha 1956; Wapstra *et al.* 1953). The Kurie plot of the beta spectrum obtained by Benczer *et al.* (1956) showed the presence of three components. By subtraction, the end-point energies and relative intensities of the two highest-energy groups were established and the presence of a weak lower-energy group (β_3) was indicated. Owing to the inherent inaccuracy of the successive subtractions neither the end point nor the shape of the Kurie plot for β_3 could be obtained. By subtracting from the end-point energy of the ground-state beta spectrum ($E_{\beta_1} = 2.12$ Mev) the measured energy (0.98 Mev) of the gamma ray from the second excited state of Xe^{128}, they derived a value of 1.14 Mev for the maximum energy of β_3.

By observing the beta spectrum in coincidence with the 0.98-Mev gamma ray the present authors have confirmed the proposed decay scheme and have measured the end-point energy and spectrum shape of β_3 directly.

A NaI (Tl) crystal, irradiated with neutrons, was used as both source and detector for the beta particles thus providing a zero thickness source and eliminating self-absorption, counter window, and scattering corrections. A 1 in. diameter by 1 in. long NaI crystal was irradiated for 40 minutes in a water tank surrounding a Sb–Be neutron source. It was partially shielded from the gamma rays from the source by a 1-in. thickness of lead which served to reduce sufficiently the long term phosphorescence which otherwise appeared. After irradiation the crystal was mounted on a DuMont 6292 photomultiplier connected by conventional electronics to a 100-channel pulse-height analyzer (100 PHA). A $1\frac{3}{4}$ in. diameter by 2 in. long NaI (Tl) crystal was placed near the irradiated one to detect the emergent gamma rays from the latter. The output from the second detector was analyzed by a single-channel analyzer set to accept pulses from the photopeak of the 0.98-Mev gamma ray emitted by the second excited state of the daughter nucleus, Xe^{128}. The output from this analyzer gated the 100 PHA so that the latter only accepted pulses, in the irradiated crystal, in coincidence with 0.98-Mev gamma rays. As separate gamma–gamma coincidence experiments with an I^{128} source showed that no other gamma rays were in coincidence with those at 0.98 Mev, the spectrum obtained from the 100 PHA, after suitable correction, was the spectrum of the beta particles emitted in the transition from the ground state of I^{128} to the second excited state of Xe^{128}. Corrections were applied for random coincidences between the 0.98-Mev gamma rays and beta particles from the higher-energy branches of the beta decay and also for true coincidences due to the decay of Na^{24} produced by the irradiation. Pulses from the Compton distribution of the higher-energy gamma rays

emitted by Mg^{24} following the beta decay of Na^{24} could appear in the 0.98-Mev gate and cause spurious real coincidences. The Na^{24} has, however, a half life of 15 hours and for this reason and because the capture cross section of Na^{23} for neutrons is small, the Na^{24} activity was weak. The long half life also permitted an experimental correction to be made for the Na^{24} contribution by observing its spectrum after the I^{128} had decayed away.

The Kurie plot of the spectrum finally obtained is shown in Fig. 1. It is seen to have a straight-line shape and to intercept the energy axis at 1.20 Mev. The estimated error in this result is ± 0.05 Mev and is largely caused by statistical errors in the counts obtained.

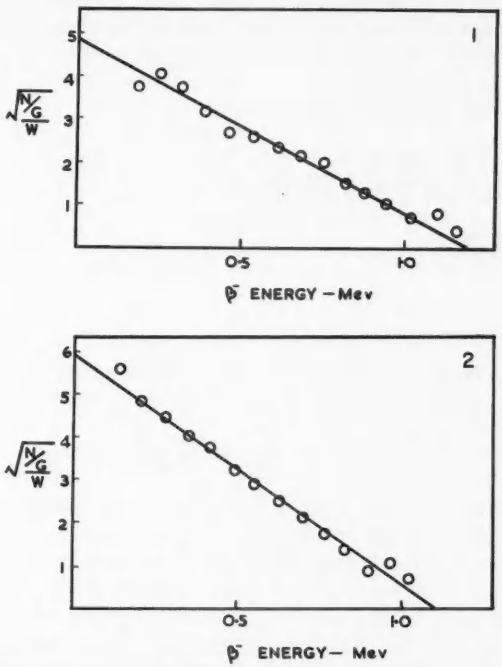

FIG. 1. The beta spectrum of I^{128} in coincidence with 0.98-Mev gamma rays. N = number of beta particles per channel. G = modified Fermi function = $(p/W)F$. W = total energy of beta particles in units of mc^2.

FIG. 2. The beta spectrum in coincidence with 0.54-Mev gamma rays.

A similar experiment with the gamma-ray gate set on the 0.54-Mev cascade transition from the second to the first excited states of Xe^{128} yielded a straight-line shape and a value of 1.13 ± 0.04 Mev (Fig. 2). We, therefore, conclude that the best value for the end-point energy of β_3 is 1.16 ± 0.05 Mev and that the spectrum shape is consistent with its being an allowed transition. This value agrees with the value of 1.14 ± 0.02 Mev deduced by Benczer *et al.* (1956) and together with their result that 2% of all transitions proceed

by this branch leads to a log *ft* value of 6.6. The shape and log *ft* value suggest an allowed transition and tend to confirm the 1^+ and 2^+ assignments for the ground state of I^{128} and second excited state of Xe^{128} respectively.

In connection with the usefulness of the experimental technique of making the source in the crystal it is perhaps of interest to note that it was also possible to confirm that a 0.75-Mev γ-ray observed in the gamma-ray spectrum belonged to a competing electron capture decay branch. In this case the Te *K* X rays following electron capture, absorbed in the radioactive crystal, were used to gate the spectrum of gamma rays detected in an external crystal. A gate set to accept the *K* X rays inevitably accepted many pulses from low-energy β-particles in coincidence with all the other gamma rays as well but when the gate was moved to either side of the X-ray peak the 0.75-Mev gamma ray disappeared, the remainder of the coincidence spectrum remaining unchanged. Thus the 0.75-Mev γ-ray was clearly shown to be in coincidence with Te *K* X rays but not with β-particles.

Benczer, N., Farrelly, B., Koerts, L., and Wu, C. S. 1956. Phys. Rev. **101**, 1027.
Gupta, R. K. and Jha, S. 1956. Nuclear Phys. **1**, 2.
Wapstra, A. H., Verster, N. F., and Boelhouwer, M. 1953. Physica, **19**, 138.

Received March 27, 1961.
Department of Physics,
University of Toronto,
Toronto, Ontario.

INELASTIC SCATTERING OF NEUTRONS FROM ROTATING LIQUID HELIUM II*

A. D. B. Woods

This note describes an attempt to see if macroscopic rotation of liquid helium II changes the character of the energy/momentum dispersion curve for the Landau excitations; no effect was observed. The excitations have been extensively studied in recent years using inelastic neutron scattering (Yarnell, Arnold, Bendt, and Kerr 1959; Palevsky, Otnes, and Larsson 1958; Henshaw 1958; and Henshaw and Woods 1960, 1961). The interesting properties of liquid helium II moving at high velocities (see, for example, Walmsley and Lane 1958 and Dowley and Hallett 1960) suggested that it might be desirable to determine whether the excitations, particularly those in the region of the roton minimum, are affected by rotation of the helium. In this experiment changes in either the energy of the scattered neutron group corresponding to an excitation near the roton minimum or in its width were looked for. An increase in width of the neutron group on rotation would imply enhanced roton/roton interaction and, hence, shorter roton lifetimes when the helium was rotating.

*Issued as A.E.C.L. No. 1262.

Accordingly the following experiment was performed. Neutrons with an initial wavelength of 4.06 Å were scattered from liquid helium through an angle of $81\frac{1}{4}°$ and the scattered neutrons were energy-analyzed using a time-of-flight rotating crystal spectrometer (Brockhouse 1960) at the Chalk River NRU reactor. The helium was in a chamber with an inside diameter of 2.6 in. which contained a bucket $2\frac{1}{4}$ in. in diameter. This bucket was rotated at a speed of 60 r.p.m. with the helium at a temperature of $1.5_4°$ K. At this temperature the roton line width is known to be perceptibly broadened (Larsson and Otnes 1959; Henshaw and Woods 1960), so that further increase on rotation should have been detectable. The runs lasted for almost 1 hour and rotation was begun about 15 minutes before counting.

The results obtained are shown in Fig. 1 where the counting rate per time

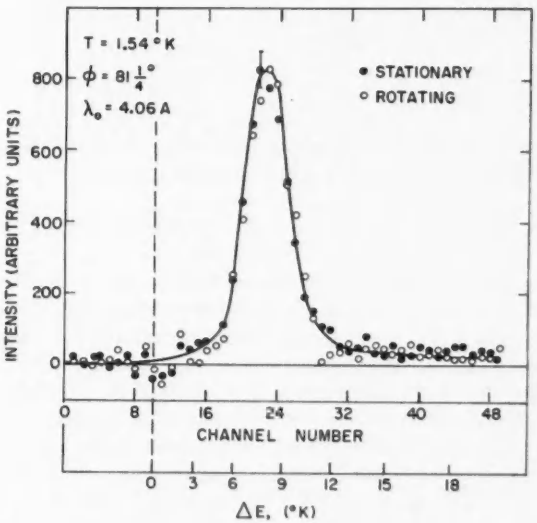

FIG. 1. Neutron groups observed for stationary and rotating conditions of inner bucket. The broken vertical line represents the position of zero energy transfer. The position of the peak corresponds to an excitation in the region of the roton minimum.

channel (with background scattering subtracted) is plotted for both the rotating and stationary conditions of the inner bucket. The scales have been adjusted so that the peak heights are equal. No significant difference between the patterns is observable. It is estimated that any shift in peak position is less than 0.3° K and any increase in width less than 0.5° K.

The author would like to thank Dr. D. G. Henshaw for the loan of the cryostat. Mr. E. A. Glaser and Mr. J. R. Freeborn gave valuable technical assistance.

BROCKHOUSE, B. N. 1960. Symposium on Inelastic Scattering of Neutrons in Solids and Liquids. Vienna, 11–14 October, 1960. Paper I/S18. Also issued as Chalk River Report CRNP 947.
DOWLEY, M. W. and HOLLIS HALLETT, A. C. 1960. Proceedings of the VIIth International Conference on Low Temperature Physics, *edited by* G. M. Graham and A. C. Hollis Hallett (University of Toronto Press, Toronto), p. 464.
HENSHAW, D. G. 1958. Phys. Rev. Letters, **1**, 127.
HENSHAW, D. G. and WOODS, A. D. B. 1960. Proceedings of the VIIth International Conference on Low Temperature Physics, *edited by* G. M. Graham and A. C. Hollis Hallett (University of Toronto Press, Toronto), p. 539.
——— 1961. Phys. Rev. **121**, 1266.
LARSSON, K. E. and OTNES, K. 1959. Arkiv Fysik, **15**, 49.
PALEVSKY, H., OTNES, K., and LARSSON, K. E. 1958. Phys. Rev. **112**, 11.
WALMSLEY, R. H. and LANE, C. T. 1958. Phys. Rev. **112**, 1041.
YARNELL, J. L., ARNOLD, G. P., BENDT, P. J., and KERR, E. C. 1959. Phys. Rev. **113**, 1379.

RECEIVED MARCH 29, 1961.
PHYSICS DIVISION,
ATOMIC ENERGY OF CANADA LIMITED,
CHALK RIVER, ONTARIO.

THE EFFECT OF DISSOLVED IRON ON THE THERMOELECTRICITY OF SILVER AT VERY LOW TEMPERATURES*

W. B. PEARSON AND I. M. TEMPLETON

Thermoelectric measurements made in this laboratory, as well as earlier measurements of Borelius *et al.* (1932) and Keesom and Matthijs (1935), show that iron causes a very large characteristic thermoelectric power at low temperatures (say $<10°$ K) when dissolved in very dilute concentration in Cu or Au. These "giant" thermoelectric powers may be as much as 1000 times larger than values predicted for diffusion thermoelectricity by the original Wilson theory (1936). No comparable measurements appear to have been made for Ag–Fe alloys, and indeed Hansen (1958) indicates that the solid solubility of Fe in Ag is very small. We have therefore prepared an Ag–Fe alloy wire which we quenched rapidly from 940° C by ejecting it forcibly from the annealing furnace into a bath of iced water. The wire had a residual resistance ratio of 75.8×10^{-3} indicating that some iron was indeed retained in solid solution by the quench. The absolute thermoelectric power of this alloy (Fig. 1) shows that iron also gives rise to a very large absolute thermoelectric power at low temperatures when dissolved in silver; furthermore, the alloy had a minimum in its electrical resistivity.

The low solid solubility of Fe in Ag, compared to that of Cu or Au, perhaps explains why it is relatively easy to obtain pure silver with a positive thermoelectric power at low temperatures. Both Pullan (1953) and Pearson (1960) report measurements on "pure" Ag whose positive absolute thermoelectric

*Issued as N.R.C. No. 6386.

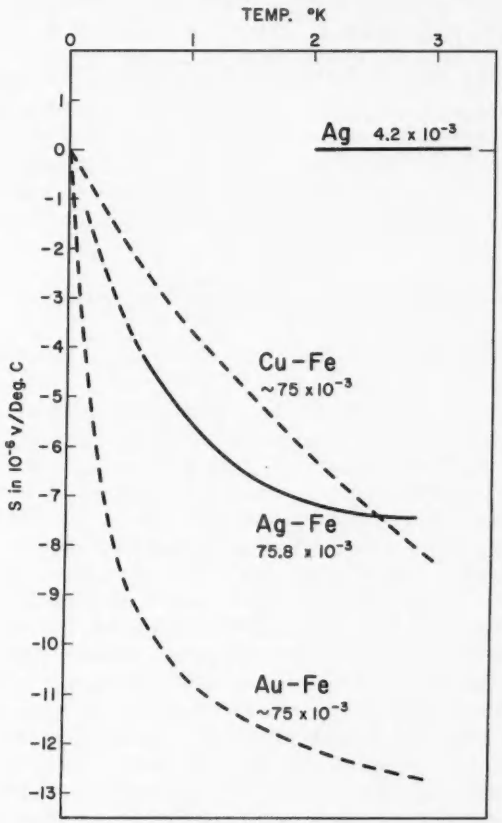

FIG. 1. Absolute thermoelectric power of Ag–Fe, Cu–Fe, and Au–Fe alloys and "pure" Tadanac Ag as a function of temperature. The figures give the residual resistance ratios, $R_{4.2°K}/(R_{296°K}-R_{4.2°K})$, for the alloys.

power increases with slightly less than the square of the absolute temperature in the temperature range from 2° to about 18° K. The sample of silver of Johnson, Matthey and Company reported to have, at very low temperatures, a small negative almost constant S (MacDonald *et al.* 1958) probably contained a trace of dissolved Fe, since the same silver also showed a minimum in its electrical resistivity (Pearson 1959).

We thank Mr. J. W. Fisher for preparing and heat-treating the Ag–Fe wire.

BORELIUS, G., KEESOM, W. H., JOHANSSON, C. H., and LINDE, J. O. 1932. Proc. Acad. Sci. Amsterdam, **35** (1), 15, 25.
HANSEN, M. 1958. Constitution of binary alloys (McGraw-Hill Book Co. Inc.), p. 20.
KEESOM, W. H. and MATTHIJS, C. J. 1935. Physica, **2**, 623.

MACDONALD, D. K. C., PEARSON, W. B., and TEMPLETON, I. M. 1958. Phil. Mag. **3**, 657.
PEARSON, W. B. 1959. Phil. Mag. **4**, 622.
——— 1960. Can. J. Phys. **38**, 1048.
PULLAN, G. T. 1953. Proc. Roy. Soc. A, **217**, 280.
WILSON, A. H. 1936. Theory of metals (Cambridge University Press).

RECEIVED APRIL 12, 1961.
DIVISION OF PURE PHYSICS,
NATIONAL RESEARCH COUNCIL,
OTTAWA, CANADA.

THE *K–LL* AUGER SPECTRUM OF $_{55}Cs^{133}$ *

R. L. GRAHAM, F. BROWN, G. T. EWAN, AND J. UHLER†

The measurements of the *K–LL* Auger lines reported here were made primarily to test the non-relativistic theory of Asaad and Burhop (1958) at the lowest value of the atomic number, Z, that has so far been studied with the Chalk River iron-free β-ray spectrometer (Graham *et al.* 1960). Discrepancies exist between the measured intensity ratios of the *K–LL* lines and the non-relativistic predictions but become smaller as Z decreases, as might be expected (Graham and Merritt 1961). Also the theoretical treatment suggests that there should be three satellite lines in addition to the six main lines of the *K–LL* Auger spectrum as a consequence of the nature of the coupling between the two final electronic L state vacancies. This coupling is expected to be close to a pure j–j coupling at high Z (six-line spectrum) and become intermediate between j–j and L–S coupling at lower Z (nine-line spectrum). The predictions suggest that the satellites should become more prominent and better separated from their partners at lower Z and hence more easily detected experimentally. In our experiments to date, at Z values $\geqslant 62$, it has been possible to detect in each case only one of the three predicted satellite lines. In this note we report measurements of the energies and intensities of the *K–LL* Auger lines at $Z = 55$. We again observe the K–L_1L_3 ($^3P_2$) satellite line and report preliminary experimental evidence for the other two satellite lines.

The source material, Xe^{133}, was prepared by neutron irradiation of natural Xe for 6 days in a neutron flux of 2.5×10^{14} cm^{-2} sec^{-1} in the NRU reactor. We are indebted to Dr. R. O. Kelly for supplying an iron capsule and for arranging the irradiation. An isotopically pure source of Xe^{133} was prepared using the newly installed mass separator (Brown *et al.* 1961). The Xe^{133} activity was confined to an area 20 mm$\times$1 mm by means of a defining slit through which passed about half the ions of mass 133. The ions were driven about 8 μg/cm^2 into an 800 μg/cm^2 aluminum-backing foil by virtue of their 30-kev kinetic energy (Davies 1961).

*Issued as A.E.C.L. No. 1264.
†Visitor from the Nobel Institute of Physics, Stockholm, Sweden.

For the measurements reported here, the spectrometer was adjusted to have an instrumental resolution of ~0.07% in momentum. Four sweeps of the spectrum were made using 100-second counting intervals. The net counting rate after subtraction of the γ background rate measured by a separate counter is shown in Fig. 1. The error bars indicate standard deviations of the gross counts at each current setting. The experimental line width of ~0.15% is mainly attributable to the straggling of electrons as they emerge through the aluminum foil from the penetration depth of the Xe atoms.

The energies and relative intensities are summarized in Table I. The relative

TABLE I

Energies and relative intensities of K–LL Auger lines in $_{55}Cs^{133}$

Transition	Line energy (kev)		Relative intensity		
	Theory[a]	Experiment	Theory[a]	Experiment	
$L_1L_1(^1S_0)$	24.34	24.39±0.02	1.00	1.00±0.06	
$L_1L_2(^1P_1)$	24.70	24.75±0.02	1.44	1.71±0.07	
$L_1L_2(^3P_0)$	24.73		0.05		
$L_2L_2(^1S_0)$	25.01	25.08±0.02	0.20	1.58±0.19	1.99±0.07
$L_1L_3(^3P_1)$	25.03		1.67		
$L_1L_3(^3P_2)$	25.08	25.14±0.03	0.24	0.42±0.19	
$L_2L_3(^1D_2)$	25.38	25.43±0.02	4.56	4.23±0.07	
$L_3L_3(^3P_0)$	25.67		0.22	1.91±0.06	
$L_3L_3(^3P_2)$	25.72	25.79±0.02	1.91		

[a]Asaad and Burhop (1958).

intensities were obtained from the line areas. For purposes of matching line shapes the net counting rates, after subtraction of the β-continuum rates, were plotted on a semilog scale in the manner discussed in earlier papers (see, for example, Graham *et al.* 1960). The K–$L_2L_3(^1D_2)$ line was used as the "standard" shape since it is most intense and is free from satellites. The shape of the intense K 80.99 internal conversion line shown at the right in Fig. 1 was also used as a guide in estimating the shape of the low-energy tails for each of the Auger lines which is not well determined statistically. The arrows in Fig. 1 show the positions of the six Auger lines and their three satellites as predicted by the formulae of Asaad and Burhop shifted ~50 ev to match the K–L_1L_1 and K–L_3L_3 peaks. The discrepancies between theoretical and experimental line energies listed in Table I are similar to those found at other Z values, see, for example, Graham and Merritt (1961). The central Auger line has three components, the K–$L_2L_2(^1S_0)$ and K–$L_1L_2(^3P_1)$ being indistinguishable because of the close energy spacing. The high-energy shoulder, however, is caused by the K–$L_1L_3(^3P_2)$ satellite line which has been seen at other Z values. The reader is referred to the paper by Graham and Merritt (1961) in this issue for a discussion of systematic trends in relative intensities with Z.

Note that the K–L_1L_2 and K–L_3L_3 lines are not consistent with the standard line shape and have excess counts at the locations predicted for their respective satellites. The K–L_1L_1 line, on the other hand, is consistent within errors. We believe the L_1L_2 and L_3L_3 discrepancies are too large to be attributable to experimental error and that they are real. The $Z = 54$ Auger lines due to the

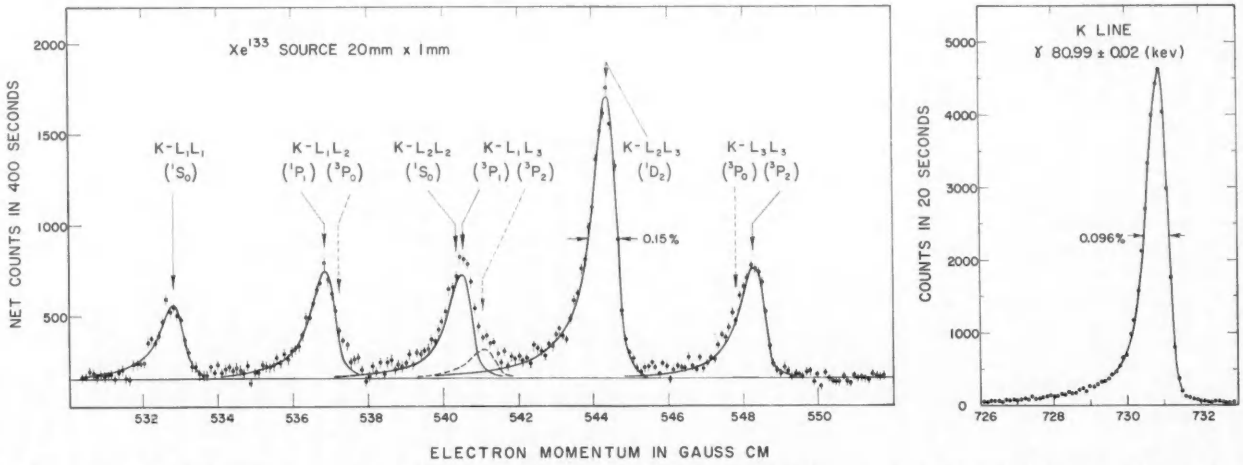

FIG. 1. The *K–LL* Auger spectrum of $_{55}Cs^{133}$ following β-decay from $_{54}Xe^{133}$. The *K* 80.99 conversion line in $_{55}Cs^{133}$ shown at the right gives rise to essentially all the *K* X rays and Auger lines from this nuclide.

K 233.2 line in the Xe^{133} 2.3-day isomer were $\lesssim 1\%$ of the $Z = 55$ Auger lines at the time of our experiments and hence were too weak to account for these excess counts. Thus there is qualitative evidence for the additional two satellite lines expected theoretically. The use of a stronger source, prepared with a de-accelerating system to slow down the Xe ions and reduce their penetration, should make it possible to investigate these effects quantitatively.

The absolute coefficient for K–LL Auger yield can be deduced from the data of Fig. 1 since the K-shell vacancies arise almost entirely ($>99\%$) from the K 80.99 conversion line shown at the right. This gives the ratio $\Sigma(K\text{–}LL)/K\ 80.99 = (6.58\pm0.10)\%$. From an additional measurement of the K–LM and K–LN Auger lines we deduce that $\Sigma(K\text{–}LY)/\Sigma(K\text{–}LL) = 0.48 \pm 0.03$. Using a value of $\Sigma(K\text{–}XY)/\Sigma(K\text{–}LL) \simeq 0.07$ (Wapstra *et al.* 1959), one obtains a value for the total Auger yield of $(10.2\pm0.2)\%$. The resulting fluorescent yield of $\omega_K = 0.898$ is to be compared with the value of $\omega_K = 0.877$ predicted by the semiempirical formula of Hagedoorn and Wapstra (Wapstra *et al.* 1959) for $Z = 55$.

ASAAD, W. N. and BURHOP, E. H. S. 1958. Proc. Phys. Soc. **71**, 360.
BERGSTRÖM, I. 1952. Arkiv Fysik, **5**, 191.
BROWN, F., GRAHAM, R. L., EWAN, G. T., and UHLER, J. 1961. Can. J. Phys. **39**, 779.
DAVIES, J. 1961. Private communication to F. Brown.
GRAHAM, R. L., EWAN, G. T., and GEIGER, J. S. 1960. Nuclear Instr. and Methods, **9**, 245.
GRAHAM, R. L. and MERRITT, J. S. 1961. Can. J. Phys. **39**. This issue.
WAPSTRA, A. H., NIJGH, G. J., and VAN LIESHOUT, R. 1959. Nuclear spectroscopy tables (North-Holland Pub. Co.), p. 81.

RECEIVED APRIL 13, 1961.
GENERAL PHYSICS AND RESEARCH CHEMISTRY BRANCHES,
ATOMIC ENERGY OF CANADA LIMITED,
CHALK RIVER, ONTARIO.

LETTERS TO THE EDITOR

Under this heading brief reports of important discoveries in physics may be published. These reports should not exceed 600 words and, for any issue, should be submitted not later than six weeks previous to the first day of the month of issue. No proof will be sent to the authors.

The Lifetime of the 6.25-kev Level in Ta^{181}*

Recently Muir and Boehm (1961) have shown the existence of a 6.25-kev level in Ta^{181}, and have determined from the M-subshell conversion ratios that it decays by $E1$ gamma-quantum emission about 2% of the time.

The Weisskopf estimate for the mean life of a 6.25-kev electric dipole transition in Ta is 10^{-9} sec. Making a correction for the known conversion coefficient (44 ± 7) and applying an inhibition factor of 10^8 which is typical for low-energy $E1$ transitions in heavy elements (Wilkinson 1960), we obtain 2.5 μsec as an estimate for the mean life of the level.

We have observed the transition and have measured the level lifetime.

A source of W^{181} (140 days) was prepared by employing 10-Mev protons from the Chalk River Tandem accelerator to initiate the (p,n) reaction in a 0.0005-in. tantalum foil. The tungsten was then separated chemically[1] and deposited on a thin teflon backing.

The low-energy gamma-ray spectrum was observed in a krypton- and CO_2-filled proportional counter having a thin Be window. This spectrum (Fig. 1A) shows the L X rays of tantalum and the 6.25-kev gamma ray. Figure 1A also shows a spectrum taken in delayed coincidence with the Ta K X rays (57.8 kev), the latter being detected in a NaI crystal, 1.5 in. diameter, 2 mm thick. The gate on the proportional-counter spectrum was opened 3.5 μsec after the detection of a K X-ray pulse and held open for 10 μsec. This coincidence spectrum shows clearly the 6.25-kev transition, as well as random coincidences with the L X rays. The area under the 6.25-kev coincidence peak has been measured for gate openings delayed by 3.5, 10, 15, and 140 μsec, the latter serving to provide a measurement of the random spectrum. The net counting rate in the remaining three delayed-coincidence spectra shows an exponential decrease with time corresponding to a half-life of $6.1\pm0.7\times10^{-6}$ sec. This result is shown in Fig. 1B.

Another measurement of the half-life has been made employing a time sorter originally set up to measure the lifetime of the 14.4-kev level in Fe^{57} (Clark 1961). The same detectors were employed, start pulses for the timing being derived from K X-ray pulses from the 2-mm NaI crystal, and stop pulses from the 6.25-kev peak in the proportional-counter spectrum. The result is shown in Fig. 1C, and gives a value $T_{1/2} = 7.0\pm0.4\times10^{-6}$ sec.

Our average value is thus $T_{1/2} = 6.8\pm0.4\times10^{-6}$ sec, which implies a mean life $9.8\pm0.5\times10^{-6}$ sec, in reasonable agreement with the estimate made for an $E1$ transition.

The value obtained for the lifetime implies an experimental width of 1.6×10^{-4} cm/sec in a Mössbauer-effect experiment. The gamma-ray energy, combined with the Debye temperature of tantalum ($\sim230°$ K) implies that the fraction of recoilless transitions at room temperature will be as high as 90%. Two of the main problems in the investigation of the recoilless radiation from the Ta^{181} 6.25-kev level will be those of extraneous vibration and temperature variations.

The assistance of Mr. G. C. Dixon is gratefully acknowledged.

CLARK, M. A. 1961. To be published.
MUIR, A. H. and BOEHM, F. 1961. Phys. Rev. To be published.
WILKINSON, D. H. 1960. Nuclear spectroscopy, B, 873, *edited by* Fay Ajzenberg-Selove (Academic Press).

RECEIVED MAY 10, 1961.
M. A. CLARK
NEUTRON PHYSICS,
ATOMIC ENERGY OF CANADA LIMITED,
CHALK RIVER, ONTARIO.

*Issued as A.E.C.L. No. 1268.
[1]I am indebted to Mrs. Janet Merritt for carrying out the chemical separation.

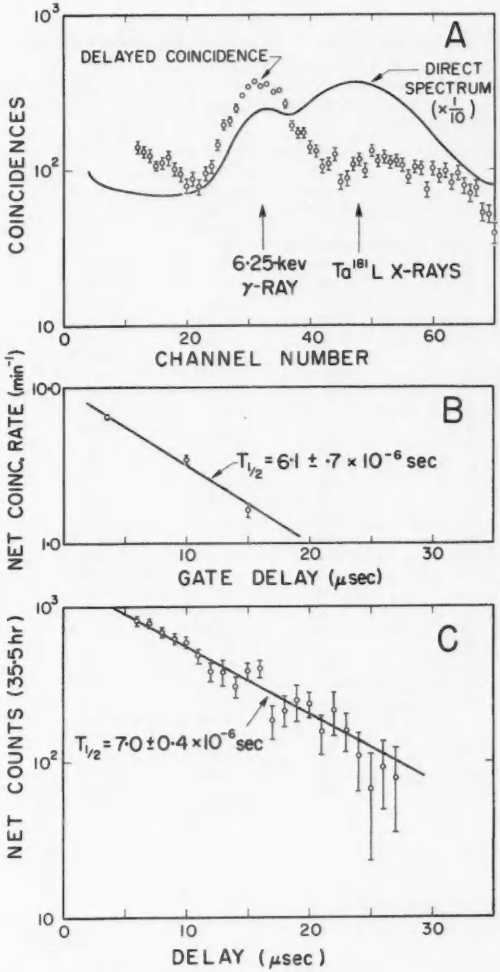

FIG. 1. A. Direct spectrum of low-energy gamma rays in the decay of W^{181}. The spectrum in delayed coincidence with Ta K X rays is also shown.
B. Delayed-coincidence intensity of the 6.25-kev gamma ray in Ta^{181} (10 μsec gate).
C. Delayed-coincidence intensity of the 6.25-kev gamma ray using the time sorter (1 μsec per channel).

Frequency Measurement of Standard Frequency Transmissions[1,2]

Measurements are made at Ottawa, Canada, using N.R.C. caesium-beam frequency resonator as reference standard (with an assumed frequency of 9 192 631 770 c.p.s.). Frequency deviations from nominal are quoted in parts per 10^{10}. A negative sign indicates that the frequency is below nominal.

Date, April 1961	MSF, 60 kc/s	GBR, 16 kc/s		WWVB, 60 kc/s
		6½-hour average*	24-hour average†	
1	−140	−150	−146	−147
2	−152	−152	−148	−147
3	−157	−152	−148	−144
4	−156	−155	−149	N.M.
5	−159	−157	−156	N.M.
6	−152	−153	−149	−148
7	N.M.	−147	−149	−152
8	N.M.	−139	−141	N.M.
9	N.M.	−147	−138	N.M.
10	−154	−152	−143	−149
11	−161	−146	−147	−152
12	−154	N.M.	−145	−153
13	−160	−149	−149	−150
14	−159	−152	−152	−150
15	−148	−144	−147	−146
16	−152	−143	−142	−147
17	−156	−147	−142	−151
18	−152	−146	−143	−154
19	−150	−151	−142	−153
20	−156	−149	−140	−150
21	N.M.	−156	−151	−152
22	−156	−157	−152	−147
23	−155	−154	−156	−148
24	−153	−147	−149	−154
25	N.M.	−138	−143	N.M.
26	−153	−150	−148	−153
27	−153	−149	−145	−155
28	−157	−152	−147	−155
29	−138	−143	−144	N.M.
30	−136	−141	−142	N.M.
Average	−153	−149	−146	−150
Midmonthly mean of WWV	−147			

NOTE: N.M. no measurement.
*Time of observations: 11:30 to 18:00 hours U.T.
†Time of observations: 15 to 15 hours U.T.

RECEIVED MAY 12, 1961.
S. N. KALRA
DIVISION OF APPLIED PHYSICS,
NATIONAL RESEARCH COUNCIL
OTTAWA, CANADA.

[1]Issued as N.R.C. No. 6371.
[2]Cf. Kalra, S. N. 1959. Can. J. Phys. **37**, 1328.

NOTES TO CONTRIBUTORS

Canadian Journal of Physics

MANUSCRIPTS

General.—Manuscripts, in English or French, should be typewritten, double spaced, on paper 8½×11 in. **The original and one copy are to be submitted.** Tables and captions for the figures should be placed at the end of the manuscript. Every sheet of the manuscript should be numbered. Style, arrangement, spelling, and abbreviations should conform to the usage of recent numbers of this journal. Greek letters or unusual signs should be written plainly or explained by marginal notes. Characters to be set in boldface type should be indicated by a wavy line below each character. Superscripts and subscripts must be legible and carefully placed. Manuscripts and illustrations should be carefully checked before they are submitted. Authors will be charged for unnecessary deviations from the usual format and for changes made in the proof that are considered excessive or unnecessary.

Abstract.—An abstract of not more than about 200 words, indicating the scope of the work and the principal findings, is required, except in Notes.

References.—References should be listed **alphabetically by authors' names**, unnumbered, and typed after the text. The form of the citations should be that used in current issues of this journal; in references to papers in periodicals, titles should not be given and only initial page numbers are required. The names of periodicals should be abbreviated in the form given in the most recent *List of Periodicals Abstracted by Chemical Abstracts*. All citations should be checked with the original articles and each one referred to in the text by the authors' names and the year.

Tables.—Tables should be numbered in roman numerals and each table referred to in the text. Titles should always be given but should be brief; column headings should be brief and descriptive matter in the tables confined to a minimum. Vertical rules should not be used. Numerous small tables should be avoided.

ILLUSTRATIONS

General.—All figures (including each figure of the plates) should be numbered consecutively from 1 up, in arabic numerals, and each figure referred to in the text. The author's name, title of the paper, and figure number should be written in the lower left corner of the sheets on which the illustrations appear. Captions should not be written on the illustrations.

Line drawings.—Drawings should be carefully made with India ink on white drawing paper, blue tracing linen, or co-ordinate paper ruled in blue only; any co-ordinate lines that are to appear in the reproduction should be ruled in black ink. Paper ruled in green, yellow, or red should not be used. All lines must be of sufficient thickness to reproduce well. Decimal points, periods, and stippled dots must be solid black circles large enough to be reduced if necessary. Letters and numerals should be neatly made, preferably with a stencil (**do NOT use typewriting**) and be of such size that the smallest lettering will be not less than 1 mm high when the figure is reduced to a suitable size. Many drawings are made too large; originals should not be more than 2 or 3 times the size of the desired reproduction. Whenever possible two or more drawings should be grouped to reduce the number of cuts required. In such groups of drawings, or in large drawings, full use of the space available should be made; the ratio of height to width should conform to that of a journal page (4¾×7½ in.), but allowance must be made for the captions. **The original drawings and one set of clear copies (e.g. small photographs) are to be submitted.**

Photographs.—Prints should be made on glossy paper, with strong contrasts. They should be trimmed so that essential features only are shown and mounted carefully, with rubber cement, on white cardboard, with no space between those arranged in groups. In mounting, full use of the space available should be made. **Photographs are to be submitted in duplicate**; if they are to be reproduced in groups one set should be mounted, the duplicate set unmounted.

REPRINTS

A total of 100 reprints of each paper, without covers, are supplied free. Additional reprints, with or without covers, may be purchased at the time of publication.

Charges for reprints are based on the number of printed pages, which may be calculated approximately by multiplying by 0.6 the number of manuscript pages (double-spaced typewritten sheets, 8½×11 in.) and including the space occupied by illustrations. Prices and instructions for ordering reprints are sent out with the galley proof.

Contents

R. L. Clarke—The spectrum of neutrons from the irradiation of uranium by 14-Mev neutrons - - - - - - - - - - - - - - - - - - 957

G. C. Hanna and R. L. Clarke—Neutron evaporation in the 14-Mev neutron fission of uranium - - - - - - - - - - - - - - - - - - 967

W. R. Bullock and D. M. Hunten—Vertical distribution of sodium in the upper atmosphere - - - - - - - - - - - - - - - - - - - 976

L. T. Shepherd and H. M. Skarsgard—Radio-frequency breakdown controlled by drift of electrons in an inhomogeneous magnetic field - - - - 983

V. H. Weston—The pressure pulse produced by a large explosion in the atmosphere - - - - - - - - - - - - - - - - - - - 993

K. G. McNeill, O. A. D. Trojan, and D. J. Dawson—Gamma-active fall-out in Ontario 1958–60 - - - - - - - - - - - - - - - - - - 1010

James R. Wait—The electromagnetic fields of a horizontal dipole in the presence of a conducting half-space - - - - - - - - - - - 1017

M. J. Laubitz—On measurement of thermal conductivity at high temperatures 1029

J. A. Bland and S. J. Basinski—The crystal structure of Bi_2Te_2Se - - - 1040

Tomiya Watanabe—Waves in a rarefied ionized gas propagated transverse to an external magnetic field - - - - - - - - - - - - - - - 1044

Robert L. Graham and Janet S. Merritt—The *K–LL* Auger spectrum of $_{66}Dy^{161}$ 1058

R. A. Hurd—A note on the diffraction of a scalar wave by a small circular aperture - 1065

Notes:

G. C. Benson and P. Balk—Estimation of the effect of surface on the dipolar broadening of magnetic resonance lines in crystals - - - - - - 1071

H. A. Buckmaster—Angular variation of axial spin-Hamiltonian eigenvalues in strong magnetic field - - - - - - - - - - - - - - - 1073

K. G. McNeill and J. D. Prentice—The 1.2-Mev beta decay of I^{128} - - 1080

A. D. B. Woods—Inelastic scattering of neutrons from rotating liquid helium II - 1082

W. B. Pearson and I. M. Templeton—The effect of dissolved iron on the thermoelectricity of silver at very low temperatures - - - - - - 1084

R. L. Graham, F. Brown, G. T. Ewan, and J. Uhler—The *K–LL* Auger spectrum of $_{55}Cs^{133}$ - - - - - - - - - - - - - - - - 1086

Letters to the Editor:

M. A. Clark—The lifetime of the 6.25-kev level in Ta^{181} - - - - - - 1090

Announcements:

S. N. Kalra—Frequency measurement of standard frequency transmissions 1092

Printed in Canada *by* University of Toronto Press